Thaw slump activity via close-range 'Structure from Motion' in time-lapse using ground-based autonomous cameras

Lindsay Faye Armstrong

A thesis submitted to the
Faculty of Graduate and Postdoctoral Studies
in partial fulfillment of the requirements
for the degree of
Master of Science in Geography

Acknowledgements

Firstly, a sincere thanks to my supervisor Denis Lacelle for providing me this opportunity, and the guidance and resources to support it. I've been free to choose my interests, make decisions, make mistakes, incessantly ask questions, and to approach this endeavor in an unconventional fashion. I've been afforded unquestioned support and the trust to execute plans under my own leadership. I've also been gifted with more exposure to Canada's remote north than I could have hoped for in life, and will forever be grateful for the perspective I've gained.

Thanks to my co-supervisor Rob Fraser responding to my constant enquiries, intelligent or otherwise, with thoughtful contribution, encouragement and enthusiasm. The collaborative spirit of our discussions reinforced my sense of capability and reminded me that science is intrinsically experimental and unpredictable.

Thanks to my committee members Luke Copland and Anders Knudby for also welcoming the exchange of ideas and for offering access to a wealth of resources.

Steve Kokelj is thanked for his collaboration, resources, time, thoughtful conversations, and for encouraging me to develop ideas from his work.

Thanks to my office mates of the Simard sub-basement; Jean Bjornson, Jean Holloway, Benoit Faucher, and Marjolaine Verret, for reminding me that I'm in the right place.

Thanks to my peer and field assistant Hugo Crites, who not only helped execute my campaign with enthusiasm and little guidance, but also contributed valuable ideas to the effort. I'm grateful to have had a willing sounding board over many kilometers driven and appreciate the moral support provided during the execution of the field work.

Thanks also to the Tetlit Gwich'in RRC of Fort MacPherson for their warm welcome, support and guidance. And specifically, to Billy Wilson, our guide on the Peel Plateau, for the hard work freely offered, the strategic advice, the "common sense" tricks for freeing 3ft drill bits from permafrost, and for genuine interest in my project. I feel fortunate to have been paired with not only an extremely capable guide, but also a highly enriching individual.

Thanks to Koreen Millard and Doug Stiff for many thoughtful discussions, troubleshooting help, patience, mentoring, and for their friendship over the years.

Thanks to my friends and family for their support over my academic career, and for providing me distraction from my work when needed. Thanks especially to my mother, who encouraged my excitable nature, ensuring I never considered questioning my ability or potential.

Thanks to Chris Stygall for his unconditional support and reassurance when I went back to school, for what ended up being more degrees than originally intended. His ability to understand what I

needed to get through far exceeds my own. Without that provision, I'm certain I would not have had as enjoyable a time on this trip as I have. I appreciate him ensuring that I reflect and realize that my anxieties often stem from positive ambitions, rather than unfortunate circumstances. This perspective reshaped my attitude towards challenge, in academics and in life.

Finally, thanks to Daniel Giradeau-Montaut for his revolutionary work and ongoing development in point cloud comparison, for his free software 'Cloud Compare' and for making himself available to the open sourced community for one on one troubleshooting.

Abstract

Northwestern Arctic Canada is one of the most rapidly warming regions in the Arctic (Serreze *et al*., 2009). Retrogressive thaw slumps (RTS) are one of the most dramatic thermokarst features in permafrost terrain (Kokelj *et al*., 2013). Many studies have focused on describing the distribution of thermokarst landscapes (i.e., Olefeldt et al., 2016), as well as change in thermokarst terrain over the historical record (i.e., Kokelj and Jorgenson, 2013). However, improved high temporal and spatial resolution monitoring of thaw slump activity is required to enhance our understanding of factors governing their growth. Recent advances in aerial and ground-based Structure from Motion (SfM), a photogrammetry application, allow for temporal and spatial high-resolution characterization of landscape changes. This thesis explores two methods in SfM photogrammetry: 1) aerial imaging using an unmanned aerial vehicle (UAV) and 2) ground-based imaging using stationary multi-camera time-lapse installations, to derive high-resolution temporal and spatial data for change detection. A trend in mean elevation change was produced, and agrees with the RTS behaviour over the study period, which supports the viability of the proposed capture method. The lack of congruency in data range suggests need for further development in terms of analyses and differencing algorithms employed. The proposed method may be feasible for employment in other fields of science in which high temporal resolution change detection is desired. This proof of concept study was conducted at a small slump on the Peel Plateau, NWT, Canada, and aims to enhance understanding of the development and perpetuation of thaw slumps, to better anticipate landscape and ecosystem responses to future climate change.

Résumé

Le nord-ouest de l`Arctique Canadien est l'une des régions qui subit le réchauffement le plus marqué de l'Arctique (Serreze et al., 2009). Les glissements de fonte rétrogressifs (RTS) sont l'une des conséquences thermokarstiques les plus dramatiques dans les régions périglaciaires (Kokelj et al., 2013). De nombreuses études ont décrit la répartition des paysages du thermokarst (Olefeldt et al., 2016), ainsi que ses changements pendant l`histoire (Kokelj et Jorgenson, 2013). Cependant, une meilleure haute résolution temporelle et spatiale de l'activité de décongélation est nécessaire pour améliorer notre compréhension des facteurs qui régissent leur croissance. Les avancées récentes dans la structure aérienne et terrestre 'Structure from Motion' (SfM), une application de photogrammétrie, permettent une caractérisation temporelle et spatiale à haute résolution des changements de ce type de paysage. Cette thèse explore deux méthodes de photogrammétrie SfM: 1) l'imagerie aérienne à l'aide d'un véhicule aérien téléguidé (UAV) et 2) l'imagerie au sol à partir d'installations de caméras stationnaires, afin de dériver des données temporelles et spatiales à haute résolution pour la détection des changements. Une tendance de variation de l'élévation moyenne a été produite et est conforme au comportement de la RTS au cours de la période d'étude, ce qui soutient la fiabilité de la méthode de capture proposée. Le manque de congruence dans la gamme de données suggère un développement supplémentaire en termes d'analyses et d'algorithmes de différenciation utilisés. La méthode proposée peut être réalisable dans d'autres domaines de science dans lesquels une détection de changement de haute résolution temporelle est souhaitée. Cette étude faisant une preuve de concept a été menée à un glissement petit sur le Plateau de Peel, NWT., au Canada, et vise à améliorer la compréhension du développement et de la perpétuation des glissements de fonte rétrogressifs, afin de mieux anticiper les retombées sur le paysage et les écosystèmes aux changements climatiques futurs.

Table of figures

List of tables

1 Introduction

Northwestern Arctic Canada is one of the most rapidly warming regions in the Arctic (Serreze *et al*., 2009). Warming air temperatures have caused an increase in permafrost temperatures (Burn and Kokelj, 2009; Romanovsky *et al*., 2010) and many studies have focused on describing the distribution of thermokarst landscapes (i.e., Olefeldt et al., 2016), as well as the change in thermokarst terrain over the historical record (i.e., Kokelj and Jorgenson, 2013). Retrogressive thaw slumps (RTS) are one of the most dramatic thermokarst features in permafrost terrain as they can thaw hectares of permafrost annually and modify the discharge of streams and rivers (Kokelj *et al*., 2013) and the geochemical composition and sediment loads of streams and lakes (Kokelj *et al*., 2009; Malone *et al*., 2013) which affect the aquatic ecosystems, namely benthic macroinvertebrates communities (Chin *et al*., 2016). Thaw slumps have a characteristic horseshoe shape with a near vertical headwall, a slump floor with low gradient and surface areas up to 52 ha (Burn and Lewkowicz, 1990; Lacelle *et al*., 2015). Thaw slumps can be initiated by many processes that expose ice-rich permafrost, including thermo-erosion along shorelines and coastlines, rain events, and forest fires that burn and remove the protecting organic cover (Burn and Lewkowicz, 1990). The growth of thaw slumps is driven by ablation of icy permafrost exposed in the headwall and has been largely correlated with summer air temperatures and solar radiation (Lewkowicz, 1987; Grom, J. D. 2008; Lantz and Kokelj, 2008). Slump stabilization occurs when ice-poor material is encountered (Wang, 2011), or when the exposed icy permafrost surface is buried by materials falling from the headwall overburden, thereby protecting the permafrost from further melt (Kokelj *et al*., 2015).

Improved high temporal and spatial resolution monitoring of thaw slump activity is required to enhance our understanding of factors governing their growth. Thus far, the study of factors that drive the growth of slumps has been limited to: 1) in situ micro-climate point measurements to derive energy conditions at the ablating icy headwall (Lewkowicz, 1987; Grom, J. D. 2008) repeat monitoring of headwall retreat to installed stake distance (Wang, 2011); or 3) coarse temporal and/or spatial scales studies associated with air photographs (Lantuit and Pollard, 2005; Lacelle et al., 2010; Swanson, 2012), from the derivation of tassel cap methods using Landsat images (Brooker *et al*., 2014), or pixel based calculations (Kokelj *et al*., 2015). Over the last few years, much work has been done to adapt non-metric cameras for spatial measurements into complex computer vision algorithms that allow many randomly ordered overlapping photos to derive high-resolution three-dimensional structure of a target (Snavely *et al*., 2006; Snavely *et al*., 2008; Furukawa *et* al., 2010). Recent advances in aerial and ground-based Structure from Motion (SfM), a photogrammetry application, allow for temporal and spatial high-resolution characterization of landscape changes. The stand-alone SfM software performs the photogrammetric processing of 2D images and generates 3D spatial data in the form of point clouds

and/or surface models. The reconstruction relies heavily on recognizable areas of a target (conjugate features) occurring in multiple photos such that the scale invariant feature transform of Lowe (1999) can image-match automatically, regardless of change in scale, resolution or view direction. In addition, one of the most important developments in SfM is the introduction of fodar, a method that effectively removes the need for ground control points (GCPs) in SfM studies (Nolan and DesLauriers, 2016). In geosciences, the possibility to derive digital elevation models (DEM) and orthophotos are the most relevant products of SfM as they allow for landscape change detection and deformation analysis.

Structure from motion has been employed to study fluvial erosion and hillslope processes in temperate environments (Pitkänen and Kajutti, 2004; Wangensteen *et al*., 2007; Sund *et* al., 2011; Krosley *et al*., 2006; Rivera et al., 2012). However, SfM has rarely been used to study active thermokarst landforms, and those who have conducted aerial surveys using a high-resolution SLR camera mounted to a helicopter (Swanson and Hill, 2010; Swanson, 2012). This thesis explores two methods in SfM photogrammetry: 1) aerial imaging using an unmanned aerial vehicle (UAV) and 2) ground-based imaging using stationary multi-camera photogrammetric time-lapse installations, to derive high-resolution temporal and spatial data of slump headwall ablation rates and volume of sediment transported along the slump floor. The proof of concept study was conducted at a small slump on the ice-rich Peel Plateau, NWT, Canada, where hundreds of active slumps are found. The thesis will contribute to enhance our understanding of the processes and climate linkages contributing to initiation, development and perpetuation of thaw slumps in an effort to better anticipate landscape and ecosystem responses to future climate change.

2 Literature review

2.1 Retrogressive thaw slumps

Retrogressive thaw slumps are some of the most dynamic thermokarst features in permafrost terrain (Figure 1). Thaw slumps typically have a steep headwall and a low-gradient foot slope and slump floor (Burn and Lewkowicz, 1990). They may be initiated following different mass wasting events, such as active layer detachments or gully erosion, which expose ice rich permafrost to insolation and precipitation (Lewkowicz, 1987; Lacelle *et al*., 2010). The rate of headwall retreat varies from a few to tens of meters per year, and is influenced by several factors including slump size, orientation, headwall height, net radiation and ground ice content (Lewkowicz, 1987; Grom, J. D. 2008; Wang, 2011; Lacelle *et al*., 2015). Differences in headwall height within an individual slump can cause retreat rates to differ spatially, as slumps with lower headwall heights have their exposed ice ablation surface more easily covered with falling overburden than slumps with a higher headwall (i.e., Wang, 2011). Slumps have also shown diurnal variation in headwall retreat that is associated with changes in insolation (Lewkowicz, 1987).

Under overcast sky condition, slumps with varying aspects showed similar retreat rates (Burn and Lewkowicz, 1990); conversely under clear sky condition, the retreat rates of slumps were closely related to their aspect, indicating the importance of insolation in thawing exposed ice-rich permafrost. However, over a thawing season, insolation rates and headwall aspect were uncorrelated to ablation rates (Lewkowicz, 1987; Wang, 2011), suggesting that the conditions of the icy permafrost have an influence on retreat rates and spatial behaviour (i.e. slumps retreat rates tend to be correlated with ice content in the headwall; Wang, 2011). This can be observed in slumps showing tongues of stabilized or un-slumped low ice content materials. At times these tongues can even be cut off completely from the headwall, leaving sediments islands on the slump floor (Lewkowicz, 1987). It has been shown recently by Kokelj *et al*. (2015) that increases in local rainfall can contribute to maintaining thaw slumps active by facilitating the transport of slump debris away from the slump floor following heavy rainfall events.

Thaw slumps can remain active for several years, and even reinitiate at the same location following a period of inactivity (Mackay, 1966; Kokelj *et al*., 2009). The development of thaw slumps tends to reconfigure slope morphology and drainage patterns (Kokelj *et al*., 2015), which can impact water quality of streams and lakes (Lantz and Kokelj, 2008; Lantz *et al*., 2009; Kokelj *et al*., 2009; Kokelj and Jorgenson, 2013; Malone *et al*., 2013). Slumps release solutes and carbon previously trapped in the frozen ground, increasing solute concentrations and sediment load in adjacent lakes and streams (Kokelj and Jorgenson, 2013). In addition, there is evidence that thaw slumps influence vegetation distribution and assemblage. The microenvironment in thaw slumps is warmer and more nutrient rich than undisturbed tundra, leading to altered plant community composition, including increased green alder growth and reproduction (Lantz *et al*., 2009).

2.2 Remote sensing

Our changing climate has led to an increased need in monitoring surface processes and how they are affected by climate. Thermokarst studies have intensified in recent years and provides context for exploring the environmental implications of permafrost degradation (Kokelj and Jorgenson, 2013). Many landscape-scale studies, using satellite or airborne datasets, have focused on describing the abundance and distribution of thermokarst landscapes (i.e., Olefeldt et al., 2016), allowing an assessment of how these landscapes may change in the future.

Lindenbergh and Pietrzyk (2015), made a distinction between change detection and deformation analysis. Change detection evaluates if there has been a change over time, often across pixels in a stack of imagery. Deformation analysis quantifies changes in a particular place over time. To date, there have been few studies focused on process-oriented field data collection that can contribute to change detection and

deformation analysis of thermokarst landforms and landscapes (Kokelj and Jorgenson, 2013). As such, a gap in monitoring exists regarding thermokarst landscapes and processes at time-scales shorter than what can be provided by available remote sensing datasets (i.e., multi-decadal scale for air photographs, ca. 2 weeks recurrence interval for Landsat imageries). The emergence and development of unmanned aerial vehicles (UAVs) and close-range remote sensing now allows study of individual features at high temporal and spatial resolutions. Unlike ground-based field studies involving logistically difficult fieldwork to acquire low density data sets, automated photogrammetric software has provided the ability to generate high-resolution datasets at low cost, creating a renewed interest in geomorphometry (James *et al*., 2006). Below we summarize some of the various remote sensing methods used to study thermokarst features, or analogous landforms.

2.2.1 Passive remote sensing for thermokarst landforms and landscape deformation analysis

From the advent of measurements from photographs, to the launch of the newest optical satellites, the development of change detection by passive remote sensing has allowed expansion of a wide range of scientific questions, and development of whole new fields of science. With improvements to spatial and temporal resolution of space-borne sensors over time, the length of the existing airphoto record and competitive cost of consumer grade cameras, change detection studies via passive remote sensing remains an important contributor to monitoring landscapes. These characteristics provide a baseline and the accessibility imperative to explore how the landscape responds to climate change now and into the future.

2.2.1.1 Passive space-borne remote sensing: optical imagery

Many studies of thaw slumps have been conducted at large spatial scales using satellite imagery, over long, low frequency time-frames (Lantuit & Pollard, 2008; Brooker *et al*., 2014; Lacelle *et al*., 2015; Séjourné *et al.,* 2015). However, many other thermokarst features of interest are too small or evolving too fast to capture with the most commonly employed satellite imagery (Landsat 8 (15m pan), SPOT (10m pan); Westoby, 2012). Although temporal and spatial coverage of high-resolution imagery (WorldView 3 (0.31m pan), GeoEye (0.41m pan), IKONOS (1m pan), RapidEye (5m pan)), revisit time of approximately 1-3 days) is adequate and available for thaw slump studies, they remain very costly and do not cover a long-time period, making time-series analysis impractical. Existing attempts to investigate temporal phenomena therefor often involve combination of multiple data sources to manufacture a more robust temporal dataset. Balser *et al.,* (2014) combined optical satellite imagery with synthetic aperture radar, field studies, airphoto surveys, and weather station data to investigate the relationship between thaw slump initiations in the Noatak Basin of northwest Alaska. They identified 21 RTSs in the region,

and concluded that early thaw season warming, snowmelt, precipitation and subsequent lengthening of the thaw season heavily influenced RTSs activity in the region. Similarly, Sejourne *et al*., (2015) used a combination of high-resolution optical imagery (50cm pixels) and field studies to investigate several thermokarst features in the central Yakutia region of Russia. The optical imagery was used to identify the distribution of the features, and the field studies to study environmental controls on permafrost thaw. They estimated headwall retreat rates, contributing a first step in assessing the development of thermocirques in that region. A similar study was conducted in the western Canadian Arctic by Segal *et al*. (2016), where optical satellite imagery and airphotos were used in combination to investigate the influence of climate and landscape factors on thaw slump dynamics, including slump size, density, and growth rates. They observed increased slump activity in conjunction with increased air temperature and precipitation, suggesting that slump activity will continue to intensify under a warmer and wetter climate.

Although an important tool, satellite imagery is often inadequate in spatial and temporal resolution to investigate feature behaviour without combination with other remote sensing methods. They are also often not able to evade issues specific to RTS, such as steep headwalls, causing them to be obscured by shadow or distorted by image foreshortening (Kääb, 2008; Westoby *et al*., 2012). Additionally, available imagery may not be employable due to cloud cover or lack of illumination during night-time acquisition. These both are considerable factors influencing study regions in the arctic. This issue has been somewhat evaded in some cases with the use of actively sensed InSAR interferometry (Short *et al*., 2011), however the issue of revisit time on annual scales remains.

2.2.1.2 Passive air-borne remote sensing: airphotos

The use of aerial photography for mapping and photogrammetry has been in practice for several decades and has provided the longest temporal resolution available to climate change detection studies (circa. 1950s). However, although this temporal resolution is extensive, it is coarse in photo acquisition frequency. Airphoto records usually only allow revisit frequencies in the decadal range, which limits the processes able to be investigated. Lacelle *et al* (2010), used multi-decadal airphoto records to identify initiation and stabilization of RTS on the Aklavik Plateau, NWT, Canada. The temporal frequency of the photos was not sufficient to isolate the timing of slump initiation; however, it was appropriate for investigation of the timing of slump stabilization (30-50 years) and reactivation of polycyclic slumps. Unlike other studies investigating the temporal behaviour and processes of RTSs, satellite imagery was not employed as the spatial resolution was too coarse to identify smaller thaw slumps. The study found a relationship between average air temperature and precipitation with slump initiation and longevity. Lantuit & Pollard (2005, 2008) also used multi-decadal airphotos to investigate the evolution of thaw

slump activity over a 50-year period along the coast of Herschel Island in Yukon Territory, Canada. They also photogrammetrically estimated coastal retreat rates based on slump headwall migration, as both processes are thought to be closely related. They did however suggest that limitations exist in this method, as the use of un-orthorectified imagery and the frequency of airphoto acquisition is inconsistent over time, both leading to uncertainty in results.

Although the use of air-photos had some advantages for large to medium temporal scale studies, they are not appropriate for frequent observations of thermokarst processes and landscape changes.

2.2.1.3 Passive terrestrial remote sensing; close-range photography

Close-range photography uses digital cameras to photograph landforms. Unlike other change detection methods with medium to coarse temporal acquisition times (satellites, airphotos), the high-temporal and spatial resolution introduced by UAVs and ground-based close-range photography allow investigation of smaller scale features and processes in accessible areas (Feng *et al.*, 2012). Depending on the remoteness of a study site, the temporal resolution of close-range photography change detection studies may vary from annual to daily depending on site conditions. Chandler *et al*., 2002 performed daily capture of a riverbed stretch in Alberta, Canada, however only over a thirteen-day period. This permitted high spatial and temporal resolution DEM differencing, but could not perform longer term studies as the cameras were not truly automated, requiring a person to shoot pictures from cameras each day. Also, this method provided only stereo pairs from fixed vantage points and required manual survey of 2000 control points each day, which required 8-10 people work for 5-6 hours, and then input data for another 1-2 hours each day. This methodology could not be employed at study sites where access is limited and expensive, as is the case in Arctic regions.

James and Robson (2014) executed an SfM study at a high temporal resolution (one epoch each minute for 37 minutes), producing DEMs of moving lava, however, again only in stereo pairs. Although only two cameras were used, it was noted that an advantage of the approach is the ability to expand the network of cameras to extend spatial coverage. They also noted however, that challenges remain in the practical application of such methods due to uncontrolled and dynamic environments, such as near active lava flows. These problems could be evaded in less dangerous study sites by leaving installations for longer periods of time, allowing optimal data sets to be chosen from a larger volume of continuous data.

A major advantage of ground-based change detection studies is the substantially lowered cost relative to any air- or space-borne acquisitions, especially if shorter revisit time is required. Despite the advantages, there are practical problems such as sites with inadequate or inappropriate viewpoints to attain proper capture geometry, as well as the remaining need for traditional surveying for data anchoring

or validation (Chandler *et al*., 2002). This need however, may become removed in future studies as "fodar", SfM without ground control, becomes more generally accepted (Nolan and DesLauriers, 2016). Changes over time can be monitored, but the factors influencing change may remain difficult to quantify. Additionally, these analyses are less able to study the relationship between the small-scale processes it records and landscape level factors, which may influence them. Therefore, landscape-scale and feature-scale studies must work increasingly in tandem to address both aspects, as both have inherent spatial and temporal limitations.

2.2.2 Active remote sensing for thermokarst landforms and landscape deformation analysis

Unlike passive optical technologies, active remote sensing is based in ranging. These ranging technologies are similar conceptually to SONAR, in that they send a pulse of energy to a target, and record the time it takes for the pulse to return to the sensor. Knowing the speed of the laser, this time is then transformed into a distance. The high frequency of pulse return creates a high point density, and therefore a finer resolution subsequent topographic dataset. In addition, ranging technologies can overcome certain limitations of optical methods, namely penetration depth. Whether from space, air, or the ground, ranging systems are able to move through obstacles such as such cloud or vegetation, which cause impediments to optical technologies. However, similar issues to those of air- or space-borne passive technologies, namely high cost and low temporal resolution, weaken these ameliorations. This low temporal resolution is also true of ground-based studies (terrestrial laser scanning) as the return rate is a function of the sensor's high cost. Nonetheless, advances in conceptual simplicity of ranging technologies have enabled researchers to examine geomorphological targets in finer detail, and with less complicated methodologies than in the past. Until Structure from Motion study results became abundant enough over the last decade to compare among themselves, state of the art laser scanning results were the standard by which these newer technologies were measured.

2.2.2.1 Active space-borne remote sensing; InSAR

Synthetic aperture radar interferometry (InSAR) is a well-established technique for measuring ground movement (Lu *et al.,* 2004; Wdowinski *et al.,* 2008; Van Wychen *et al.,* 2012); however short repeat periods, acquisition conflicts and difficulty maintaining coherence over vegetated northern environments has limited success in permafrost studies. This is exemplified by Short *et al*. (2011) who compared three interferometric synthetic aperture radar data sets for their ability to detect ground movement over the continuous permafrost site of Herschel Island, Yukon Territory, Canada. Even when coherence was high, phase patterns were not thought to be related to topography or geomorphology,

suggesting that much of the signal was atmospheric, or interference by vegetation, rather than ground movement. There have also been problems reporting the accuracy of such deformation analyses, as changes in soil moisture can complicate quantification of true surface displacement (Short *et al*., 2011). With favorable look directions, known areas of instability could be mapped. Only with several independent InSAR data sets could real trends be identified and confirmed, limiting the application's explorative abilities. Balser *et al.* (2014) used synthetic aperture RADAR to study the initiation of RTS in the Noatak Basin of northwest Alaska, as it relates to environmental factors (annual air temperature, precipitation, and snow cover) in combination with several other remote sensing methods (optical satellite imagery, helicopter supported airphoto surveys) and field campaigns. This need for combination of data sources, as well as lack of ability to validate results from InSAR, leaves active space borne deformation analyses inappropriate for large-scale permafrost studies, let alone those at a small scale. As more RADAR sensors come online and their data becomes more available, further development for deformation analyses can be made.

2.2.2.2 Active air-borne remote sensing; LiDAR

LiDAR (Light, detection and ranging) is often referred to as laser scanning. The target is flooded with pulses, iteratively building a three-dimensional surface model based on the return pulse timing. LiDAR has the advantage over photogrammetric methods in that it is not limited by certain terrain types or characteristics. Unlike optical sensors, ranging methods can readily discern vegetation surfaces and does not suffer confusion from lack of radiometric contrast common to homogeneous terrains, such as snow, ice, or water (Kääb, 2008). With adequate funding, LiDAR provides the spatial resolution that optical satellite imagery has yet to achieve over small to medium areas, allowing quantification of volume change over time in riverbeds (Thoma *et al*., 2005), on glaciers (Bamber *et al*., 2005), and many other landforms. Although airborne LiDAR's spatial resolution has great potential for monitoring thermokarst landforms, high costs have limited acquisition to small areas or strips (Kääb, 2008; Kokelj and Jorgenson, 2013), or studies of several features in an area, rather than any particular one (Janeras *et al*., 2004; Sauber *et al*., 2005; Jones *et al*., 2013; Levy *et al*., 2013). For example, Obu et al (2016) used two LiDAR surveys (1m horizontal resolution) one year apart, to study coastal erosion and mass-wasting processes along the coast of the Yukon Coastal Plain and on Herschel Island. They studied elevation changes, volume changes and coastline movement patterns, revealing occasional events which are otherwise obscured when averaged over lower temporal frequencies (as in airphoto or satellite imagery). Glenn *et* al. (2006) used LiDAR, in combination with historical movement data and field observations, to examine the surface morphology of a landslide in southern Idaho. They were able to characterize several small-

scale parameters and concluded that the analyses and results of the study would not have been possible with coarser scale digital elevation models (10-m DEM), and that LiDAR is directly applicable to analyzing other geomorphic surfaces at appropriate scales (i.e., RTS). These are some examples of how although highly successful for geomorphic study, time-series analysis with LiDAR is limited to the past couple decades as the technology and its data sets are also relatively new (James *et al*., 2006).

2.2.2.3 Active terrestrial close-range remote sensing; terrestrial laser scanning

Traditional ground surveys involved direct contact with a target of interest, often threatening damage to the target, or danger to the surveyor. Advances in ground-based active remote sensing techniques are appropriate for high frequency, small study areas and can expand the detail of a site identified with air- or space-borne remote sensing (Kääb, 2008). With the rise in popularity of laser scanning technologies, the limitations of access, resolution and collection speed are addressed. Many studies successfully captured data that allowed change detection (Hsiao *et al*., 2004; Lindenbergh and Pietrzyk, 2015), including for RTS. Barnhart *et al*. (2013) investigated changes in thaw slump headwall morphology on the Selawik River in Alaska using high frequency repeat terrestrial laser scans. They scanned the slump every 12 hours for the months of July and August, in two consecutive years. From their results, they produced statistical models, which investigated the influence of environmental drivers on headwall retreat rate. They found that rate was related to insolation and air temperature, however noted that more work was needed to better model the retreat data. Krieger *et al*. (2009) used robotic total stations and ground-based terrestrial laser scanners (TLS) to look for consistencies in the morphology of RTSs in three different environments in southern Alaska. They concluded that there is a characteristic form to RTS, and that there may be a scaling factor present.

Laser scanners can be used by a single person in the field, increasing data-acquisition rates enormously (Chandler *et al*., 2002). However, they are prohibitively expensive and not ideally suited to the rigours of Arctic fieldwork, therefore limiting their use for long-term studies. Nonetheless, TLS are less expensive than air-borne laser scanning as it is expensive to commission aircraft of any kind. This means that TLS are employed in many varied fields of science requiring dense topographic data, and are often used to validate the results of other technologies.

2.2.3 From photogrammetry to Structure from Motion

Photogrammetry is the measurement of objects through photographs and is based on the principles of traditional stereoscopy, which uses the difference in angle between two overlapping photos of a target to derive its geometry. Several studies (Barker *et al*., 1997; Jiang *et al*., 2008; Taboga, 2011;

Fonstad *et al*., 2013) describe the traditional methods of photogrammetry, which involve complicated manual measurements and calculations, as well as specialized camera calibrations and plotters. These complexities left the method isolated to highly trained individuals and inaccessible to non-specialists. Thus, the pursuit towards non-metric cameras for spatial measurement became important and, not long after, mathematical models arose to represent non-metric cameras and their distortions (Hottier 1976). Over the last few decades, much work has been done to adapt and expand these concepts into complex computer vision algorithms that allow many randomly ordered overlapping photos to derive high-resolution three-dimensional structure of a target (Snavely *et al*., 2006; Snavely *et al*., 2008; Furukawa *et* al., 2010). More recently, photogrammetric software programs, grouped under the term 'Structure from Motion' (SfM), have been developed which combine the fore mentioned algorithms into user-friendly interfaces (i.e., Agisoft Photoscan and Pix4D). The SfM software facilitate reconstruction of nearly any target a user may be interested in, without major calibration intervention, provided certain requirements are met (Micheletti *et al*., 2015).

The stand-alone software performs the photogrammetric processing of 2D images and generates 3D spatial data in the form of point clouds and/or surface models (Agisoft, 2013). The reconstruction relies heavily on recognizable areas of a target (conjugate features) occurring in multiple photos such that scale invariant feature transform (SIFT) of Lowe (1999) can image-match automatically, regardless of change in scale, resolution or view direction. In geosciences, rather than the 3D model itself, it is the possibility to derive DEM and orthophotos that are the most relevant products. Westoby *et al*. (2012) was one of the first to use SfM techniques to map the 3D structure of a steep alpine hill slope and demonstrated that the SfM-derived elevation measurements were within 0.1 m of a TLS scan. Fonstad *et al*. (2013) also showed accurate SfM results for geomorphological mapping in comparison with on-ground GPS (<0.1 m error in X, Y, and Z) and airborne LiDAR surveys. After the suitability of SfM for geosciences became apparent from these pioneering studies, the number of studies using the method has increased significantly, with 61 publications (34 terrestrial and 27 UAV) in a variety of fields (Eltner *et al*., 2015), including investigations of bank erosion in fluvial systems (Barker *et al*., 1997, Stojic *et al*., 1998; Lane *et al*., 2000; Hancock and Willgoose, 2001; Lawless and Robert, 2001; Chandler *et al*., 2003), and slope stability and landslide dynamics (Chandler and Brunsden, 1995; Mora *et* al., 2003; Walstra *et al*., 2004; Haneberg 2008; Niethammer *et* al., 2011; Feng *et al*., 2012; Lucieer *et* al., 2014; Stumpf *et* al., 2015), which are close analogs of RTS in terms of morphology and relative speed of change. For example, Stumpf *et al*., 2015 monitored mass movements of the Super Sauze landslide in France over time using SfM with images acquired from the ground, rather than from an aerial perspective. They compared their reconstructions to both LiDAR and TLS data in three separate post processing pipelines.

As the coverage attained in each epoch relative to the LiDAR scan differed, full change detection could not be reported for the whole study area; instead changes in smaller areas of acceptable coverage were reported. They were able to detect change between 5 and 7m, noting that the minimum change detected at 95% confidence was 0.2 m, since the co- registration error was 0.1 m.

Originally employed in geosciences for quick and cheap airphoto acquisition, UAVs are now also taking advantage of the rise of accessible optical imagery and photogrammetric software to produce 3D models and topographic derivatives such as DEMs. The resulting products from UAV acquisition are comparable, if not superior in many cases to products derived from airborne LiDAR or terrestrial laser scanners, with accuracies in the centimeter range (Fonstad *et al*., 2013). Fonstad *et al*. (2013) also conveyed an improvement in point density relative to LiDAR, which reduces interpolation in surface models. This shift in prevailing technology has led to the surge in realized applications for UAV photography. For example, Neithammer *et al*. (2012) also employed a UAV to study the Super Sauze landslide in France for change detection. They produced two epochs of data for differencing, and used a TLS for high detail mapping in certain areas as well as 199 GCPs for validation, which showed spatial variability in accuracy. They found accuracy reduced considerably towards the boundaries of the surveyed area, falling from a mean error of 0.5m to up to 3.9m in the periphery. Although acceptable when investigating multi-year change, errors of this magnitude would not be appropriate for studies of shorter time intervals. This suggests that UAVs may not be appropriate to study features of this large size, as other studies have much lower error on smaller target features. There are however, other downfalls to using UAVs for data acquisition. As with many other technologies, a learning curve exists not only in regards to piloting, but also in survey design, camera parameter selection, and pre and post processing. There also remains a limitation due to legal restrictions of UAV use, such as areas permitted for flight and necessity to maintain visual contact. Furthermore, there lies a limiting factor in terms of return rate for time-series studies, especially for studies in remote environments such as the Arctic. It is for this reason that many time-series studies of concern to climate change, although methodologically simple, have yet to be conducted.

One of the most important recent advances in SfM is the introduction of fodar (Nolan and DesLauriers, 2016), a method that effectively removes the need for ground control points (GCPs) in SfM studies. GCPs are one of the remaining major constraints of SfM use for remote studies, as their installation and record by dGPS, requires extensive fieldwork, a negation of the allure of SfM methods; less field time. The innovation was seeded from the desire to annually track volume change of 800+ glaciers in the road-less remote arctic (Nolan and DesLauriers, 2016). This was financially unfeasible using conventional LiDAR or InSAR, neither of which employs ground control. They repeated their

survey five times, not only to report precision, but also to detect snow cover change on mountaintops. Results were verified against LiDAR surveys, as well as ground dGPS surveys processed with the precise point positioning (PPP) method and reported accuracy and precision of better than +/-20cm at 95% RMSE for four acquisitions. They found that not only are their results accurate, but they also could not be improved by the inclusion of GCPs. Also, they use onboard survey grade GPS instead of camera EXIF data to constrain photo locations, increasing accuracy and reducing post processing time. They suggest no GCP network can match fodar results, as fodar can be considered survey grade SfM, whereas GCP dependent SfM remains consumer grade.

Structure from motion has been used sparingly in recent thermokarst studies, generally with high-resolution SLR camera surveys conducted from air via helicopter (Swanson and Hill, 2010; Swanson, 2012) or UAV (Fraser, unpublished), or from the ground (Kääb *et* al., 2014). Few studies have employed stationary autonomous cameras for modeling, and those who have (Pitkänen and Kajutti, 2004; Wangensteen *et al*., 2007; Sund *et* al., 2011; Krosley *et al*., 2006; Rivera et al., 2012) have kept to traditional stereo pair based photogrammetry, rather than SfM. The closest analogous target features to thermokarst thaw slumps are considered to be landslides or coastal erosion studies.

3 Study area and target sites

The study area is situated in the Stony Creek watershed of the Peel Plateau of northwestern Canada. The plateau lies in the southeastern foothills of the Richardson Mountains, and gently slopes down eastward from 650 m in the foothills of the Richardson Mountains to 100 m a.s.l. west of the Peel River.

The region experiences long cold winters and short cool summers. The mean annual air temperature at Fort McPherson (1986–2007) is −7.1 °C (Environment Canada, 2015). Mean July temperature is 15.3 °C, and the coldest month, January, has a mean temperature of −27.2 °C. A warming trend in the region is indicated by an increase in mean annual air temperature of 0.77 °C per decade since the 1970s (Burn and Kokelj, 2009). Average annual rainfall over the period 1986-2007 was 146.2mm (Environment Canada, 2015). However, there has been a significant increase in rainfall in recent years, including a large increase in the frequency and magnitude of extreme rain events starting in 2005 (Kokelj *et al*., 2015). The five largest rain events (>25mm) occurred in the last decade, and included a 40 mm and 64 mm event in 2010 and a 67mm event in 2012.

The fine-grained turbic cryosol (clayey silts with less than 10% gravels) supports vegetation that consists mainly of arctic tundra assemblages, sedges, and some dwarf shrubs on the uplands (*Betula* spp., *Alnus* spp., *Salix* spp., *Cyperaceae* spp., *Eriophorum angustifolium*) and of open black spruce woodlands,

willows and alders in the lowlands (*Picea* spp., *Populus balsamifera*). These climatic and environmental conditions ensure that the study area is situated in the continuous permafrost zone (Burn, 2015). A site 22km west of Fort McPherson was estimated to have permafrost approximately 120m thick (Mackay, 1967). The permafrost in the study area was warm, especially with proximity to the Dempster Highway due to increased snow coverage on road embankments, and its temperatures have increased by more than 2 °C in response to warming air temperatures over the past few decades (O'Neill *et al*., 2015a). The mean active layer thickness on the Peel Plateau is 68cm and has shown a trend of thickening over the past few years (O'Neill *et al*., 2015a; 2015b). The permafrost of the Peel Plateau is characteristically ice-rich and may have thick layers of massive ground ice (Fontaine, 2016). The ground ice content of permafrost in the Stony Creek watershed is estimated from measurements as 50 vol.%, to tabular bodies of ground ice (Lacelle *et al*., 2004, 2010; Malone *et al*., 2013; Fontaine, 2016).

The ice-rich landscape of the Peel Plateau is dotted by hundreds of active thaw slumps of various sizes that developed in tills and glacio-lacustrine sediments deposited between 18-15 ka cal BP (Lacelle et al., 2015). In a 15,700km^2 area of the Peel Plateau and Richardson Mountains, Lacelle *et al*. (2015) identified 189 active slumps greater or equal to 0.4ha, using tassel cap transformations of Landsat imagery. The average size was 5.4ha, and included 10 slumps over 20ha in size. These large slumps, now termed mega-slumps, accounted for 27% of the total slump surface area mapped. The slumps occurred most commonly on east facing slopes of 8-12 °. A random sample showed headwall retreat rates from 5 to 60m yr^{-1}, with an average rate of 12.4 ± 7.4 m yr^{-1} (Lacelle *et al*., 2015). The region has seen a pronounced increase in the size distribution and abundance of large, active thaw slumps from 1985-1990 to 2011 (Kokelj *et al*., 2015).

The selection of thaw slumps for photogrammetry was based on site accessibility (within 1km of the Dempster Highway), size and feasibility to fly the UAV and install trail cameras. There were a few slumps of interest in Stony Creek watershed that could be targeted for photography. Charas (FM2) and Melanie (FM3) are situated along Dempster Creek. Charas slump, at 54 ha and 0.656 km wide, is the largest on the Peel Plateau and too large to target for photogrammetry. In 2012, Melanie slump had a 10 m high headwall and the slump covered an area of 7 ha, including the debris tongue (Kokelj *et al*., 2015). As the summers of 2010 and 2012 were particularly wet, this slump grew significantly and is now too large to be properly instrumented and fully monitored by the proposed method (Figure 2, 3; Table 1). Two smaller slumps (D1 and CB) are accessible and may be appropriate for the study due to their smaller size, and proximity to the road. During the field season in June 2016, it was decided that D1 (Figure 2, 3) would be instrumented and become the main study site, as CB proved too large and showed evidence of frequent grizzly bear activity thought to present risk to the camera installations.

D1 is a small RTS on the south side of the Dempster highway, approximately 25km east of the NWT border in the foothills of the Richardson Mountains. The slump sits at approximately 580m elevation, has a northern aspect (faces north) and an approximate area of 0.5ha. The ground ice content of the D1 slump is estimated from other measurements in the Stoney Creek watershed, as 50 vol.%, to tabular bodies of ground ice (Lacelle *et al*., 2004, 2010; Malone *et al*., 2013; Fontaine, 2016). The slump floor has a small creek running through it at the topographic low near the toe of the slump.

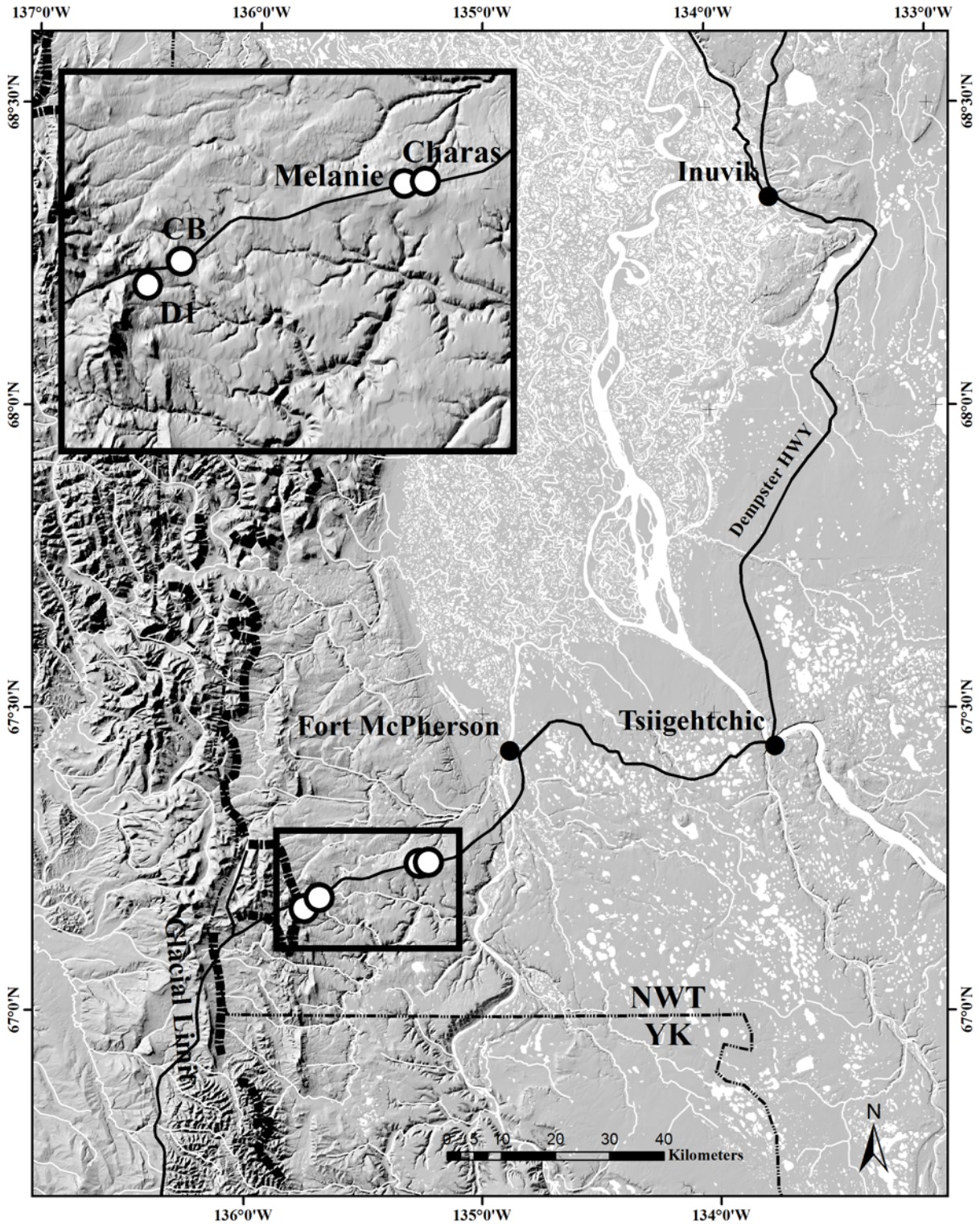

Figure 1. Location of D1, CB, Melanie and Charas slumps on the Peel Plateau, NWT, Canada.


Melanie slump


Charas slump

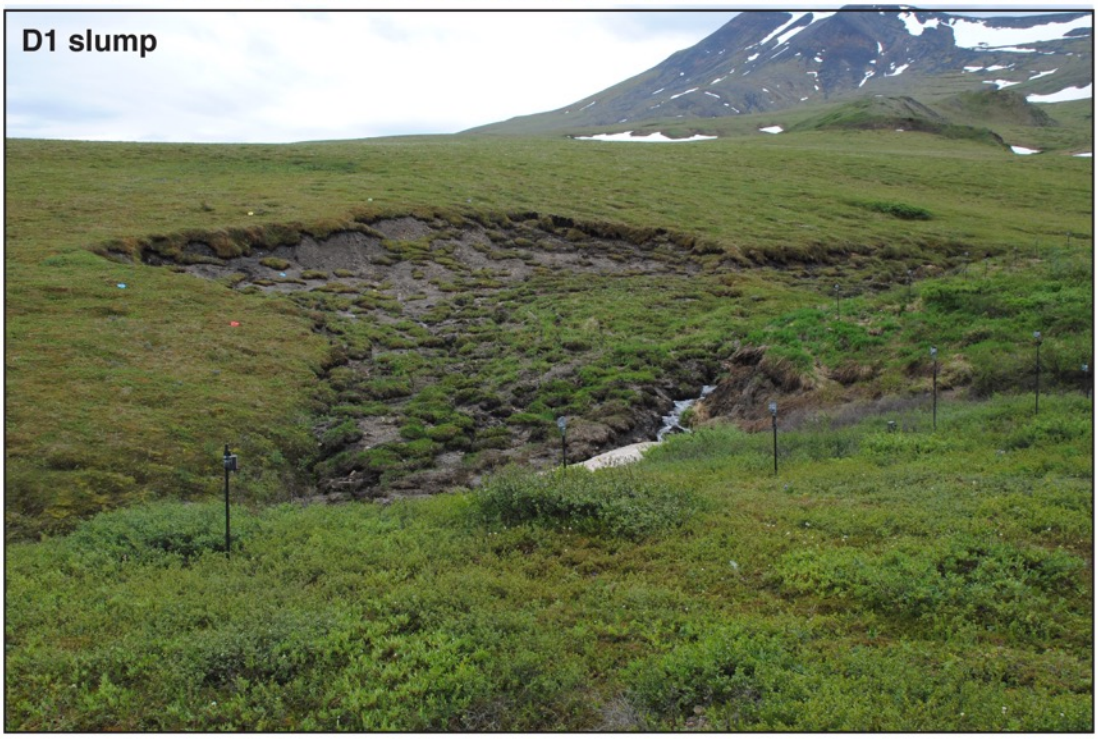
D1 slump

Figure 1. Morphology of retrogressive thaw slumps in the study area (Peel Plateau, NWT, Canada). A) Melanie (mega slump), B) Charas (mega slump) and C) D1.

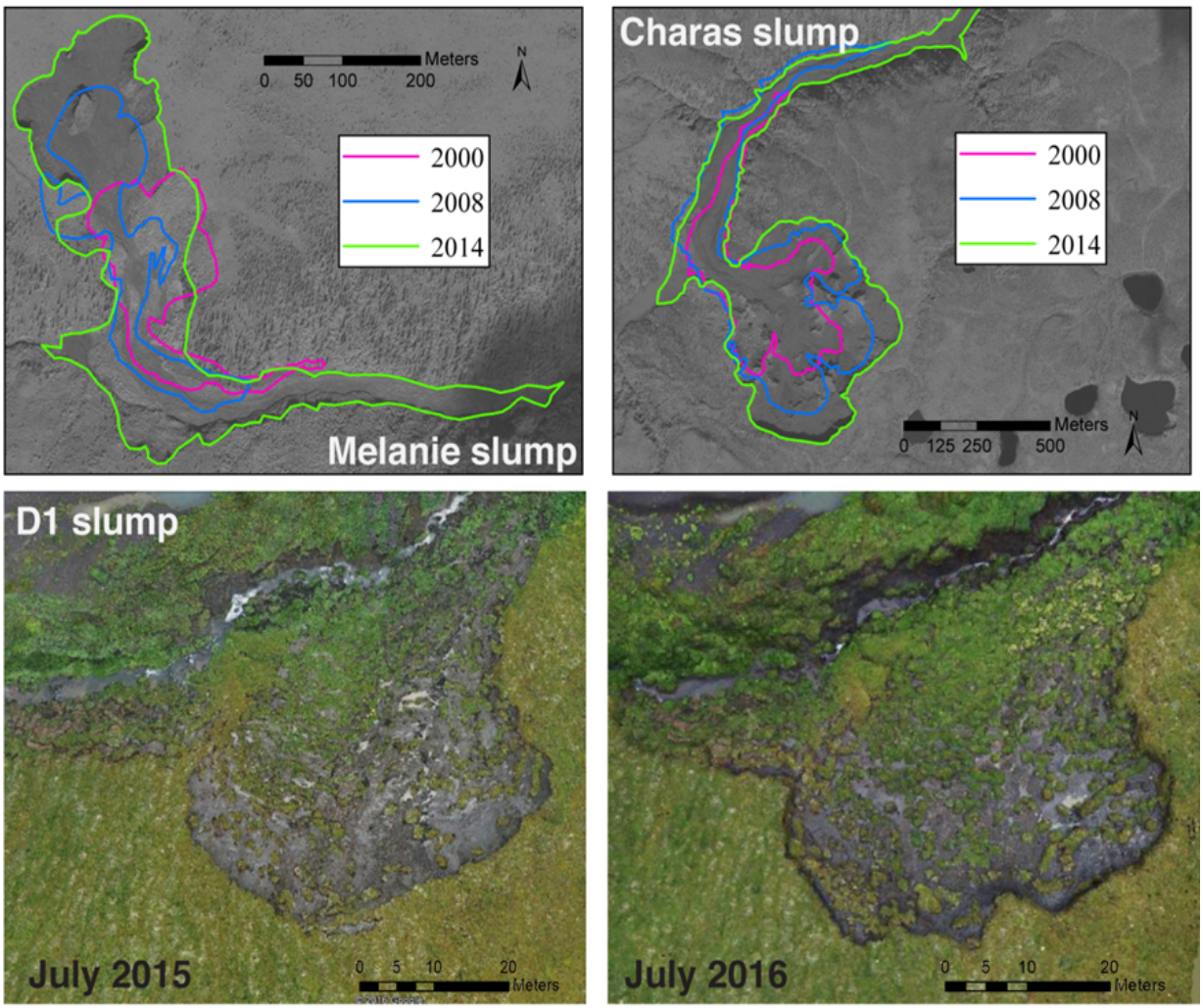

Figure 2. Change in area of FM3: Melanie (top left) and FM2: Charas (top right) over the years 2000, 2008, 2014 (Digital Globe). Changes in area of D1 (bottom) over one year period (July 2015 and July 2016)**.**

Table 1. Recent areal growth of Peel mega slumps.

Slump	2000 (m^2)	2008 (m^2)	2014 (m^2)	Elevation (m)
FM3 (Melanie)	27,215	29,999	89,092	398
FM2 (Charas)	164,345	300,466	447,572	353

*Calculations computed using Digital Globe imagery.

4 Methodologies

Photogrammetry is a method that allows detection of morphological change at different scales (Chandler, 1999). In this study, a UAV mounted with a digital camera and ground-based stationary trail cameras were used to collect photographs from an active thaw slump on the Peel Plateau, NWT. SfM photogrammetry assigns a point to a 3D location in local space, which represent a recognized pixel

repeated between images. The point is also assigned a RGB value, which matches that of the recognized pixel colour. This process is repeated until a cloud of points is formed, representing the target object. This 'point cloud' represents a pixelated 3D model of the object, which can be transformed into a 2D DEM. The latter is then used to investigate morphology and growth patterns of the slump (i.e., headwall retreat rates and changes in surface elevation). Air-borne imagery was acquired on July 27, 2015 and August 3, 2016; whereas ground-based imagery was acquired over the 2016 thaw season; June 27, 2016 to September 2, 2016. The veracity of the terrain deformation analysis derived from the ground-based SfM model, a new application in this type of study, was assessed by comparing with those from the air-borne SfM model.

4.1 Field procedures

4.1.1 Field tests in the Ottawa region

The position of stationary cameras is the most important aspect in the functioning of ground-based SfM and will influence the resolution and accuracy of subsequent models (Cerminaro, 2014). Barker *et al*. (1997) and Stumpf *et al*. (2015) highlighted the need for test runs prior to main execution as the camera orientation, parameters, and many other factors, vary among targets. Given the importance of installation geometry on successful reconstruction and the complexity of determining proper geometry, two field trials were conducted in the Ottawa region (Cantley Quarry, Quebec and Milles Isles, Quebec) where features occur (an aggregate stockpile and a blasted bedrock wall respectively) that have analogous horseshoe-shape of similar size to our intended D1 thaw slump target. These trials, although used 20 mega-pixel Canon EOS 6D digital SLR camera, aimed to investigate the effect of camera focal length, distance to target, camera spacing and elevation above ground, as well as GCPs abundance and distribution (Figure 4). The results of these trials indicated that baseline offset ratios of 1:6 to 1:8 were appropriate, the distance between the cameras (between overlapping photos) relative to the distance from the camera to the intended target, ratios similar to those used in other studies (e.g., Chandler *et al*., 2005; Krosley *et al*., 2006; Chandler *et al*., 2002; Haneberg 2008; Eiken and Sund, 2012). It was also found that positioning cameras at different height above the ground (vertical offset) and at variable distances to the target was advantageous in the reconstructions of SfM models. Finally, it was also apparent that the employment of cameras position for location anchoring, rather than GCPs position, still resulted in high-accuracy reports of the models, which agrees with assertions made in 'fodar' methodology.

Figure 4. Morphology of features targeted for local field trials in the Ottawa region. Aggregate stockpile at the Cantley quarry, Quebec (left) and cul-de-sac with blasted outcrop wall in Milles Isles, Quebec (right).

4.1.2 Acquisition of UAV imagery

In 2015, UAV photo surveys of the D1 slump were conducted on July 27 by Rob Fraser of CCRS using a 24 megapixel Sony a6000 mirror less camera with Sony f/2.8 20mm pancake lens mounted to the UAV. The UAV used was a Spyder PX8 3 Plus 1000 octocopter by XPedition Robotics. The PX8 uses the 3DR Pixhawk flight 4 controller running ArduCopter v3.2.1 and dual 6S 6,600 mAh LiPo batteries. Mission Planner v1.3 software was used to create an autonomous mission in a grid pattern with up to 83% forward overlap and 75% side photo overlap at 70 m height above the ground, resulting in 24 photos. The photos were captured in shutter priority mode at a 1/1000 s interval, 400 ISO, and with focus fixed at infinity. GPS tags were added to the JPEG EXIF information using the log file from the onboard 3DR UBlox GPS that provided a 5 Hz update rate. The 1-2 m accuracy UAV georeferencing were optimized using four GCP ground targets located to within 2 cm accuracy using post-differential GPS correction to a nearby base station that was running for 7 hours and corrected using the NRCan online PPP system. The GPS unit was a Trimble R9s.

In 2016, the D1 slump was surveyed on August 3 by Rob Fraser of CCRS using the DJI Inspire Pro. The Inspire Pro has a 6S 4,500 mAh LiPo battery, and the DJI GO automated flight software provided overlap, height, and resolution were similar to that of the 2015 survey. The photos were captured in automatic exposure mode at 200 ISO, which gave a shutter speed around 1/1000s. The locations of the stationary cameras (see section below) and four GCPs were surveyed in a similar manner as 2015 using two Leica GS14 Performance Smart Antenna GPS's. The GCPs surveyed did not fall within the successfully modelled areas by the ground based SfM and were not able to be employed for referencing in those models.

4.1.3 Acquisition of time-lapse imagery using stationary trail cameras

The D1 slump was photographed at hourly interval in summer 2016 (June to September) using twelve 12MP Solar SpyPoint trail cameras in time-lapse mode. These cameras are designed to be left unattended for extended periods of time and are equipped with protective casing against climate elements, large data storage capacity (32GB) and a solar power source with back-up batteries. An important aspect in static close-range photogrammetry is acquiring imagery at a range of baseline and vertical offsets to reduce the systematic image distortion and to improve SfM models (Chandler *et al*., 2002; Fonstad *et al*., 2013; Micheletti *et al*., 2015). In this study, the cameras were placed approximately 5 m apart and approximately 25-70 m away from the slump headwall, corresponding to a baseline offset approximately between 1:5 and 1:9. Additionally, the cameras were mounted between 1 to 2.2 m above the ground surface, with half of the cameras perched on ground 1-2m above the surround terrain, further increasing the range in elevation offsets.

To ensure a balance between proper image overlap (> 60%) and level of photographic details, the camera array was organized into two groups, largely determined by the morphology of the target and available installation points (Figure 5). Cameras 1 through 5 were positioned in front of the slump, approximately 50 m away from the center of the feature. The alignment provided nearly 100% overlap as they captured the entire slump in their field of view. A small stream cutting through the slump floor forced installation of cameras 6-12 to be somewhat separate from the first array. This second array sat on a topographic high above the stream, and was also closer to the target, at approximately 30 m distance. At this distance, a smaller portion of the slump was captured at approximately 70% overlap, intending to provide higher level of detail of the slump floor and headwall. The first two cameras of this second array, cameras 6 and 7, were oriented towards the eastern-portion of the slump floor in attempt to capture the area experiencing the most movement in summer 2015, as well as to act as a bridge of overlap, joining the two array groups. All cameras were mounted to iron posts that were drilled at least one meter into the permafrost to help avoid camera movement during the study period, minimizing data loss due to shift in orientation (Figure 6). The cameras were programmed to acquire images at hourly interval from June to September 2016, providing a redundancy of daily imagery that increased the likelihood of obtaining a set of daily imageries under optimal conditions. This is an important aspect since SfM algorithms are sensitive to certain environmental conditions, namely textural differences between images and sun angle causing shadowing (Micheletti *et al*., 2015). Texture-poor targets or surfaces such as snow or water can cause issues for the algorithms and should be avoided (Fonstad *et al*., 2013). In the case of thaw slumps, the moist soils on the floor of slumps were of concern due to their high reflectivity and the SfM software had issues to reconstruct this component (see section below). The presence of low sun angles can cause

shadowing that creates issues as the algorithm cannot find unique pixels to match in black patches. Shadows can also be problematic in time-series datasets from static cameras as the sun's angle will change between cameras and over time, thus modifying illumination between images. In this case, the algorithms have issues when the illumination of the same object changes throughout the photo set, reducing accuracy of reconstruction.

In all SfM applications, the installation and use of ground control points (GCPs) in the photographic frames helps the algorithms to find distinct and recognizable features in the frame and to transforms the models into real world coordinates. Manually surveying the location of GCPs with high precision allows for model quantification. The accuracy of this scaling is an important consideration, and provides a metric of the internal quality of 3D reconstructions. However, recent advances in the photogrammetry have removed the need for GCPs in SfM applications. The advancement stems from improvements in UAV hardware and in the record of the camera's shutter timing with onboard survey grade GPS. This now allows decimeter-scale SfM model accuracies, which were not possible with former camera EXIF data. This advancement has been coined 'fodar' (portmanteau of photo and LiDAR) and is considered survey-grade SfM photogrammetry (Nolan & DesLauriers, 2016). Although never tested, this concept is also applicable to ground-based stationary cameras, like in this study. Thus, in addition to the intended survey of GCPs, the locations of the trail cameras were recorded with high accuracy using differential GPS in August, 2016 by Rob Fraser to transform the SfM reconstruction into real-world coordinates.

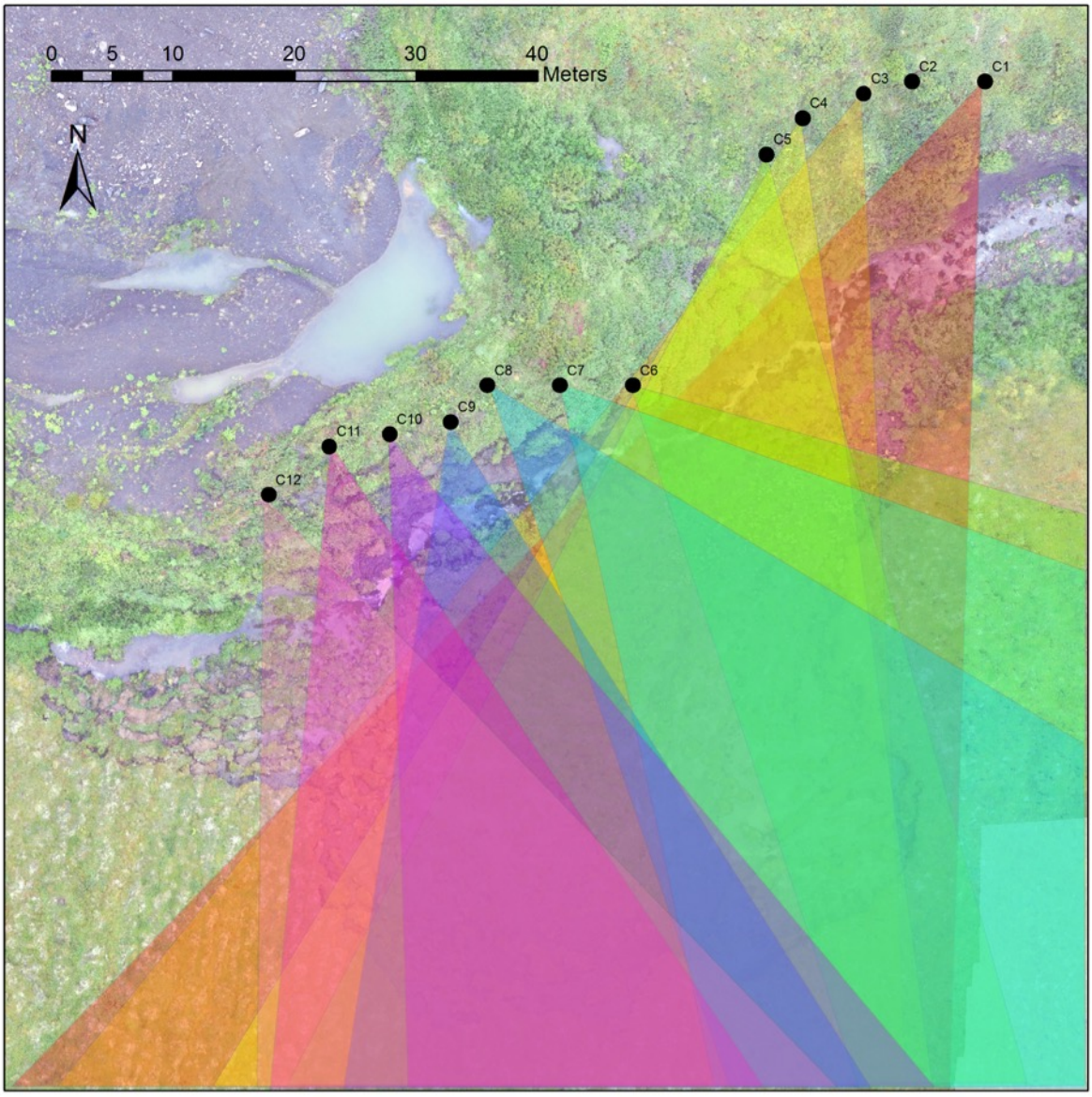

Figure 5. Geometry of camera array and associated fields of view.

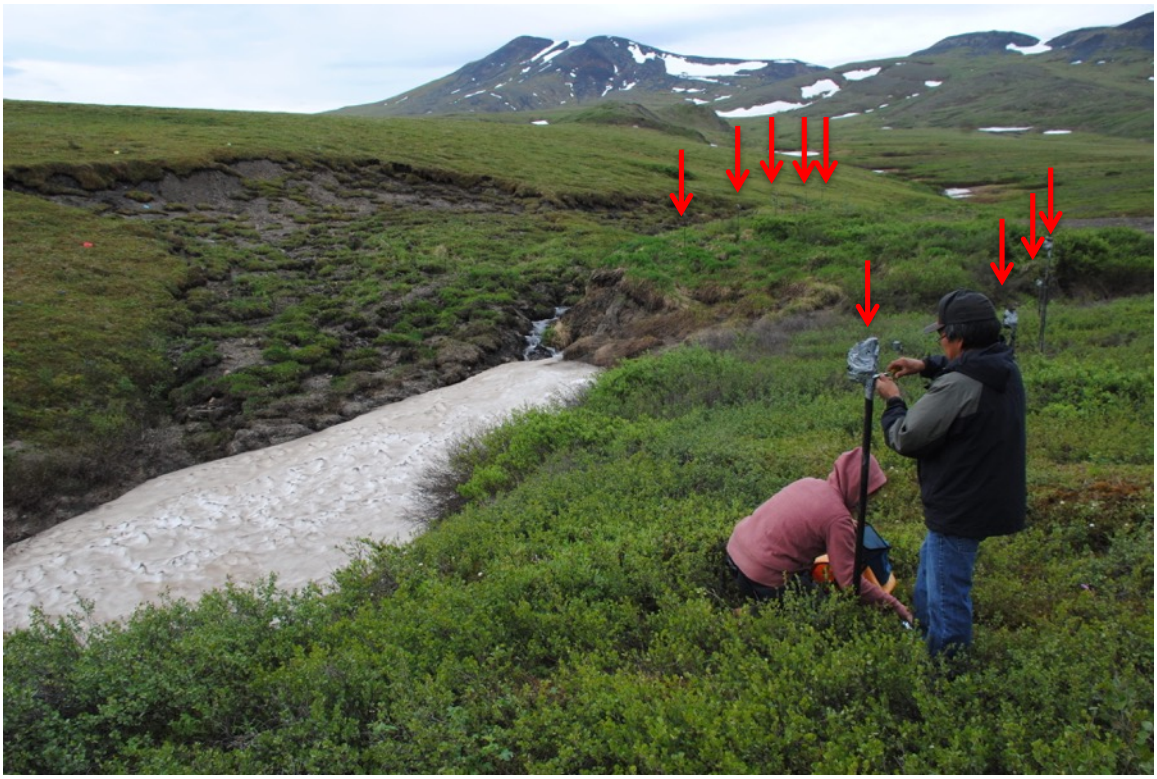

Figure 6. Example illustrating some of the cameras in the array, indicated by red arrows.

Figure 7. Close up example of a camera in the array.

4.2 Data post-processing

4.2.1 Processing UAV imagery and rectification to real-world coordinates

The imagery captured by the UAV in 2016 was input to Agisoft Photoscan and was initially aligned with the onboard camera's EXIF data, which provides latitude and longitude coordinates for each image. After initial alignment, camera calibration and georeferencing was optimized using four dGPS surveyed GCP targets before the dense cloud was generated. These GCPs were not present during the installation of the ground camera array in June of 2016, and those GCPs installed at that time were not surveyed on the UAV acquisition day, August 1st, 2016. The Agisoft Photoscan processing report for the 2016 UAV model reports a GCP RMSE at a sub centimeter level. However, when comparing stable features (recognizable objects above the headwall) between the 2015 and 2016 UAV models, there was an approximate distance of 2-4cm between those objects. This estimated accuracy was more conservative and assumed as more representative of the true registration accuracy of the full model.

4.2.2 Processing stationary camera imagery and rectification to real-world coordinates

Out of the 12 cameras, 11 cameras collected hourly images for 72 days, which resulted in approximately 20,000 images. The images were manually audited to remove those captured at night (triggered infrared setting), those captured during precipitation events, those with poor light conditions, and those occurring during periods of rapid terrain deformation. Although cameras were programmed to capture once each hour, the time-stamp of each image varied between and within cameras from 56 to 103 minutes. This caused an offset in the timing of image capture that compounded over the study period of 72 days. This limitation made possible only 8 sets of data (June 27, July 7, July 17, July 25, August 1, August 3, August 14, August 20, September 2) which provided the images for use in SfM modelling. Each dataset contained an image from each of the 11 cameras (camera 2 failed two days after installation) which were grouped in folders by date, as the input data for modelling.

The point clouds of the slump were derived using Agisoft Photoscan (Agisoft, 2013), a SfM software suite that is automated in its implementation of matching algorithms, but still allows for comprehensive customization of processing options. The software's algorithms use the images of each dataset as input and begins the point cloud reconstruction by either: 1) estimating the location of the camera in the dataset (it does this by using the objects in the images as a guide, iteratively identifying where each camera was, and therefore the location and geometry of what it was seeing when the photo was taken); or 2) the user providing the locations of camera from dGPS survey (with known camera coordinates, the algorithms can make estimations of target geometry to a higher degree of precision as there is no error introduced by the camera location estimation). Here, we provided the coordinates of the 11 stationary cameras obtained from handheld Garmin GPS (lower accuracy) and from dGPS (high

accuracy). However, Photoscan was unable to align the 11 cameras or successfully reconstruct the slump. Therefore, a series of different steps were performed in attempt to ameliorate the reconstruction of the slump into point clouds (Figure 8).

The first step taken in attempt to ameliorate the SfM reconstruction involved masking the images within the software to remove the SpyPoint banner and the background sky and mountains (Figure 9). This allowed elimination of unnecessary information on the images, without altering image dimensions, which is known cause of reconstruction failure. Masking the images led to successful reconstruction of the images in various datasets of 9 out of 11 cameras. The two consistently omitted images in each dataset were from cameras 6 and 7 (one from each camera), were pointing towards vegetated areas, which are also known to confuse SfM algorithms (Agisoft, 2013). Additionally, these cameras were centrally positioned in the full array and represented the bridge between the two groups of camera. Excluding these cameras from the SfM model reconstruction reduced the error they introduced, but also segregated the slump into two sections, or "chunks", as termed by Photoscan.

An additional option in Photoscan that has great influence on success of camera alignment was the key and tie point limits, which dictate the number of feature points to be considered during reconstruction. Experimentation with the values found that alteration influenced not only the quality of reconstruction, but whether alignment was successful: employed values for success were key point limit equal to 100K and tie point limit equal to 5K. Higher values did not improve results, but significantly increased processing time. In addition, the depth filtering reconstruction parameter controls the influence of points that are sparse or distant from a connecting surface. Modification of this parameter causes a variety of impacts depending on the dataset in use and required experimentation. Poor-texture of some elements in the image, noisy or badly focused images can cause outliers among the points. To address the outliers, PhotoScan has several built-in filtering algorithms (Agisoft, 2013). In this case, mild-depth filtering caused models to contain erroneous panes of discontinuous surface, and aggressive-depth filtering caused them to appear sparse and stretched towards outer boundaries. Setting the depth filtering to moderate helped maintain the detail in the complex surface texture and allowed obvious outliers to be removed.

The second step taken in attempt to successfully reconstruct each dataset with the images of the 11 cameras involved trying to calibrate the camera lenses with the automatic calibration software Agisoft Lens. The Agisoft Lens software uses a computer screen with a checkerboard grid as a calibration target. The software is meant to estimate the full camera calibration matrix, including non-linear distortion coefficients. The estimates are then imported to Photoscan for use in camera alignment. The images captured are meant to only include the screen at a variety of angles, with no other surrounding features,

including the computer screen frame. Unfortunately, without a view finder, manual focus and shutter on the SpyPoint camera, proper capture of the calibration target screen with the camera was very difficult (attempt to acquire camera parameter information from SpyPoint was unsuccessful). Despite extensive efforts (trying to trigger cameras with time-lapse and motion sensor settings), resultant calibrations corrections were poor and entirely unreproducible as repeat calibration was not able to produce consistent results. Given the lack of ability to control potential introduction of error, the avenue was abandoned.

The third step taken in attempt to ameliorate the reconstruction of each epoch with the images of the 11 cameras involved "4D processing" capability in Photoscan which allows for dynamic scenes captured by static synchronized cameras to be processed together as "multi-frame chunks", rather than as separate epochs. This multi-frame aggregate method offers several advantages: 1) no alignment between chunks is necessary as they are processed in a batch, and therefore share a coordinate system; 2) the photo alignment is often improved as the alignment process includes all the photos in the dataset; and 3) the processing workflow is simplified as each step is applied to the entire sequence, which is not the case in processing of individual epochs of data. Nonetheless, this processing method was unsuccessful in the point clouds reconstruction of the thaw slump. Only a portion of the cameras were aligned and the estimated reconstruction error was reported as greater than 5 m, and the camera positions were visually heavily misaligned.

The fourth step taken in attempt to ameliorate the reconstruction of each epoch with the images of the 11 cameras involved improving the variation in illumination conditions in the dataset. This was an issue between different cameras viewpoints acquired at the same time-stamp and also at the same camera with images acquired over very short time-interval. Figure 10 provides an example of the difficulty in finding images for modelling each dataset for which lighting conditions are similar, even when images from two cameras only 20 m apart (cameras 1 and 3) were taken 13 minutes apart. It was thus considered that poor modelling results could be due to illumination inconsistencies between photographs from each camera and between them, and attempt to alleviate this effect was done by colour matching the images in an epoch using GIMP software. Each image`s three colour channels were individually adjusted to closely match those of one image in the set for which illumination was favourable. This adjustment doubled the file size of each image, to approximately 2MB, in some cases 4MB; however, it led to only 4 of 11 cameras being aligned.

With no improvement to obtaining a contiguous SfM reconstruction of the slump, processing continued from the initial multiple chunk results attained after masking and removal of the images from camera 6 and 7 in each epoch (Figure 11). Photoscan allows multiple point cloud models to be merged after being independently reconstructed with overlapping points. The SfM slump model was therefore

reconstructed in two chunks (two groups of cameras; cameras 1-5 and 8-12, noting camera 2 failed and cameras 6 and 7 were removed from the chunks) and then merged. Despite extensive effort to improve reconstruction, the resulting reconstructions were discontinuous, as well as non-overlapping between datasets in many instances. GCPs occurring at the same target between chunks are normally used to anchor the `chunks` to each other; however, the reconstructions were not able to model the entire slump and reconstructed only the headwall; the slump floor was not modeled likely due to the wetness and highly dynamic nature that confused the SfM algorithms. The GCPs installed were placed around the periphery of the headwall and on the slump floor, but neither area was successfully modelled in full. None of the GCPs surveyed by the UAV team were located in the reconstructed chunks, removing the ability to merge them using known points. Thus, an alternative solution was sought. Three of the GCPs installed during the array installation, directly above the most commonly modelled area of the headwall were visible in a portion of the imagery. These GCPs were also visible in the UAV reference model since the UAV survey was executed two months after the array installation. The modelled coordinates of these GCPs were extracted from the UAV model and provided to Photoscan before photo alignment. Although only as accurate as the UAV model (approximately 3 cm), these "pseudo GCPs" provided the anchoring points required to merge subsequent chunks, as it would be the case were dGPS-surveyed GCPs available. After introduction of the "pseudo GCP" coordinates, the software was able to align and merge two chunks (4 cameras in one chunk, 5 cameras in the other) of modelled data for each dataset. This process was repeated for each dataset, which provided eight models of the target slump as it changed over time. The modelled data each covered most of, or the full headwall of the slump. The remainder of the slump, including the slump floor, toe, creek and periphery were not successfully reconstructed.

The resultant point clouds were exported in different formats including .txt and .las files, which are text strings of the coordinates of points in point clouds, and .tiff files, which store rasterized DEMs and orthophotos. These products can be considered the raw results of the proposed method and served as DEMs for change detection and deformation analysis between sequential datasets.

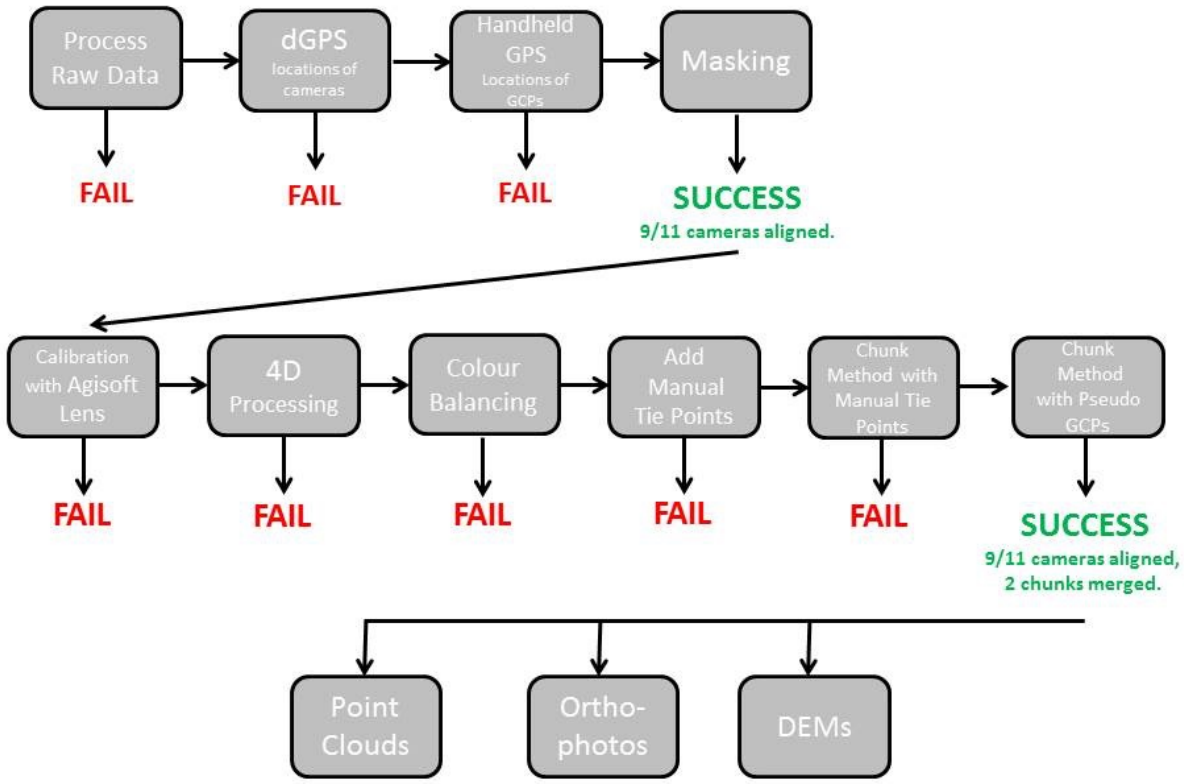

Figure 8. Workflow diagram of processing trajectory in Agisoft Photoscan.

Figure 9. Example of input image masking in Agisoft Photoscan.

Figure 10. Example of variable lighting between adjacent cameras over short time frames.

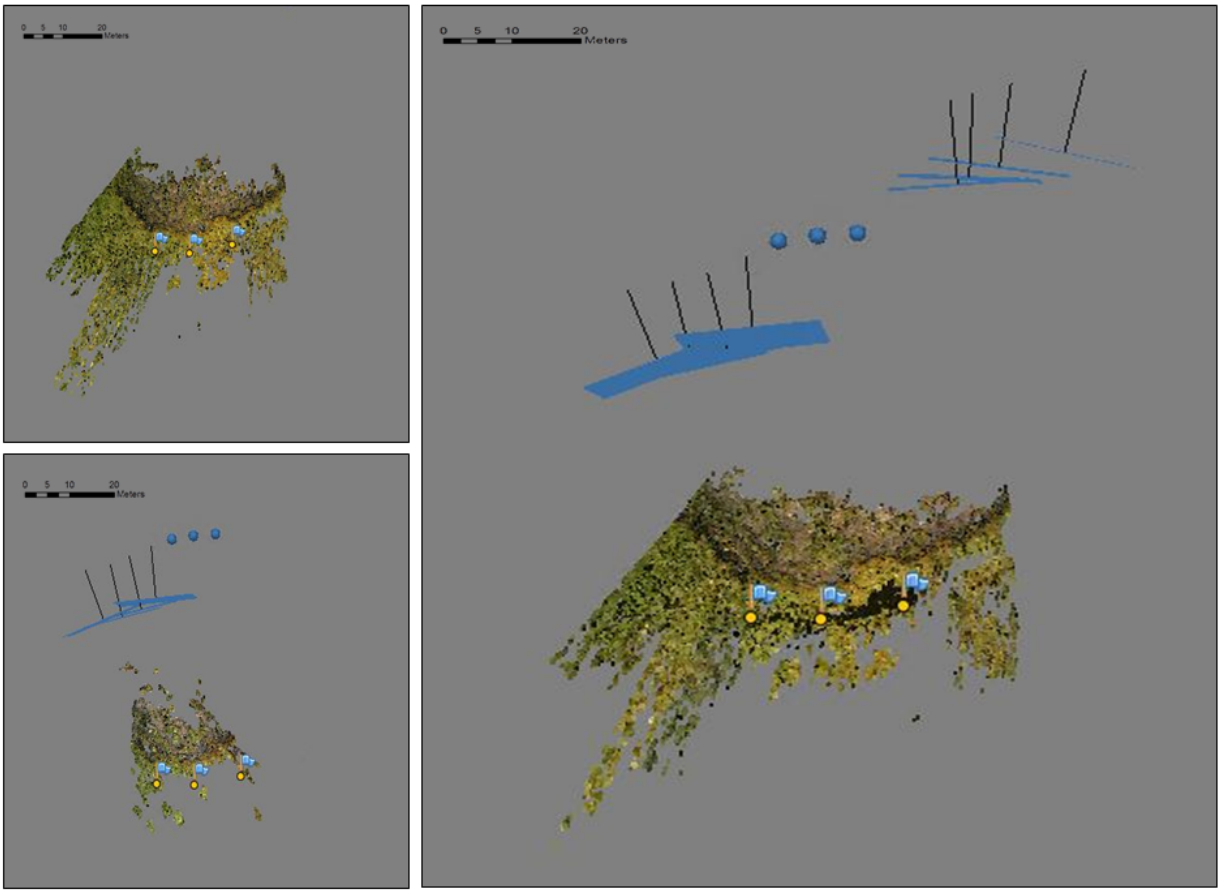

Figure 11. Example of resultant two point cloud chunks (left) which require subsequent merging (right) via use of pseudo GCPs (blue flags). Estimated camera positions indicated as blue squares, and unaligned cameras indicated as blue circles.

4.2.3 Accuracy of reconstructed stationary camera point cloud models

In SfM methodology, it is important to quantify the accuracy of the reconstructed point clouds relative to known points or another model of known quality, especially since in this case the generation of the point clouds model was not straight-forward, and their accuracy is a function of the algorithm's interpretations. Traditionally, model accuracy compares locations of objects in the models with their known coordinates from a dGPS survey; however, this was not possible here. A LiDAR dataset is available for the study area, however it was obtained in by the GNWT in 2012 (landscape and the slump has changed since then) and its spatial resolution is coarser (30cm cell resolution) than the point clouds model. In Figure 12, hillshaded LiDAR data of four RTS are shown, including D1. The mega slumps Charas and Melanie may be large enough to employ LiDAR for change detection, however for CB and D1 that may not be the case (Figure 12). The red line in the D1 tile of Figure 12 delineates the 2016 extent of D1 as indicated by the UAV data employed in this study. At the time of LiDAR acquisition in 2012, D1 was much smaller, as seen by the shaded depression near the toe of the 2016 extent. This available data was therefore inappropriate for accuracy assessment. It was thus decided to compare the quality of the stationary camera point cloud models to the 2016 georeferenced UAV survey using the Cloud Compare software (www.danielgm.net/cc; EDF R&D, 2012). Pseudo GCPs were used for anchoring to the UAV model. Therefore, comparison of the point cloud of each modelled epoch to the UAV reference data, in the form of distance/difference computation using a variety or algorithms and methods, would be used as surrogate accuracy. Upon import of each dataset's point cloud, visual inspection isolated poorly modeled portions and these were removed. These poorly modelled sections were often small portions of disoriented surfaces at some distance from the main contiguous surface (Figure 15a, b). Removal of these portions from models was justified on the basis that these areas would increase error in the subsequent cloud comparison results which would not be representative of the modelled headwall area.

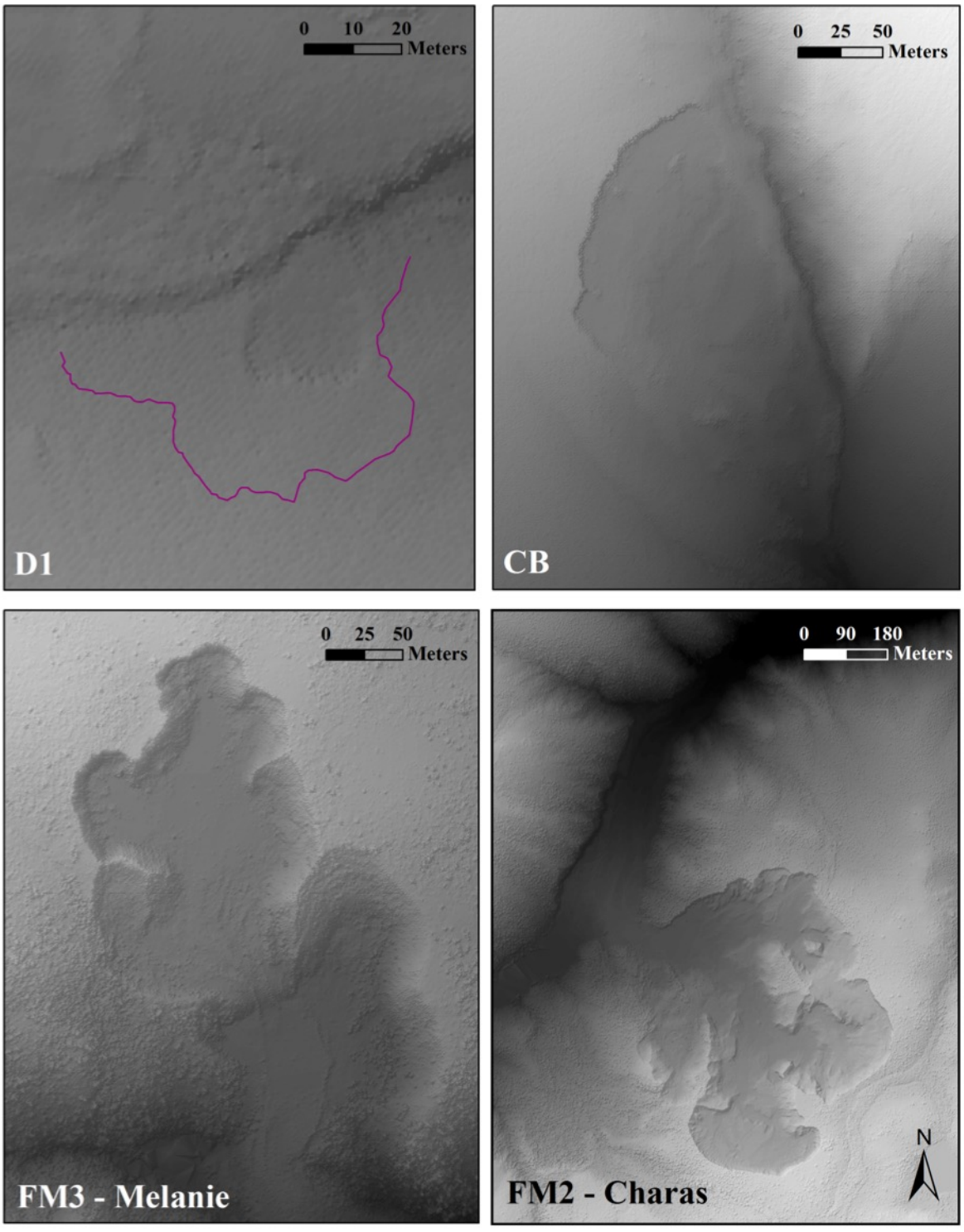

Figure 12. Retrogressive thaw slumps of the Peel Plateau, NWT, on LiDAR data acquired in by the GNWT in 2012.

4.3 Change detection and deformation analysis

There exist different methods for change detection and deformation analysis. The most common is DEM differencing (DoD), however this method is not always appropriate for complex topography, as is the case for this study. A 2D DEM introduces error and biases on vertical or overhanging surfaces and limits the resolution of results as output to a fixed grid size (Lague *et al,* 2013). Furthermore, the spatial distribution of surface roughness cannot be well represented by a regular grid and will always therefore include interpolation and resampling. Solutions to this issue exist by performing point cloud comparisons that consider the 3D geometry of a target without the requirement to resample to 2D. This is particularly advantageous in natural environments as surfaces are often non-planar and complex. However, these methods have been scarcely used and are not adapted to complex natural surface with high degrees of topographic heterogeneity as they often improperly assign the normal angle from the modelled surface due to heterogeneity in small scale roughness (Lague *et al,* 2013). To address this issue, the normal angle must be derived at a scale appropriate to the surface local to the points being used in calculation. Natural surfaces, subject to a variety of processes which can register as displacement such as differential erosion, sedimentation or vegetation growth, often cause a lack of homogeneous portions between datasets. For this reason, it can be difficult or impossible to register datasets based on unchanged regions to allow quantification of those regions which have changed. In this case then, we address change detection and deformation analysis in complex topography lacking corresponding elements among successive point clouds.

Given the complexity of the modeled feature, three differencing methods were tested for the aerial and ground-based SfM: DEM of Difference (DoD), Cloud to Mesh (C2M) and Multi-Scale Model to Model Cloud Comparison (M3C2). For comparison against cloud differencing methods, each epoch's un-interpolated DEM was differenced against the UAV georeferenced DEM, translated to points and then interpolated with Kriging to allow visualization. The differencing results from the various methods were then symbolized spatially in ArcMap on a common scale and overlaid onto the georeference UAV orthophoto to allow visual comparison of spatial distribution of the epoch results (Appendix A). To investigate the data further, each epoch's data was culled to include only the extremes in the data. This was done by isolating the lower and upper 10% of the data and visualisation of where these extremes occurred spatially. This analysis allowed determination of whether this outlying data should be considered error or signal depending on its position on the slump surface.

4.3.1 DEM differencing (DoD) for headwall retreat rate, volume loss estimation and comparison to UAV reference data.

Due to the discontinuous nature of the DEMs from the stationary camera point clouds, DEMs were interpolated from each of the eight datasets into continuous surfaces using the Kriging interpolation algorithm. The DEMs were re-sampled to points and re-rasterized instead of using the raw point cloud files. Although interpolation intrinsically introduced errors in the raw results, it was deemed necessary to move forward with the change detection and deformation analysis. This process was not required for the UAV data as it was not discontinuous in nature. The UAV DEMs were employed for the DoD production without interpolation, however the datset before and after (August 1 and August 14) the UAV dataset were resampled from 1cm to 2cm resolution to allow DoD production at the same scale. The annual UAV DEMs were differenced for DoD production without resampling as they were both 2cm resolution, and were included in the differencing method analysis. Interpolated DEMs from each dataset were then differenced in paired sequence, representing the change in surface elevation between successive epochs. The UAV data was captured on August 3rd, 2016, and for the purposes of the DoD production for subsequent headwall volume and retreat rate estimation, was included to create additional epochs among those derived using the proposed acquisition method.

Calculating DoD for subsequent determination of geomorphic change in terms of volume loss and headwall retreat rate was achieved by differencing DEMs of two datasets using the following equation:

$$\Delta xy = Z_{xy} - Z_{ixy}$$

Using raster calculator in ArcGIS ArcMap software, the DEM from a dataset i (initial) was subtracted from the DEM dataset i+1. The resulting values in each pixel represent the change in surface elevation as positive or negative values. The interpretation of the increase or decrease in elevation (erosion, deposition, error, etc.) depends on the knowledge of the target and its processes and behaviors (James *et al*., 2012).

Using the orthophotos of each dataset, including the UAV georeferenced orthophotos, the location of the headwall of the slump was manually digitized for each. The headwall delimitation from the first dataset was then overlain by that of the second. The two headwall extents were then merged into a closed polygon, which represented the horizontal extent of the headwall retreat over the epoch. The polygon was then used to reduce the epochs' DoD to the area which was best modelled. In doing so, the error associated with interpolation was reduced to only that where the raw DEM was most reliable and required the least intervention. Additionally, clipping the DoDs to represent only the area of headwall retreat allowed quantification of the volume lost in that area between datsets, as well as estimation of retreat rate over all epochs.

The resultant clipped DoD's general statistics were exported in table format and used to calculate volume lost from the modelled headwall region and retreat rates using the following equations:

Volume of Material Lost from the Headwall Region = Cell Resolution * Sum of Cell Values

$$V = Xm^2 * \sum (DN)m$$

Rate of Volume Loss = Volume (m^3) / Epoch Length

Headwall Retreat Rate = Average distance between headwall extent (m) / Epoch length

To compare the modelled datasets to that of the UAV derived data, cross sections of data were extracted from each dataset along the same line which fell from the headwall to the slump toe (Figure 18). The cross sections were then plotted together to investigate if the headwall was modelled over time in the positions one would expect.

4.3.2 Cloud to Mesh (C2M)

The first 3D cloud comparison method used was 'Cloud to Mesh' (C2M), in which a mesh is constructed based on the average point cloud position and used for comparison to other point clouds. Like DoD, mesh surface derivation introduced interpolation where data is sparse. Although several algorithms are available, two meshing algorithms were investigated in this study as they were readily available in the open sourced 'Cloud Compare' software, for which any potential user of the proposed data capture method has access. The first meshing algorithm, Delaunay triangulation (Shewchuk, 2002) minimizes long skinny triangles caused by sparse data in occlusion shadows or towards data boundaries (Barnhart & Crosby, 2013). The algorithm computes a Voronoi diagram for all the points in the cloud and uses it as a guide to triangulate a surface over the diagram (Maiti & Chakravarty, 2016). Delaunay triangulation is recommended for planar surfaces with minimal jumps or gaps in surface continuity. This is not the case with the datasets in this study, which contain not only surfaces of various orientations, but with inconsistencies in the transition between those orientations. Delaunay triangulation is also highly sensitive to data noise, and is known to create artifacts (Cloud Compare, personal communication). This meshing algorithm is recommended for cloud comparison where the input data has very little noise, and confidently represents the target they represent.

Poisson surface reconstruction (PSD) (Bolitho *et al.,* 2009) smooths data and therefore can navigate noisy data more readily. However, it's possible that smoothing may also suppress real features and alter the change signal. PSD is meant for application to closed 3D surfaces, which the datasets also do not represent. This algorithm aims to use calculated normal angles to each point to reconstruct a surface based on minimizing the difference between those normal angles (Maiti & Chakravarty, 2016). This meshing algorithm may be used with unclosed 3D surfaces, however special attention must be paid to

ensuring calculated normal are robust. For this study, Cloud Compare's "calculate normals" tool was employed to allow uniform treatment to each dataset, as manual assignment of normal angles would be time consuming, and difficult to ensure equal confidence between datasets. Poor normal calculation is most common in areas where data is sparse or where slope changes quickly, both of which conditions occur in the datasets representing the targeted feature, and can lead to bubble shaped artifacts in results (Cloud Compare personal communication).

C2M differencing's performance then rests in the quality of the mesh produced. None the less, even if a perfect mesh is created, C2M could still under-report cloud to cloud distances as it is based solely on minimum distance between points, regardless of orientation of surrounding points.

4.3.3 Multi-scale Model to Model Cloud Comparison (M3C2)

Multi-scale Model to Model Cloud Comparison (M3C2) does not require or employ a meshed surface, which not only reduces processing time, but also the error associated with poor mesh representation of point clouds. M3C2 (Lague *et al,* 2013) attempts to reduce cloud differencing error in complex topography by introducing a small search region around each point, which is used in calculation of the normal angle from each point to the surface estimated in that search region, ensuring the deduced normal angle is representative of the surface orientation of that particular point. Figure 13c provides a diagram describing the process. If the normal angle is measured at a scale too small with respect to the surface roughness characteristics (or instrumental noise), its orientation will vary strongly (Lague *et al,* 2013). This complexity may tend to overestimate the distance between the two clouds. The quality of M3C2 results are then closely related to the quality of the normal angles computed (similar to the quality of meshes in C2M), which if automated is influenced by the point cloud density. In this study, the values selected as inputs (Table 2) to the M3C2 algorithm were estimated by Cloud Compare (EDF R&D, 2012). The core points were derived by Cloud Compare's subsampling algorithm and provided a minimum distance between core points as reported in Table 2. Similarly, the search region for normal angle derivation was estimated by Cloud Compare as a percentage of the point cloud's extent (bounding box). User defined values require a thorough understanding of each data set's individual heterogeneity and the potential spatial distribution of varied magnitude in said heterogeneity. Given the variety intrinsic to natural environments, it is unlikely that a unique solution could be applied to all normal calculations (Lague *et al,* 2013). User overestimation and underestimation of the normal or projection scales cause a variety of complications which can degrade resolution and increase errors. It is possible that the default estimated values may be smaller or larger than the local roughness surrounding any particular core point.

M3C2 also includes other calculated attributes of the results, including report of the spatially

variant confidence interval (SVCI) estimated using local roughness and point density, which informs the statistical significance or lack thereof, of the change measured at any point. There remains question of the effect of local surface roughness, and the choice of search radius scale in relation to local surface roughness. A thorough understanding of, or empirical model to correct for this limitation is yet to be developed (Lague *et al,* 2013), and was therefore not used in this study.

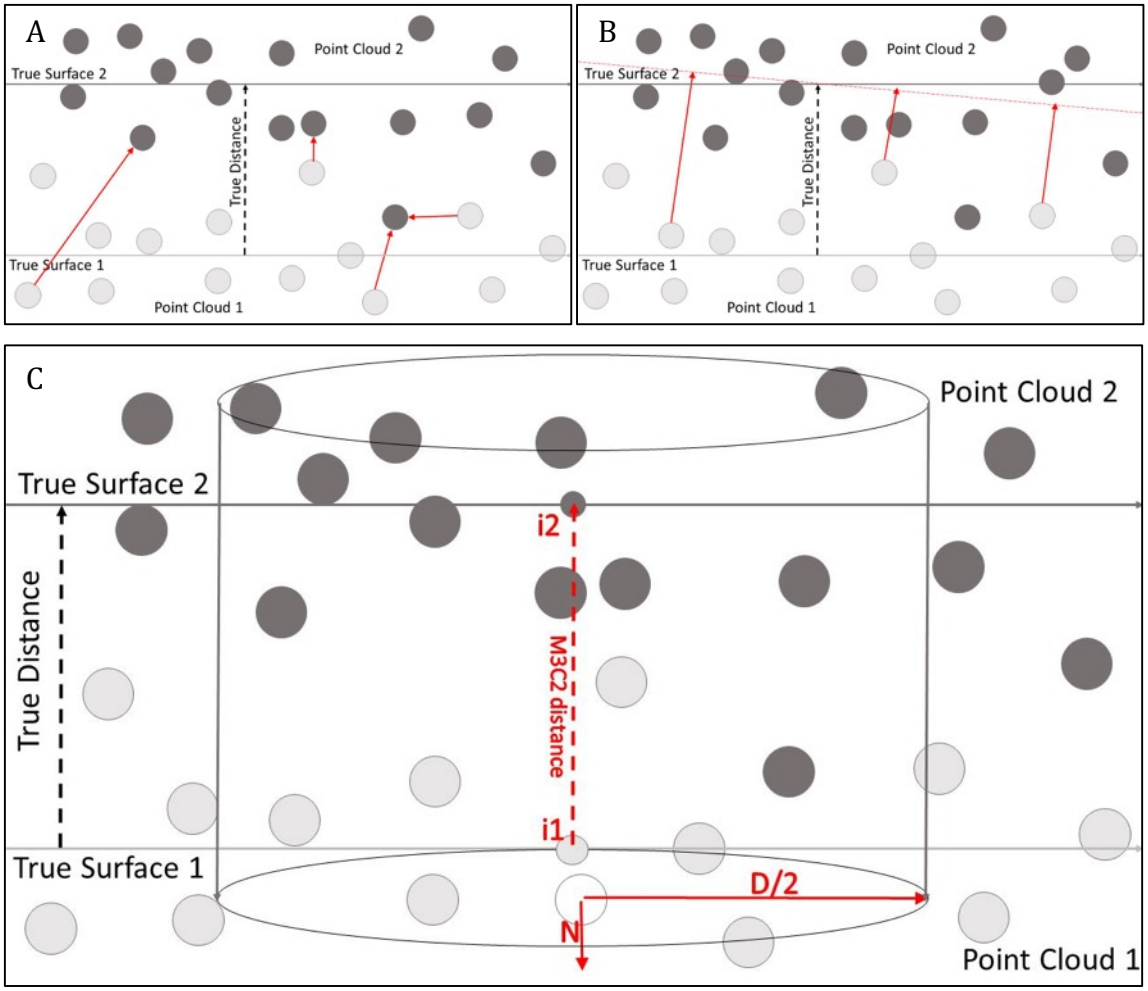

Figure 13. Adapted from Barnhart & Crosby, 2013.
A) Cloud to Cloud Distance. True surfaces are represented as point clouds, which include error as noise. Without knowing which direction is normal to the true surface, distances reported represent the closest point in point cloud 2 to the point in point cloud 1. This can result in underestimation of distances between surfaces. Additionally, the closest point in the compared or referenced cloud can be outliers, also leading to underestimates of distance between surfaces. This method is therefore less appropriate for data sets with high surface roughness or sparse clouds. **B)** Cloud to Mesh Distance. Building a mesh of the reference cloud averages the position of the point cloud, and provides the proper normal angle to the modelled surface. Although error is associated with averaging the point cloud into a mesh surface, underestimation is reduced by removing the influence of outliers and poor normal angle selection to one of the data sets. If the mesh properly estimates the position of surface 1, then the estimated distances are the true distance, plus or minus scatter/noise. **C)** Multi-scale Model to Model Comparison (M3C2). Step 1: A subsample of "core points" from the reference cloud is isolated for comparison against all cloud points to reduce

processing time (represented by hollow point). For any given core point, i, a search radius of D/2 is used to define the angle normal (N) to the collection of points with the radius. Step 2: 2 sub-clouds are defined by the intersection of the reference and compared clouds with a cylinder of diameter *D/2* and axis (*i, N)* which gives a distribution of distances along the normal direction. These are used to define the mean position of each sub cloud, *i1* and *i2*. The distance between these points is reported as a M3C2 distance for that core point.

Table 2. M3C2 input parameters estimated by Cloud Compare based in input data (in meters).

Epoch	D and d (search radius for calculation of N and i (1 and 2))	Depth (height of cylinder)	Minimum distance between core points
June 27	0.743029	3.715146	0.371515
July 7	0.506050	2.530248	0.253025
July 17	0.695463	3.477317	0.347732
July 25	0.642246	3.211230	0.321123
August 1	0.709257	3.546284	0.354628
August 14	0.683531	3.147655	0.341766
August 20	0.697590	3.487951	0.348795
September 2	0.765758	3.828792	0.382879
Annual	1.386175	6.930876	0.693088

5. Results

5.1 Aerial SfM model of D1 slump

The SfM modelled results of the two UAV surveys (July 27th 2015 and August 3rd 2016) are shown as orthophotos in Figure 14. The D1 slump is a small (approximately 0.5 ha), north facing RTS with a horse shoe shaped headwall, and a small creek at the toe running perpendicular to the hill slope. Over the year of imagery acquisition, changes in D1 slump were observed in terms of headwall retreat, areal extent and section of stabilization. D1 slump also expanded significantly, namely in the south-east section of the headwall. In a similar fashion to the retreat pattern seen at Charas and Melanie slumps over the last decade (Figure 3), D1 slump exhibits differential retreat rates along the headwall, leading the headwall to begin development of two lobes. At the center of D1's headwall, a small region appears slightly resistant to backwasting, causing a small tongue of material to remain un-degraded. The differential retreat along the headwall is likely caused by differences in ground ice content in the thawing permafrost. However, it's also possible that the slope on the east side of the slump is not sufficient to allow continued headwall retreat. No permafrost samples were collected at D1 to confirm such an assertion. Based on differences in vegetation cover on the slump floor, the lower section of the floor appears to have stabilized given the more abundant vegetation in 2016.

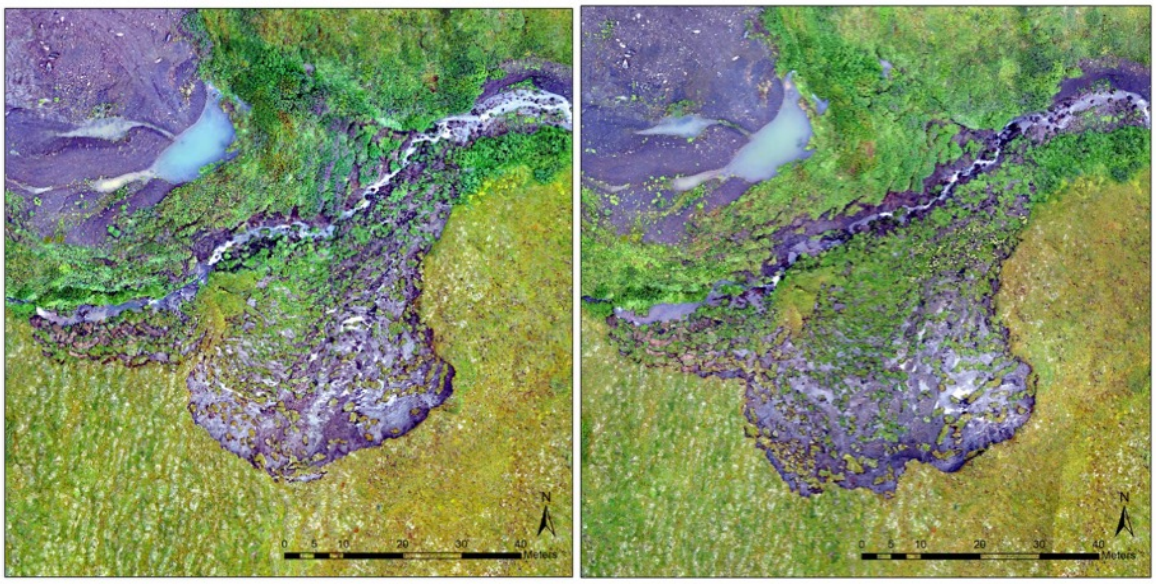

Figure 14. Orthophotos of SfM models derived from UAV imagery in July 27, 2015 (left) and August 3, 2016 (right). Courtesy of Robert Fraser, CCRS.

5.1.1 Quantifying changes between 2015 and 2016

Using the DEMs for DoD, and the point clouds for the three cloud differencing methods, the changes of the D1 slump were quantified using the 2015 and 2016 UAV data (Figure 15). The DoD was employed in estimation of headwall retreat rate and calculation of volume lost from the headwall. The DoD and three other differencing methods were employed in elevation change detection. Figure 15 illustrates the spatial distribution of change detected, where material is lost (negative change interpreted as erosion) from the headwall region, and the topographic high just north of the small creek, and material is gained (positive change interpreted as deposition) in the slump toe region at the topographic low where the small creek flows. The headwall retreat rate is estimated from an average of the width of the negative change signal (blue) at the headwall. Table 3 shows the minimum, maximum, range, median and mean change in elevation of each of the four differencing methods. The range in elevation change data varies between the differencing methods, from 5.863m to 12.457 m, with minimums (interpreted as erosion) ranging from -1.452 m to -6.627 m, and maximums (interpreted as deposition) ranging between 2.879 m and 5.830 m. The data means for each differencing method vary between 0.118m and 0.223m. The same data is represented in Figure 16 as a boxplot, containing the comparison of the UAV data over a year, using each differencing method. The mean of each method falls in a similar location near zero, and the whiskers (data extremes) varying widely. The M3C2 in particular has outlying negative data which lead to a large data range not seen in the other differencing methods. The similarity in data means between differencing methods and disparity in data ranges suggest the differencing methods are unable to estimate

data extremes consistently, and that the mean data can be interpreted as representative of the average change. The average also includes the immediate area surrounding the D1 slump which is considered stationary. The spatial extent of the analysis corresponds to the areas mapped in yellow, red and blue (Figure 15). The disparity in data range highlights the lack of consistency in the change detection results as provided by the differencing methods applied.

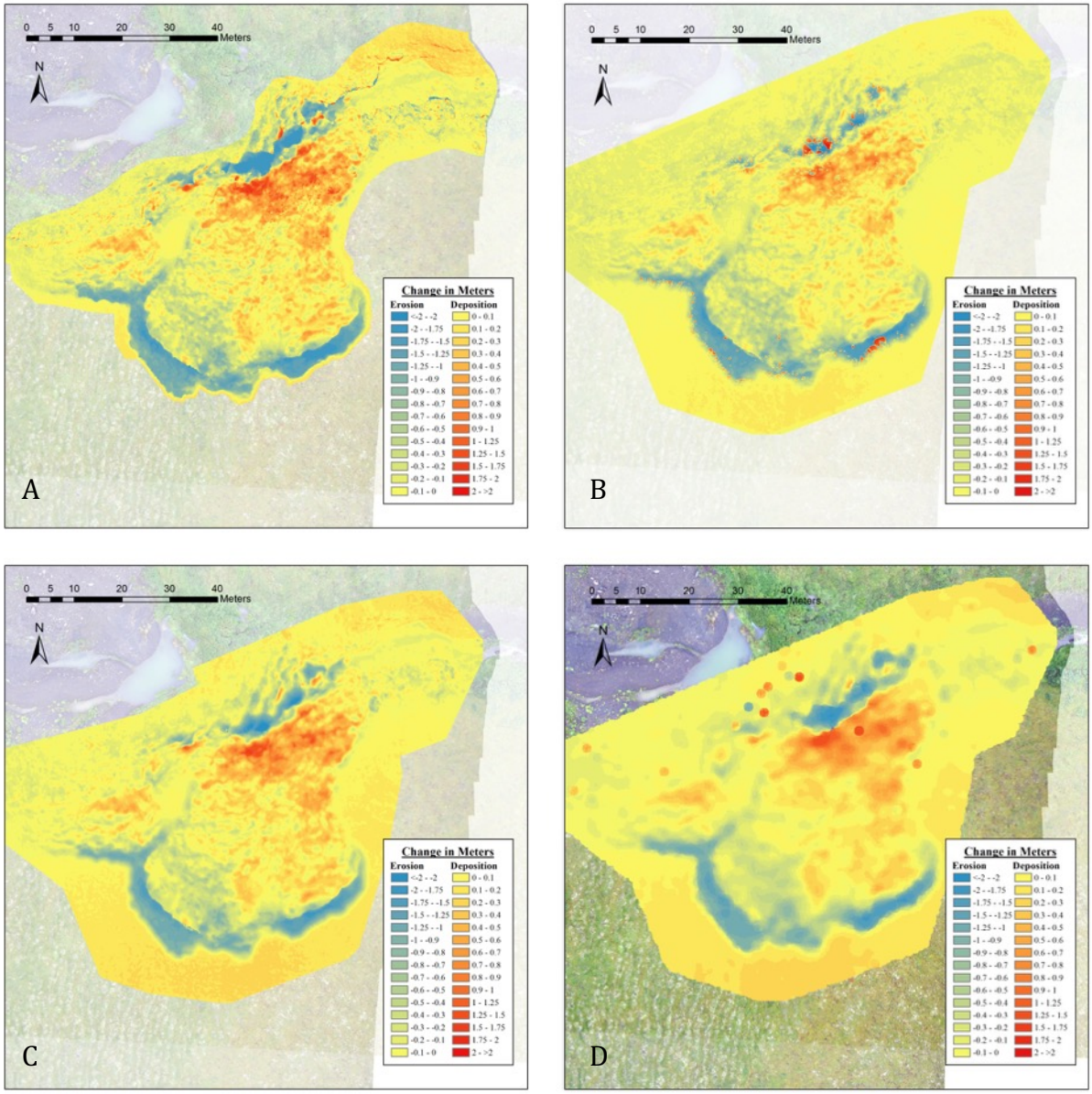

Figure 15. Elevation change results of SfM models derived from UAV imagery in July 27, 2015 and August 3, 2016. A) DoD; B) C2M distances (via Delaunay triangulation mesh); C) C2M distances (via Poisson mesh); D) M3C2 distances. Courtesy of Robert Fraser, CCRS.

Table 3. Elevation change over one year (July 27th 2015 to August 3rd, 2016) at D1 via four change detection methods (in meters).

Differencing Method	Minimum	Maximum	Range	Median	Mean
DoD	-3.271	4.892	8.163	0.127	0.223
C2M - Delaunay	-2.984	2.879	5.863	0.072	0.118
C2M - Poisson	-1.452	4.851	6.306	0.087	0.179
M3C2	-6.627	5.830	12.457	0.098	0.178

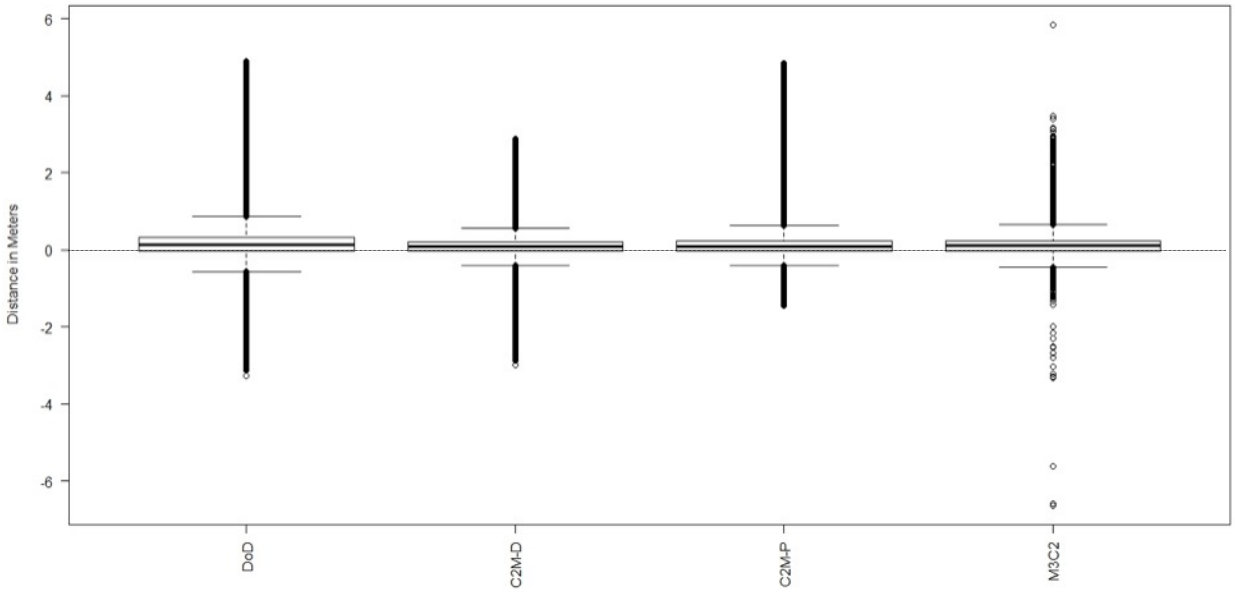

Figure 16. Boxplots of elevation change over one year (July 27th 2015 to August 3rd, 2016) at D1 via four change detection methods.

5.2 Ground-based SfM modelling of D1 slump

Eight point clouds of varying quality and density were produced, one for each dataset. The point density of each epoch cloud (Table 4) should be considered as averages as their densities are not uniform. The clouds for each dataset had point counts ranging from 1.5 - 4M points each, whereas the 2016 UAV derived point cloud had 12M points. Although the point clouds had a fraction of the points compared to the UAV reference cloud, their point densities were comparable (~2,500pts/m^2 for the UAV data versus ~1,000-2,100pts/m^2), suggesting that although the data was not able to provide the same areal extent as the UAV data (750 to 1500 m^2 compared to 5000 m^2), the area that could be modelled had data density comparable to that which could be acquired by a UAV with a higher resolution camera. The only exception was the July 7th data, which has point density of 5,400pts/m^2, caused by the highest point count over the smallest area. The variation in point count and density between datasets reflects the variation in appropriate imagery for SfM.

Figure 17 shows the orthophoto and raw modelling results for all eight datasets overlying the 2016 UAV orthophoto, which allows for visualization of the small spatial extent of the thaw slump which could be modelled relative to the UAV point cloud. Also visible in Figure 17 is an example of outlying modelled portions which were not connected to the headwall region, and were generally culled when possible. Although representing only a small region of the slump that was intended to be modelled, the orthophotos show relatively clear indication of the headwall position at each day captured, which was advantageous in allowing manual digitization of the headwall for retreat rate and volume loss calculation in the absence of a larger, more continuous model.

Based on the time-series June 27th – August 1 (Figure 17a-j), a portion of material in the center-right region of the headwall experienced slower retreat rate as evidenced by the development of a triangular point. In the epochs that follow (August 14 – September 2), we see this material erode and released into the floor of the slump as small clods (Figure 17k-p). Similarly, on the western side of the headwall, clod material is seen iteratively breaking away from the headwall and moving downslope into the slump floor. This activity is particularly apparent on the July 7th data. In some cases, particular clods can be recognized and tracked down slope between datasets. Surface material above the headwall at D1 is then falling into the slump floor over time, causing the headwall position to retreat. This resistant area is seen best on the August 20th and September 2nd epochs on the center-left region of the headwall (Figure 17m-p). These examples of more resistant headwall are similar to those seen in larger slumps, which often become islands of abandoned material in the slump floor. These islands or thaw resistant areas are thought to occur due to differences in permafrost matrix material and their associated frost susceptibility. Although not obvious in these results, the base height of the slump floor on which the clods sit, can be seen lowering over time in the source images collected by the trail cameras, when viewed in time-lapse. The rate of slump floor lowering was not consistent, and appeared to accelerate in the hours or days after precipitation events. This change in slump floor elevation increased the elevation difference between the slump floor and the surface beyond the headwall, leading to continued headwall retreat as surface materials lost underlying support and the buttressing effect of the materials in the slump floor. This change was most obvious on the western side of D1, contrary to the time-lapse imagery of D1 during the 2015 thaw season, in which the eastern side of the slump saw the most obvious flow and headwall retreat. The reasoning for this difference is not well understood. The increased temporal frequency of the ground-based SfM method, in combination with other information such as meteorological station could help decipher the intricacies of such behaviour.

Table 4. General characteristics of raw modelled epoch and UAV derived point clouds.

Epoch Date	Number of Points in Cloud	Area (m^2)	Point Density (pts/m^2)
June 27	2,565,026	1,482	1,731
July 7	4,068,255	748	5,439
July 17	1,517,326	1,487	1,020
July 25	2,182,996	1,101	1,983
August 1	2,779,416	1,542	1,802
August 14	2,499,876	1,590	1,572
August 20	2,892,855	1,366	2,118
September 2	3,183,310	1,889	1,685
August 3 UAV Reference	12,053,579	4,902	2,459

***UAV reference cloud included for comparison.**

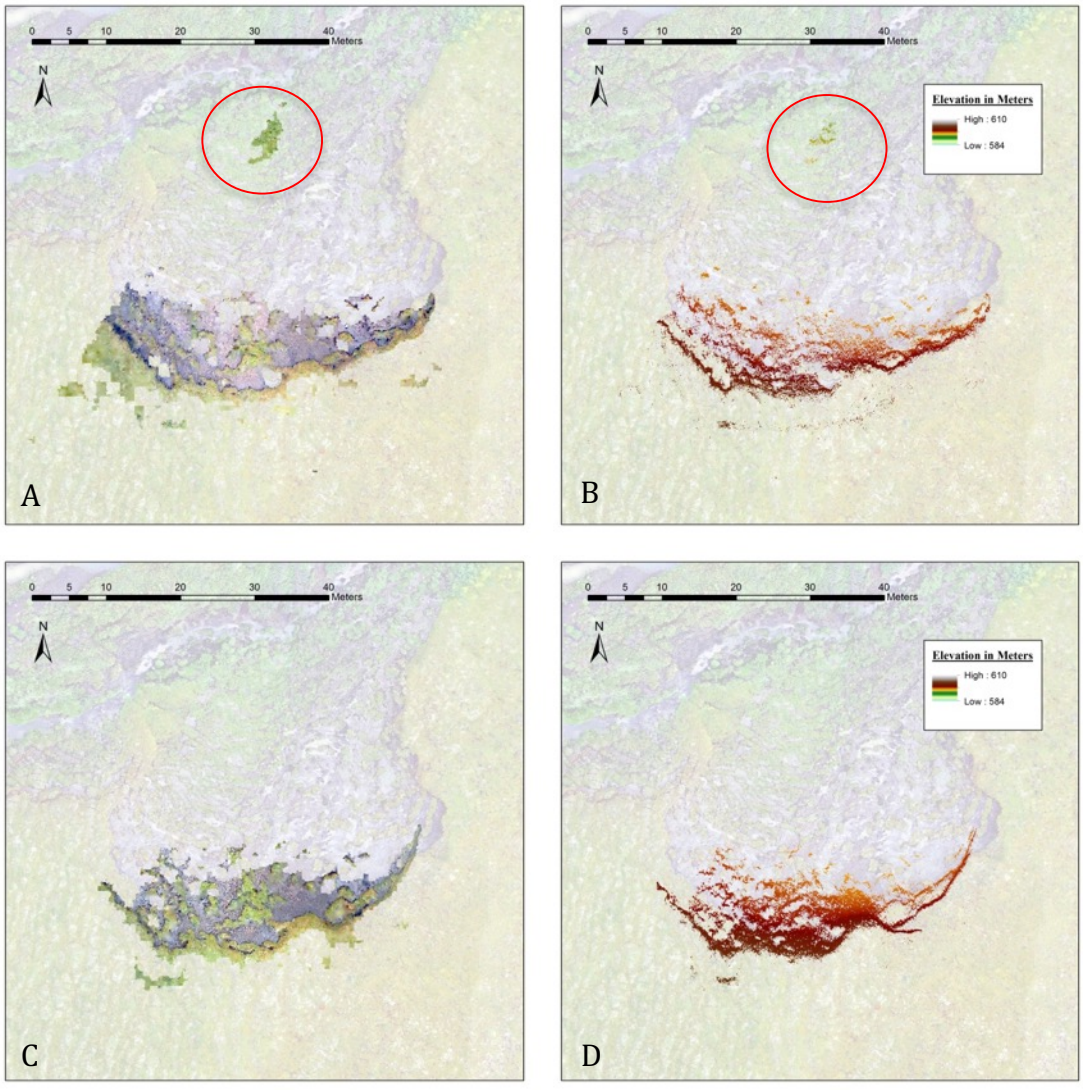

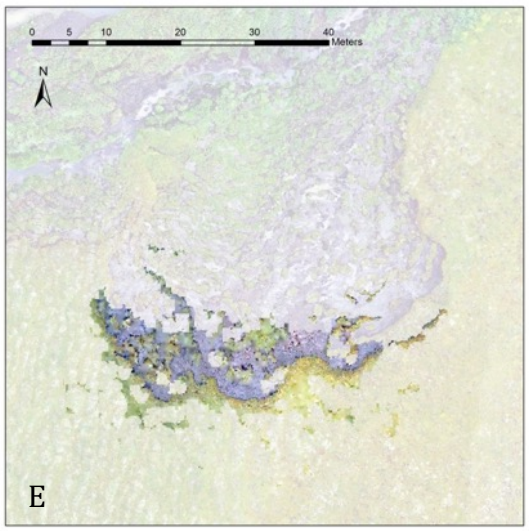
0 5 10 20 30 40
Meters
N
E

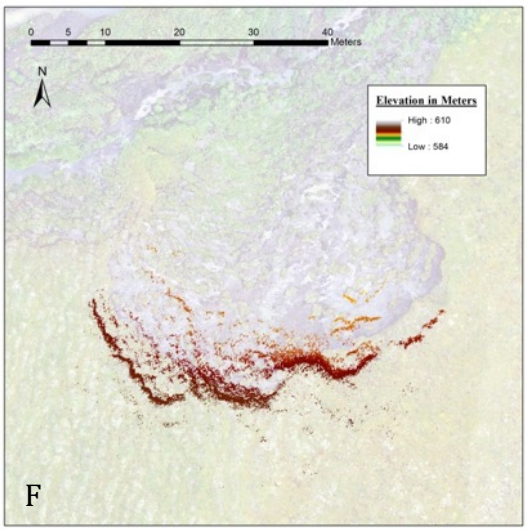
0 5 10 20 30 40
Meters
N
Elevation in Meters
High : 610
Low : 584
F

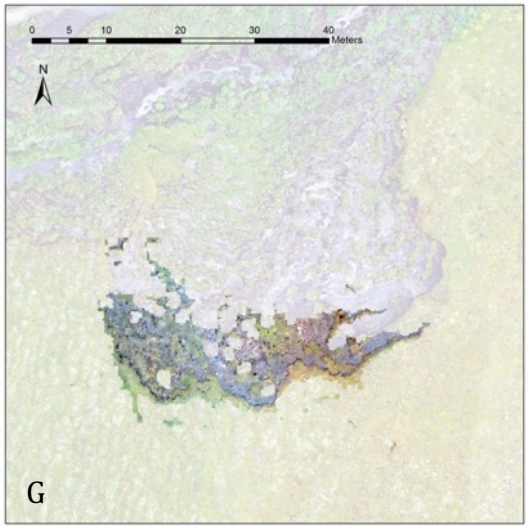
0 5 10 20 30 40
Meters
N
G

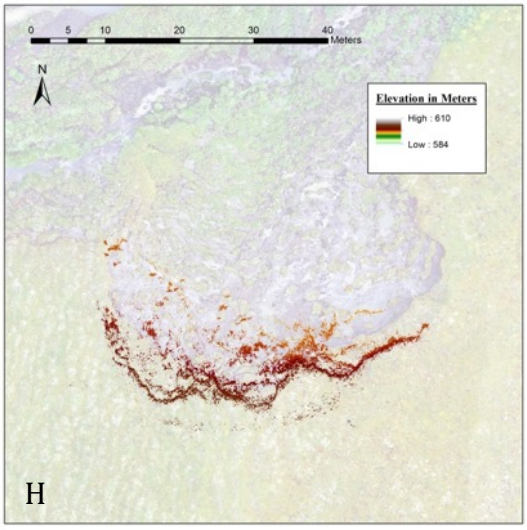
0 5 10 20 30 40
Meters
N
Elevation in Meters
High : 610
Low : 584
H

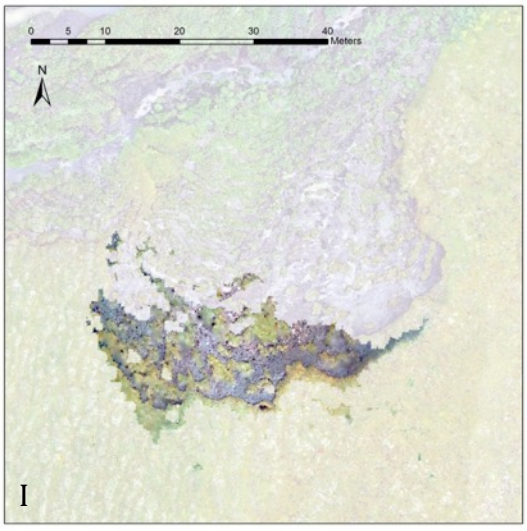
0 5 10 20 30 40
Meters
N
I

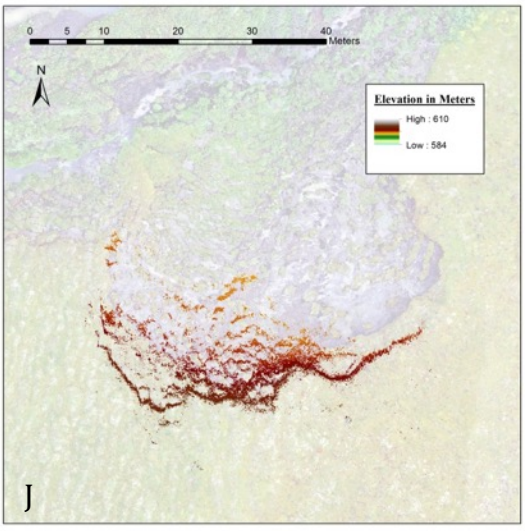
0 5 10 20 30 40
Meters
N
Elevation in Meters
High : 610
Low : 584
J

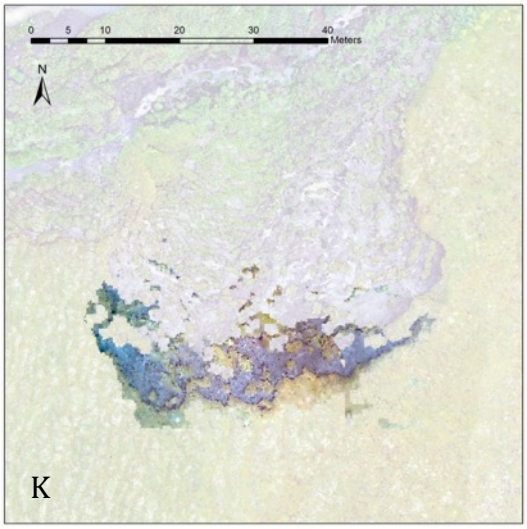
0 5 10 20 30 40
Meters
N
K

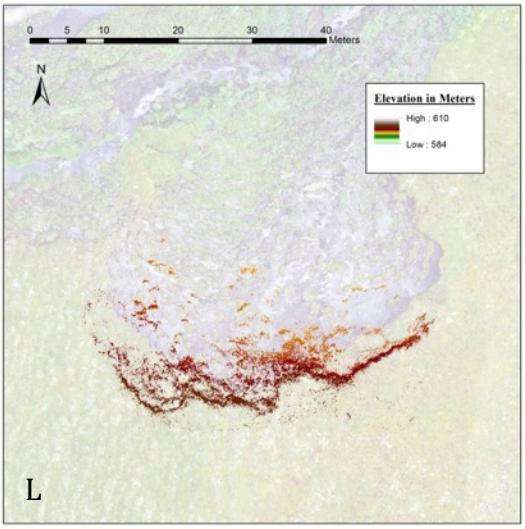
0 5 10 20 30 40
Meters
N
Elevation in Meters
High : 610
Low : 584
L

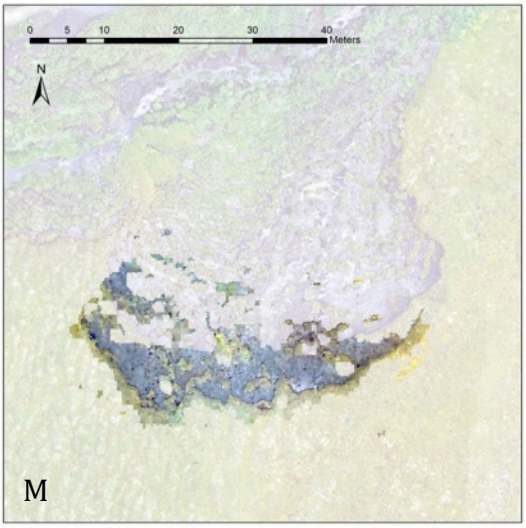
0 5 10 20 30 40
Meters
N
M

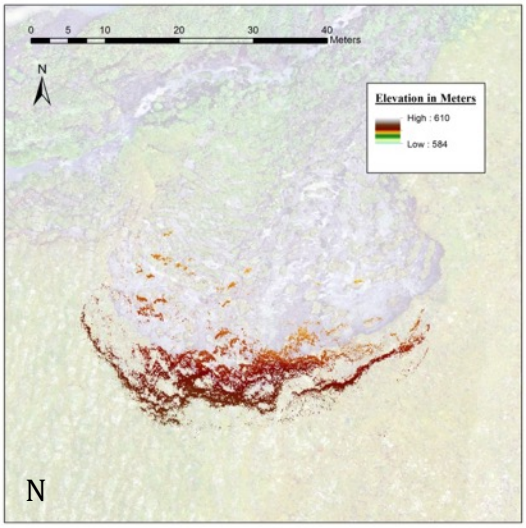
0 5 10 20 30 40
Meters
N
Elevation in Meters
High : 610
Low : 584
N

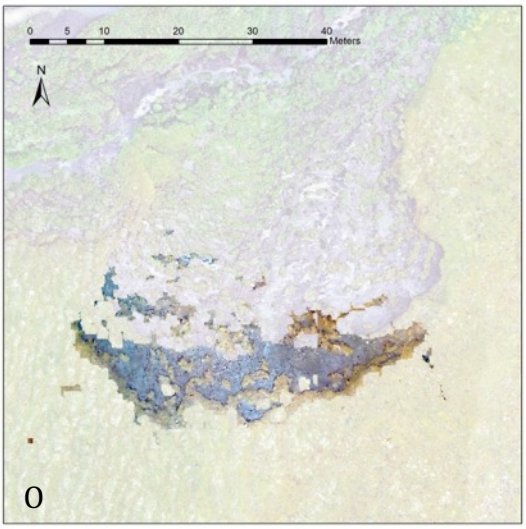
0 5 10 20 30 40
Meters
N
O

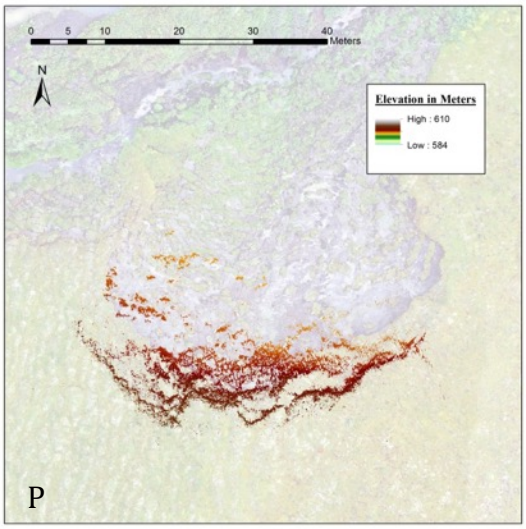
0 5 10 20 30 40
Meters
N
Elevation in Meters
High : 610
Low : 584
P

Figure 17. Orthophotos and DEM of D1 (raw results), derived from camera array. A) June 27 orthophoto. Modelled region distant from main model indicated in red as outlying data; B) June 27 DEM; C) July 7 orthophoto; D) July 7 DEM; E) July 17 orthophoto; F) July 17 DEM; G) July 25 orthophoto; H) July 25 DEM; I) August 1 orthophoto; J) August 1 DEM; K) August 14 orthophoto; L) August 14 DEM; M) August 20 orthophoto; N) August 20 DEM; O) September 2 orthophoto; P) September 2 DEM.

5.2.1 Quantifying changes in 2016

To investigate the ground-based SfM modelling results in two dimensions, a cross-section was created which traversed the slump from headwall to toe (Figure 18) where data points were collected from each epoch of data, including the 2015 and 2016 UAV reference data. Figure 19 shows only the UAV reference data cross-sections and indicates the change in morphology over one year along the cross section. The plotted data show interpreted headwall retreat, regions of sediment deposition and reorganization of material near the creek situated in a topographic low. In Figure 20a, the UAV reference data cross sections are plotted with the data from the interpolated dataset DEMs from the proposed method. The datasets appear smoothed below the headwall region as they represent interpolation in areas of sparse data, and should be dismissed as erroneous. In Figure 20b, a close-up of the headwall region is shown, allowing for closer inspection of the datasets. When compared to the UAV data cross sections, the captured data is much noisier, showing spiked surfaces. However, despite the lack of smooth surface, the captured data not only indicates the position of the headwall at each epoch, but also that the position of the headwall at each epoch agrees temporally as the headwall progressively retreats. The occurrence of each sequential position of the headwall coincided with the next available epoch of data, suggesting that although noisy, the data are representative of the approximate headwall position on that date.

The estimated rate of change in the headwall and volume loss in the headwall region between each datset is provided in Tables 5 and 6, respectively. In all cases, the headwall retreat rates were estimated by measuring the distance several times between the headwall extent on each date included in the epoch, taking the average distance and then divided by the length of the epoch. In the case of multi-year epochs, the length was adjusted to accommodate the lack of change occurring outside the active thaw season. The active thaw season was estimates as June 1 to September 30 of any year. The headwall retreat rates are therefore estimates as they created manually and were not measured along any one cross section. The calculated headwall retreat rates of the D1 slump using the epochs of data produced in this study are in the range of 10.6 to 26.4cm/day, with an average of 16.9cm. The headwall retreats derived from the eight epochs of 2016 ground-based SfM models are higher to those calculated from the 2015-16 UAV data and the 2012-16 LiDAR-UAV data, which yielded retreat rates of 4.1 and 3.6 cm/day, respectively. It's possible that these rates are slower as this estimate represents an average over a much longer time period. It's possible, when one considers the variation in the activity levels in each epoch of this study,

that the slump experienced widely varied retreat rates at different times during the slump's development. However, the estimated headwall retreat rates of the larger Charas and Melanie slumps from Digital Globe imagery measurements (Figure 3) are of the same order of magnitude as those derived from the eight epochs of 2016 ground-based SfM models. Again, it's possible that those slumps may have had high retreat rates over one year (of the several between compared epochs) and low rates over the other years. The lack of temporal resolution may be improved in the future with acquisition methods similar to that proposed in this study, and could help shed light on the complexities of RTS activity, perhaps even as they relate to other factors such as precipitation events or increased temperatures.

The rate of volume loss (m^3/day) was derived as the calculated volume lost (m^3) over the length of time represented by the DoD. For example, between June 27th and July 7th, 14.47m^3 were lost over 11 days, providing a rate of change of 1.32m^3/day. Over each of the epochs, an area of approximately 15-60m^2 was modelled and approximately 3 – 35m^3 of material was lost. It should be highlighted that the number of days represented by each DoD differed widely (3-14 days) due to inconsistent availability of appropriate imagery sets. Over the study period (June 27th – September 2nd, 2017) volume lost near the headwall was approximately 130m^3 over 74 days, resulting in an estimated rate of change of 1.75m^3/day.

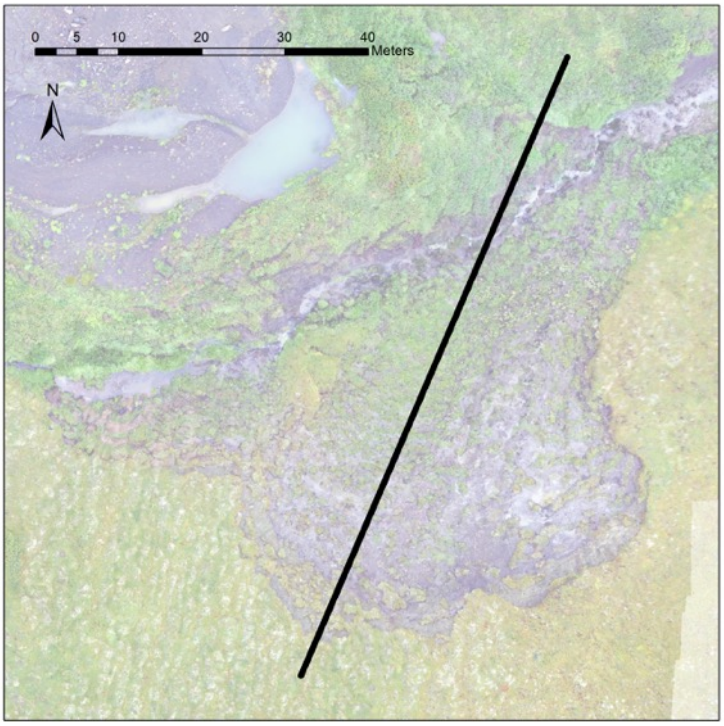

Figure 18. Location and orientation of cross-section at D1 used for comparison between UAV derived and epoch based DEMs.

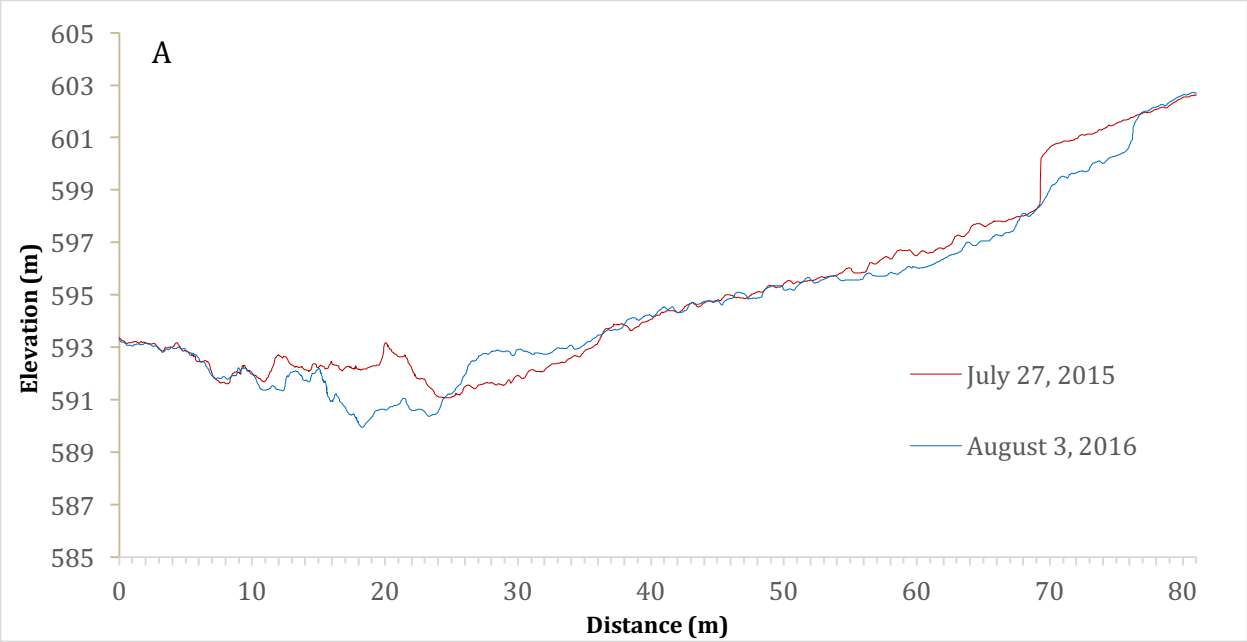

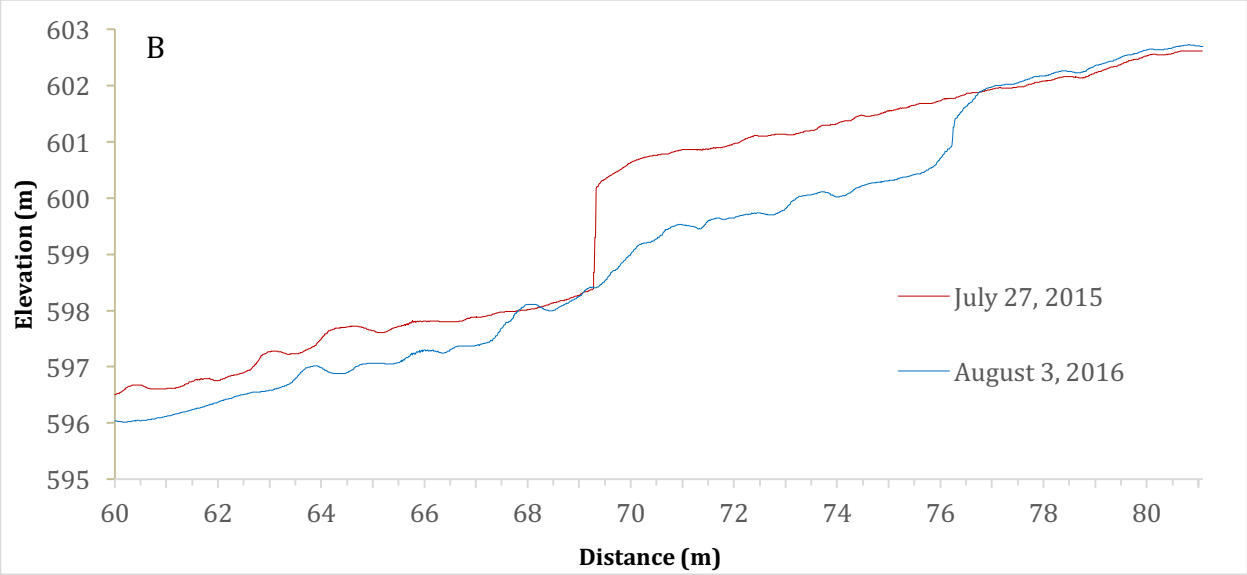

Figure 19. Cross section of UAV reference DEMs over one year (July 27, 2015 to August 3, 2016). A) Full cross section; B) Headwall region only.

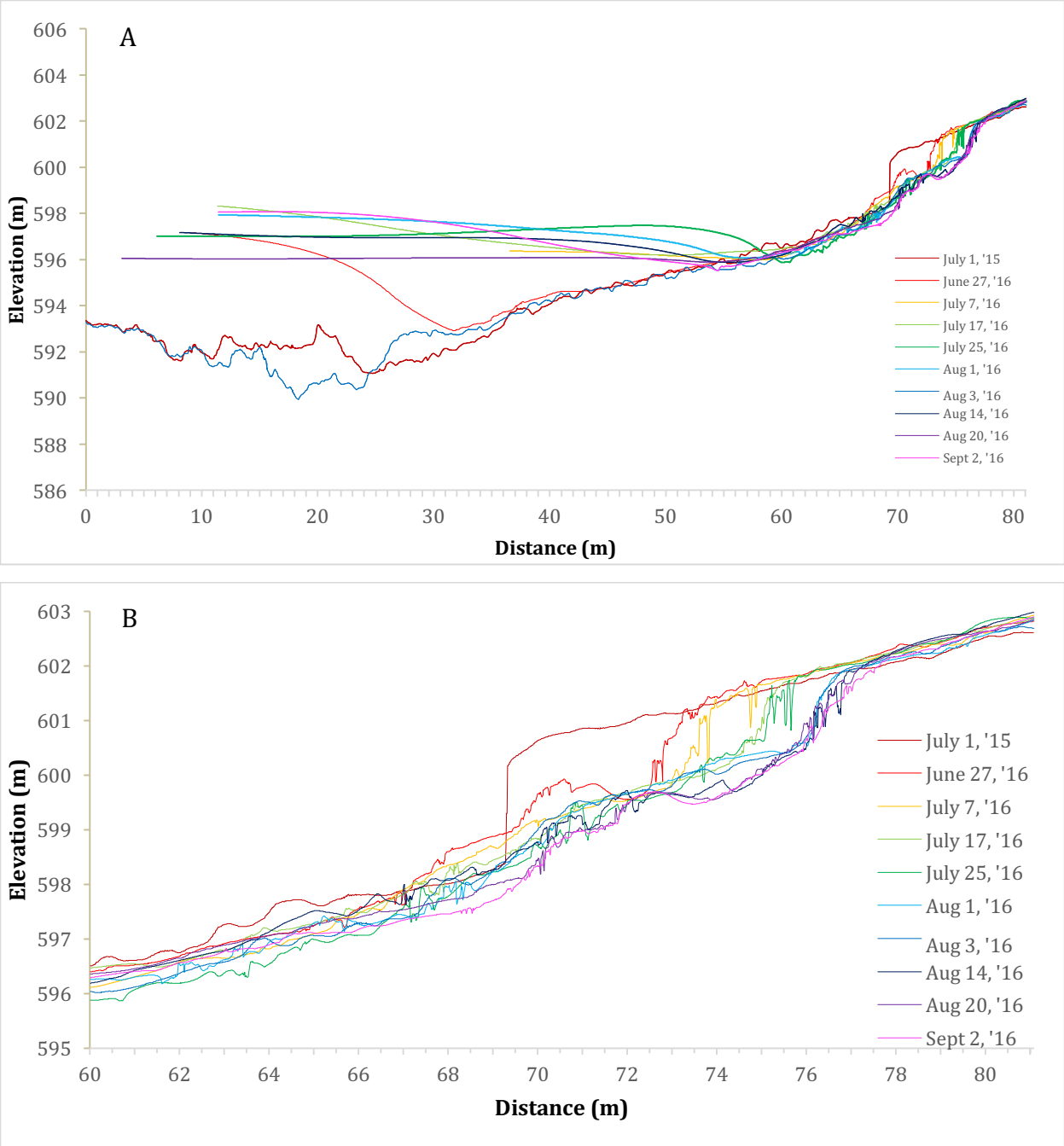

Figure 20. Cross Section of interpolated DEMs including both UAV reference models and models of this study's epochs. A) Full cross section; B) Headwall region only.

Table 5. Estimated headwall retreat of Peel Plateau retrogressive thaw slumps.

Slump/Epoch	Average Retreat (m)	Epoch Length	Est. Retreat Rate (cm/day)
Melanie (2000 – 2008)	120	976 days	12.3
Melanie (2008 – 2014)	52	732 days	7.1
Charas (2000 – 2008)	110	976 days	11.3
Charas (2008 – 2014)	90	732 days	12.2
D1: June 27-July 7	1.489	11 days	13.5
D1: July 7-July 17	1.439	10 days	14.4
D1: July 17-July 25	1.354	9 days	15.0
D1: July 25-August 1	1.245	8 days	15.6
D1: August 1 – August 3	0.675	3 days	22.5
D1: August 3 – August 14	1.275	12 days	10.6
D1: August 14 – August 20	1.848	7 days	26.4
D1: August 20 – September 2	2.355	14 days	16.82
D1: July 27, 2015 (UAV) – August 3, 2016 (UAV)	4.6	129 days	3.6
D1: 2012 (LiDAR) – August 3, 2016 (UAV)	20.1	488 days	4.1

*for multiyear epochs, length of epochs is calculated as June-September (approximate thaw season = 122 days) and multiplied over the number of years. Calculations for Melanie and Charas used Digital Globe imagery and LiDAR (GNWT, 2012).

Table 6. Calculated volume loss over time and associated rate of volume loss.

Epoch	Cell Size (m)	Cell Count	Area (m^2)	Sum of Cell Values	Volume Lost (m^3)	Length of Epoch	Rate of change (m^3/d)
June 27 – July 7	0.01	206,095	20.6095	144,672.3571	14.47	11 days	1.32
July 7 – July 17	0.01	589,951	58.9951	367,792.6624	36.78	10 days	3.68
July 17 – July 25	0.01	221,497	22.1497	99,944.08551	9.99	9 days	1.11
July 25 – August 1	0.01	299,997	29.9997	186,922.5637	18.69	8 days	2.34
August 1 – August 3	0.02	49,938	19.9752	6,812.318481	2.73	3 days	0.91
August 3 – August 14	0.02	39,813	15.9252	19,334.45795	7.73	12 days	0.64
August 14 – August 20	0.01	256,822	25.6822	133,158.9852	13.32	7 days	1.90
August 20 – September 2	0.01	521,915	52.1915	255,461.1671	25.55	14 days	1.83
June 27 – September 2	-	-	-	-	129.26	74 days	1.75*
Jul 27, 2015 – Aug 3, 2016	0.02	9,905,880	3,962.352	2,365,689.158	946.28	129 days	7.34

*Bounding dates of each epoch are counted twice as they are used in calculating length of epoch in more than one epoch (start date for one, end date for next). This causes additional error in the calculation of average rate of change. The average rate reported for the study period (June 27 – September 2) is the sum of volume lost over the study divided by the length of the study. Each row represents a DoD between two sequential epochs of data. The area of each DoD is reported based on the cell resolution of the DEM and the cell count. DoDs that employed the August 3rd UAV reference data were adjusted to account for the larger cell resolution of the UAV data.

5.3. Comparison of differencing methods: 2016 ground-based SfM versus 2016 UAV reference data

Four methods of change detection and deformation analysis were employed to investigate changes to the D1 slump. One was a two-dimensional approach applied by differencing DEMs to produce DEMs of difference (DoDs), and the other three are 3D cloud differencing methods (C2M-Delaunay, C2M-Poisson, M3C2). Here, we compare the changes in elevation of the slump derived from each method to evaluate if similar results are obtained. To allow comparison to the other cloud differencing methods, the dataset's un-interpolated DEMs were differenced against the August 3rd UAV data to create DoDs. Cloud differencing results have been resampled to a larger resolution (10cm) as the raw results are too fine resolution (0.01m) for visualization (Figures 25-32).

Table 7 shows the minimum, maximum, range, median and mean of elevation change for each of the four differencing methods investigated relative to the August 3rd UAV reference data. The data range in each epoch, over the various differencing methods, vary from 2.087m to 6.674m, with minimums (negative change interpreted as erosion) ranging from -0.626m to -3.317m and maximums (positive change interpreted as deposition) ranging between 1.099m and 3.357m. The data means for each epoch and differencing methods varied between -0.020m and 0.588m. The same data is represented in Figure 21 as boxplots, each of which contains all eight epochs of data as compared to the August 3rd UAV data. Each differencing method's boxplot has 8 boxes, one for each date, and all show a slight negative trend, which can be interpreted as increasing (positive and negative) magnitude change with distance from the central UAV reference date. In each plot, the August 1st epoch falls near the zero line, as little change was detected over the 3 days since the UAV survey on August 3rd. By contrast, on June 27th, we see the largest deviation from zero (August 3rd UAV reference) as there was much more material (positive mean) present at D1 slump on that date. Similarly, on September 2nd, there was much less material (negative mean value) compared to August 3rd UAV reference. This temporal trend was observed in all four differencing methods investigated (Figure 21). Major differences exist in the data's whiskers for each date, between methods. These values are presented in Table 7, and were presented above as widely ranging data sets. Figure 22 focuses on the data means, not the disparate data ranges. Here we see that the data for each differencing method plotted, allowing comparison of the trend over time. All methods produced negative slopes. The DoD results had the steepest slope, suggesting that that differencing method reported the largest change when compared to the UAV reference data. The M3C2 results show the shallowest slope, suggesting that that differencing method reported the smallest change when compared to the reference UAV data. The two C2M differencing results fall between the DoD and M3C2 results. It should be noted that all four differencing methods estimate change on August 1st as very close to zero when compared to

the August 3rd UAV reference data, suggesting that the proposed data acquisition method can detect small scale change.

Figure 23 shows the spatially mapped results from all four differencing methods, for the June 27th epoch. The results for all eight epochs are found in Appendix A, Figures 25-32. As an example, the DoD map for June 27th (Figure 23a) shows a reduced extent compared to the other differencing method maps, as the un-interpolated DEMs were employed. The DoD map has darker colours, suggesting increased magnitude in the data extremes. Surfaces (meshes, average surface) estimated based on the input point clouds were employed in the other differencing methods (Figure 23 b-d) producing similar areal extents that do not match that of the DoD map. The two C2M maps for June 27th (Figure 23 b-c) appear similar, apart from processing artifacts in the C2M Delaunay map (Figure 23c), which commonly occur when Delaunay triangulation is used on non-planar surfaces. The artifacts occur along the far west and east side of the headwall, where vertical change is high. Similar artifacts appear on the M3C2 map (Figure 23d) of the June 27th epoch, and also appear on the C2M – Delaunay and M3C2 maps of other epoch data (Appendix A).

Figure 24 demonstrates the mapped extremes in the resulting June 27th data for each differencing method, as calculated by isolating the top and bottom 10% of the dataset. The major differences in the maps are the same as in the full data maps. The DoD map (Figure 24a) has darker colours, and therefore larger magnitude extremes, C2M-Delaunay and M3C2 show artifacts in areas of high vertical change, and the three differencing methods employing surfaces (C2M –D, C2M-P, and M3C2) have data upslope of the headwall that does not occur in the DoD map. However, aside from these differences, the spatial occurrence of the data extremes appears to occur in the same locations, regardless of disparity in their values (different reported data ranges). This spatial agreement suggests that although unable to produce results of the same magnitude between differencing methods, the proposed acquisition method is detecting the greatest magnitude change in the locations one would expect given RTS behaviour and visual inspection of the input imagery.

Table 7. Elevation differencing results of epoch data at D1, relative to UAV reference Aug 3, 2016 (in meters).

Epoch Date	Minimum	Maximum	Range	Median	Mean
June 27					
DoD	-1.819	2.183	4.002	0.498	0.588
C2M-D	-1.767	1.873	3.640	0.321	0.359
C2M-P	-0.815	1.916	2.731	0.365	0.432
M3C2	-3.317	3.357	6.674	0.199	0.290
July 7					
DoD	-2.866	2.421	5.287	0.377	0.468
C2M-D	-1.766	2.265	4.031	0.254	0.292
C2M-P	-0.912	2.293	3.205	0.293	0.351
M3C2	-2.500	2.550	5.050	0.130	0.270
July 17					
DoD	-0.920	2.072	2.992	0.274	0.402
C2M-D	-1.593	1.692	3.285	0.164	0.201
C2M-P	-0.767	1.726	2.493	0.195	0.257
M3C2	-2.237	2.538	4.775	0.157	0.214
July 25					
DoD	-2.164	1.989	4.153	0.190	0.248
C2M-D	-1.360	1.676	3.036	0.079	0.093
C2M-P	-1.444	1.712	3.156	0.104	0.122
M3C2	-2.832	2.490	5.322	0.101	0.131
August 1					
DoD	-1.615	1.583	3.198	0.068	0.066
C2M-D	-1.535	2.025	3.560	0.055	0.050
C2M-P	-1.570	2.120	3.690	0.063	0.059
M3C2	-0.626	1.461	2.087	0.061	0.068
August 14					
DoD	-2.508	2.171	4.679	-0.112	-0.115
C2M-D	-1.831	1.634	3.465	-0.060	-0.063
C2M-P	-1.884	1.364	3.248	-0.078	-0.084
M3C2	-0.879	1.345	2.224	0.066	0.085
August 20					
DoD	-1.984	2.471	4.455	-0.182	-0.241
C2M-D	-1.531	1.395	2.926	-0.122	-0.152
C2M-P	-1.587	1.211	2.798	-0.146	-0.181
M3C2	-1.448	1.235	2.683	0.025	-0.020
September 2					
DoD	-2.362	1.950	4.312	-0.298	-0.349
C2M-D	-2.354	3.535	5.889	-0.206	-0.226
C2M-P	-1.836	2.214	4.050	-0.242	-0.267
M3C2	-1.921	1.099	3.020	0.029	-0.062

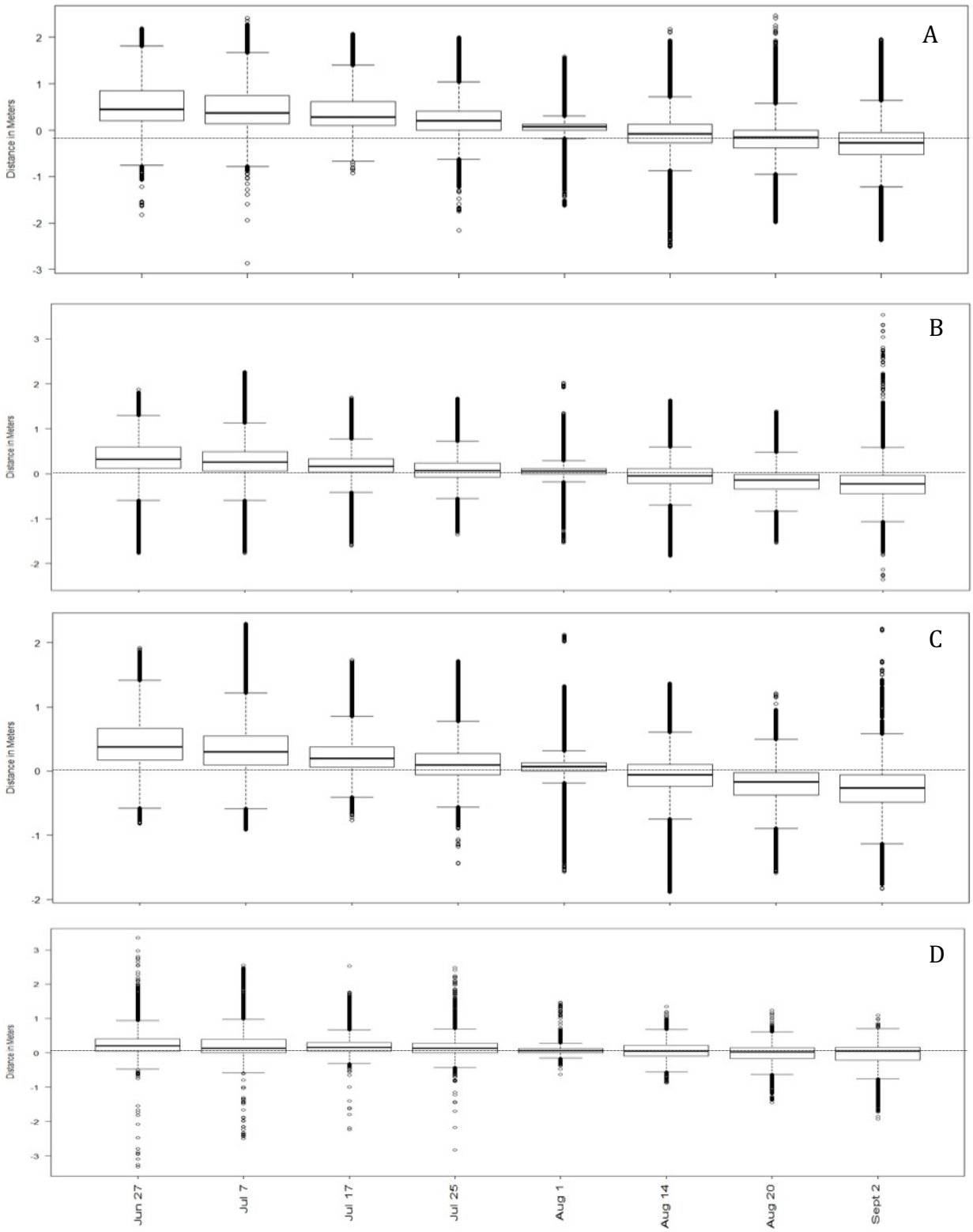

Figure 21. A) Box plot of each modelled epoch compared to the August 3, 2016 UAV reference model. A) DoD; B**)** cloud to mesh (C2M – Delaunay) distances; C) cloud to mesh (C2M - Poisson) distances; D) multiscale model to model cloud comparison (M3C2) to mesh distances.

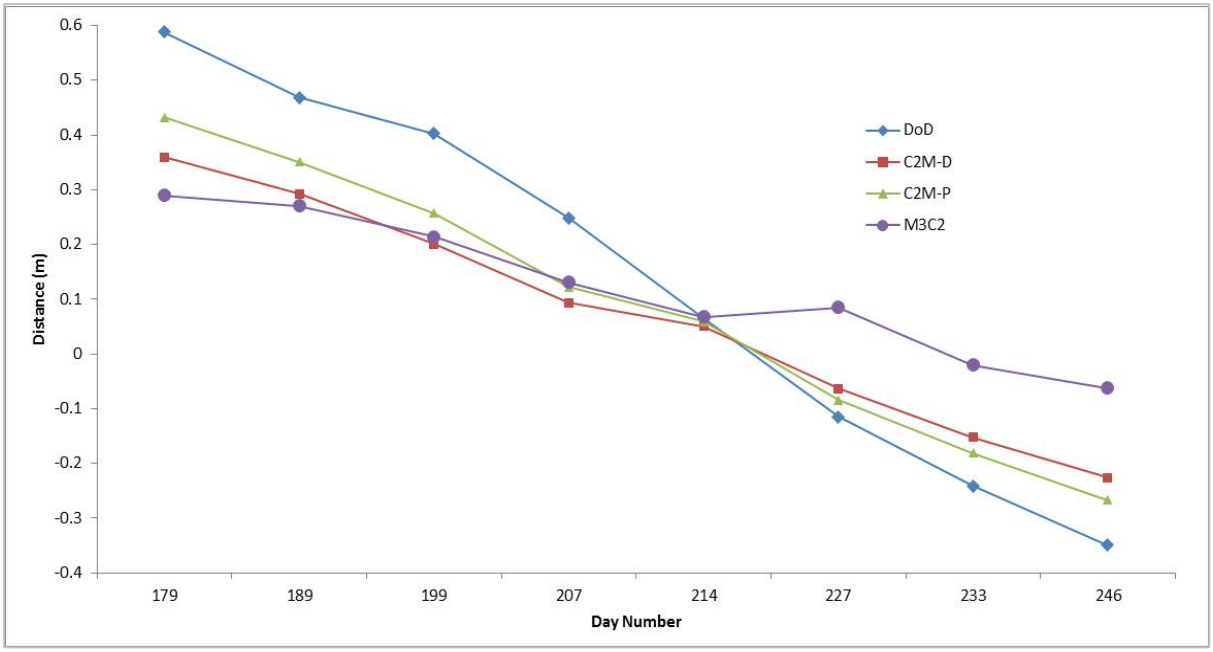

Figure 22. Plot of mean epoch elevation change over time, relative to August 3, 2016 UAV reference, via four differencing methods.

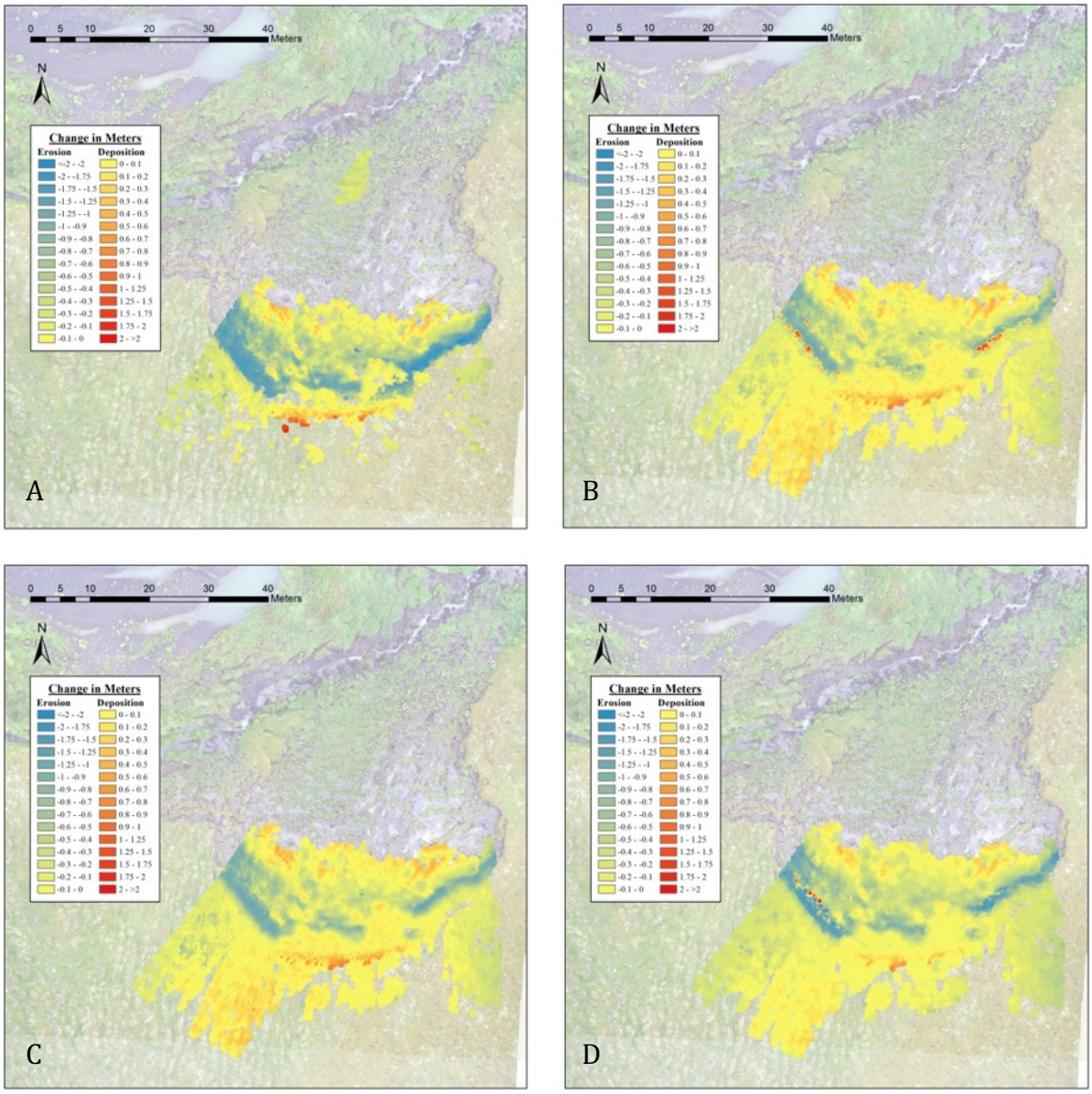

Figure 23. Elevation change results of SfM models at D1 (relative to August 3, 2016 UAV reference model) derived from camera array on June 27, 2017. A) DEMs of Difference (DoDs); B) Cloud to Mesh (C2M) distances (via Delaunay triangulation mesh; C) Cloud to Mesh (C2M) distances (via Poisson mesh); D) Multiscale Model to Model Cloud Comparison (M3C2) distances.

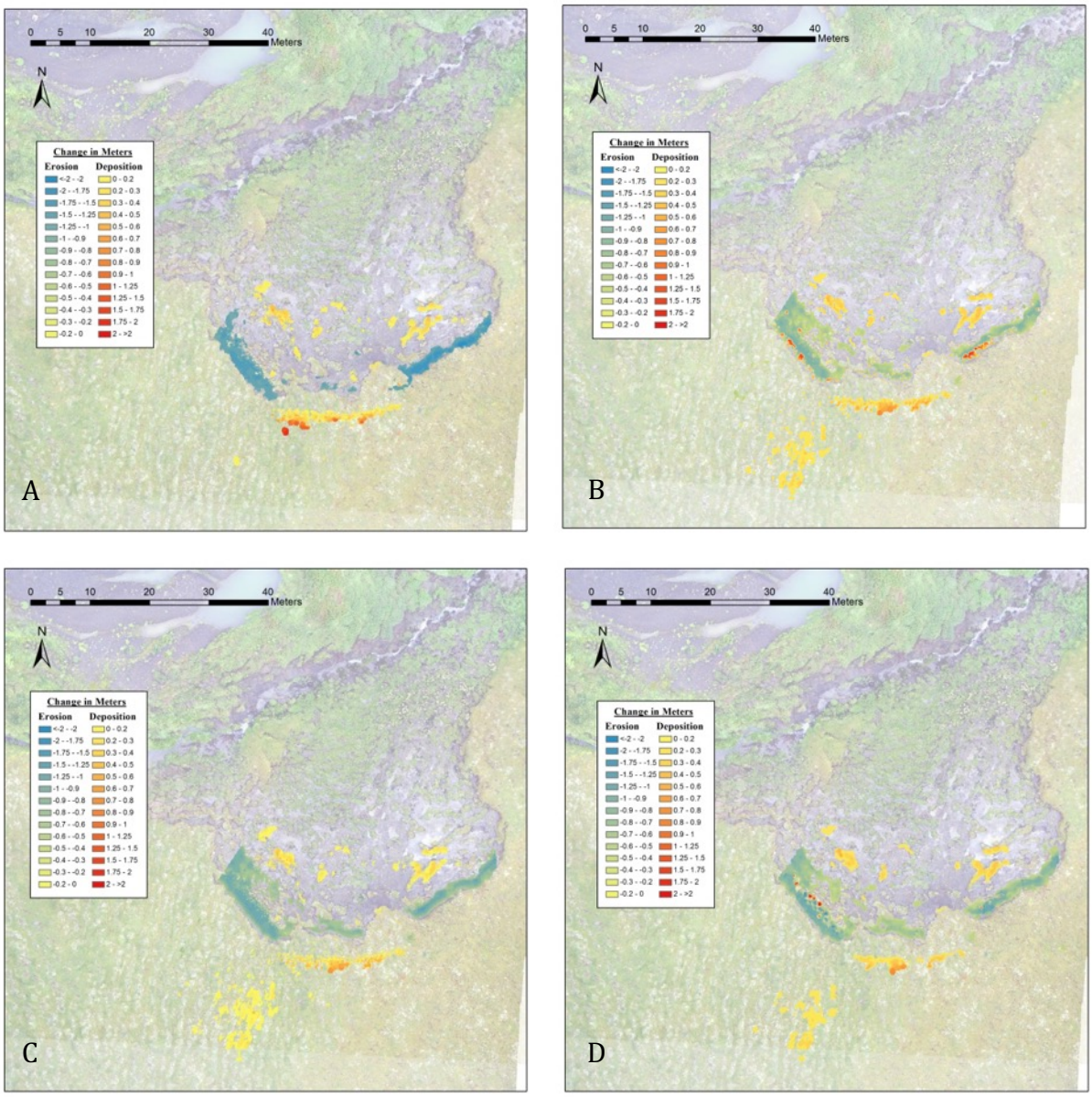

Figure 24. Elevation change results of SfM models at D1 (relative to August 3, 2016 UAV reference model) derived from camera array on June 27, 2017. Data has been reduced to the extreme values falling under and over the 10% and 90% quantiles, respectively. A) DEMs of Difference (DoDs); B) Cloud to Mesh (C2M) distances (via Delaunay triangulation mesh; C) Cloud to Mesh (C2M) distances (via Poisson mesh); D) Multiscale Model to Model Cloud Comparison (M3C2) distances.

6 Discussion

6.1 Complications associated with trail cameras

This thesis was a proof of concept study on the use of trail cameras to generate ground based SfM models. Many of the complications associated with this study are related to the cameras employed, some of which were anticipated and some of which were not. One unanticipated issue was the compression of the images produced (Figure 42), which acts to impede the performance of the feature matching algorithms, as it employs similarity between groups of pixels in different images. Unlike most cameras used in Structure from Motion for mapping applications, there are no .RAW format images available from the chosen cameras. Furthermore, the .JPG files produced by the trail cameras are aggressively compressed. For comparison, photos from DJI's Phantom 3, which has the same 12-megapixel resolution as the chosen camera, are approximately 5MB is size. The .JPG images used in this study have been compressed to approximately 1MB, a comparative reduction in quality of 80%. This means that despite an appropriate sensor size and resolution, the loss of fine detail causes unnecessary difficulty for the SIFT matching algorithm, on which subsequent results rely.

To further highlight the detriment of the camera's file compression, it should be noted that an IPhone 5, with an 8mega pixel camera, was used to check camera field of view overlap in the field during installation. The images were used to produce test models in Agisoft Photoscan which would confirm proper camera alignment, and were not intended for use in the study. Despite the lower resolution (8mega pixel versus 12mega pixel), the average image size produced by the IPhone was 4MB (compared to ~10MB from the Canon SLR camera used in the trial and ~1MB from the cameras used in the study), and were able to produce models without the addition of position information, nor processing manipulation.

One of the twelve cameras critically failed after only three days due to outdated firmware upon purchase, according to SpyPoint's customer service. Fortunately, this camera was the second in the array, falling in the area of 100% overlap, meaning its loss was less detrimental than had this individual unit been positioned in the lower overlapping portion of the array (cameras 6 - 12).

Additionally, four of the remaining eleven cameras experienced errors in data logging at various points over the season which caused the internal clock to be set back to previous dates in the study period, leading to mis-assignment of date and time to frames after that point. Another issue that caused considerable challenge to the project was the internal clocks of the cameras. The cameras were set to the time-lapse capture mode on a one hour interval. However, in organizing the subsequent photos into groups by shot time, it was found that the one hour capture setting was not exact. In most cases the cameras shot every 58 minutes, and in several cases, the interval changed within individual cameras. Capture occurred anywhere from every 56-103 minutes, often changing in interval over time. Over the

study period of two and a half months, this compounding change in capture interval lead to photo capture at a wide variance of times. In most cases, photos within one time epoch vary in capture time by up to +/- one hour. This misalignment of capture timing meant that although the volume of captured data was large (approximately 20k frames total), it was not as robust a data source as anticipated.

Some of the best lighting conditions occurred in early morning, when sun intensity was low. This window of ideal lighting was quite short, usually lasting less than one hour. Unfortunately, due to the capture timing offset previously discussed, full 11 photo sets were not often found within the one hour time frame. Additionally, the cameras used also employ infrared light during night hours. However, again, the timing of the switch between infrared and regular optical lens was inconsistent between cameras. This meant that even when ideal shots were captured in regular daylight early in the morning, other cameras remained on infrared mode, only changing to regular optical mode on the next hour (~58 minute) interval after the ideal morning light had dissipated (Figure 10).

Additional factors that reduced the volume of ideal 11 photo data sets were wide. As in any other SfM survey, overcast conditions are considered ideal as shadow casting and reflection of light is minimal. Periods of extended rainfall could not be used due to wet and therefore reflective surfaces, as well as fog and condensation on the camera lenses, which obscure the photos. Often good lighting conditions appear immediately after rain events as the overcast skies do not cast shadow on the complex topography of the slump floor. However, in these cases, one or more or the 11 cameras would have water droplets on the lens, which also exclude the set from use in modelling. Finally, and most substantially, slump movement was an issue in data selection. The slump movement was not constant, varying widely in rate over time. There were periods of several days in which no movement occurred, as well as periods of several days where extensive geomorphic reworking took place. Again, because of the timing offset in capture, no data from these periods of movement could be used as the difference in morphology over periods of even only several minutes, removed photo sets offset by no less than 30 minutes from candidacy. The difference in morphology of the slump between shots during these times would not allow reconstruction of models as they cannot model areas which moved or changed in shape. This large suite of limitations in condition reduced the workable data down to 8 datasets (88 photos or 0.3% of the collected data). The utility of trail cameras for monitoring sciences should not be undervalued, and have proven increasingly advantageous in a variety of studies (Rovero *et al.*, 2013).

6.2 Complications associated with geometry of camera alignment

A total of twelve cameras were set in an array facing the thaw slump target. The array was separated into two groups based on available installation positions. The first 5 cameras were set further

away from the slump to allow each to capture the entire target feature in frame, providing close to 100% overlap. The remaining six cameras were set closer to the slump on a small topographic high, which provided the array variation in height and obliquity. The coverage attained by these cameras focused on overlapping sections (approximately 70%) of the slump floor and provided more (closer, therefore higher resolution) detail to the survey.

Cameras six and seven, in the center of the array, were somewhat focused in field of view toward an area of the slump floor which was the most active in the previous thaw season, as seen in reconnaissance data collected from one Reconyx camera, courtesy of Steve Kokelj (GNWT). The assumption that this area would again be the most active, and therefore worthy of focus, proved a poor choice as this area subsequently experienced very little movement in 2016. Additionally, the stabilization of this erroneously chosen area of interest led to development of a large amount of tall vegetation coverage, which further reduced the employability of these photos, as they consisted of mostly tall vegetation, which SfM algorithms have difficulty rectifying. These two cameras therefore were least likely to be included in model reconstruction, leaving the far left of the slump unmodeled and a consistent separation of the array by the software into two groups.

Camera movement over the study period was minimal, as determined by visual inspection of difference in field of view over time. Camera 6's alignment shifted more than any other camera, however this shift only began late in the study period. The movement was more notably a change in orientation, rather than in 3D location, which would have negative effects on field of view overlap, not camera positioning. Both location and orientation of cameras are calculated in reconstruction, therefore this information is not required as an input. Camera position was recorded, but orientation was not. Therefore, this movement is not a deviation from the camera position data recorded, but in field of view overlap.

It remains to be determined why the high-resolution camera positions caused large increase in error estimates during modelling attempts. It's possible that when anchored to the pseudo GCPs, which were upslope of the feature on un-deformed terrain, the SfM algorithms could not rectify the estimated camera positions with the provided coordinates. This is less likely to be the only influencing factor, as the pseudo GCPs were only included after the failure of the camera coordinates. Although successfully included, the pseudo GCPs that were used in lieu of the camera coordinates were relatively linearly aligned, which is not recommended for proper triangulation. It's then possible that the success of the modelling in areas proximal to the headwall, and pseudo GCPs, could be due to their spatial position in the data. Additionally, given their position, it could be argued that the areas not well modelled (down slope of the headwall, near camera positions) are, as one might expect, those distal to the anchoring points. Also, areas distal from anchoring points, especially those with poor triangulation, are the most

susceptible to poor registration. However, the GCPs were positioned outside the area of deformation, on stable ground above the headwall. Although susceptible to creep by gravity, this area was likely the least likely to endure positional change over the study period as the permafrost remained insulated under the active layer.

6.3 Comparison of the proposed acquisition method's modeling results against RTS behaviour

Appendix A contains maps for visualization of this study's results spatially which allows not only investigation of the performance of the various differencing methods employed, but also for indication of the success of the study's proposed capture method. The trends presented in the data tables and boxplots support the proposed method in terms of empirically supporting the temporal behaviour we would expect, and examination of the maps allow better insight into to the validity of the data in terms of its position. Based on understanding of retrogressive thaw slump behaviour, one would expect to see erosion at the headwall, and deposition of material within the slump scar. This is indeed what we see in the mapped results, over all the epochs in the study period. The dominant signal indicated low magnitude change (yellow), with smaller spatially agreeable regions of blue and red (interpreted as erosion and deposition respectively). Additionally, the pattern of high magnitude change (positive and negative) seems to inflate temporally as one would expect. Because the reference UAV data acquisition date falls close to the center of the chosen epochs, those epochs most temporally distal from this central reference date tend to show higher magnitude data extremes when compared to those dates closer to the reference acquisition date. For example, when the August 1st epoch is considered, we see little data falling in the extreme magnitude values (red or blue) and see that the data is generally yellow, indicating low magnitude change. This is what one would expect considering there was only two days between that epoch and the UAV reference data acquisition. Contrarily, the map show that the change detected on epochs with larger temporal offset, relative to the UAV reference date, contain portions of large magnitude change (positive and negative) as more time, and therefore deformation, has occurred over this period. This is highlighted in Figures 34-41 in Appendix A where only the highest and lowest 10% of data are represented. For August 1st (Figure 38), the extreme 10% of the data are of much lower magnitude than the more temporally distal epochs, with the maps showing shades of yellow. On September 2nd (Figure 41) for example, the extreme 10% of the data have little yellow, indicating the magnitude of change on that epoch was much larger due to the temporal offset. This high magnitude change is also positioned intuitively indicating the largest change happened along the headwall. The headwall erosion (blue interpreted as erosion) width also seems to agree temporally in magnitude, such that wider bands occur on epochs with larger temporal offset, and

thinner bands occur on epochs with shorter temporal offset as less retreat occurred over that time, relative to the UAV reference date.

Due to the inconsistency in data range between dates and differencing methods, the maps symbolized the extremes as one colour representing change beyond +/- 2m, masking increase in magnitude beyond +/-2m as one colour (red and blue respectively). If we investigate the data ranges of the M3C2 results in Table 7 for example, we see that there is a slight trend in the size of the range over time. The range is largest on dates distal to the UAV reference, and smaller when close to that date. The major outlier to this trend is July 25th, where the range indicates higher magnitude change than that of July 7th, a date much further temporally from August 1st. The minimum value recoded in the M3C2 results on July 25th was -2.832m, which is much larger than the minimum value recorded on the same date by the other differencing methods. This suggests such a large extreme may be considered error in this case. This example highlights again, the lack of congruency in data range between differencing methods, suggesting they lack precision. Without further analysis, it's difficult to say which of the methods should be considered the most precise. Investigation of the spatial occurrence of this particular extreme value may provide insight as to its validity in terms of signal or error. If the data point occurred isolated instead of among a gradient of spatially congruent high magnitude change, it may be considered error and could be culled. This is only one example from this study's results that exemplify the type of intricacies involved not only in interpretation of elevation change detection in natural environments, but also in isolating signal from error in such an analysis. Improved data grooming and classification by manual or empirical means may clarify these confusions in the future.

Although obvious differences between the differencing methods for each epoch are present, the spatial pattern of the data in each epoch seems to adjust in an intuitive way over the epoch iterations, which supplies confidence in the proposed capture method during its first attempt. Figure 22 also provides support to the method's feasibility early in development, as all the data sets, regardless of differencing method used, show some agreement in trend of data means over time.

6.4 Retreat rate and volume loss along headwall

Figure 19 shows cross sections from the two UAV derived DEMs plotted together. The data sets were collected a little over one year apart. Figure 19a shows the entire data set from head wall (70-80m distance) to the slump toe (0-20m distance). In this figure, we can see as one would expect that the headwall extent has retreated approximately 5 meters over that time period. We can also see good overlap in both epochs above the headwall, suggesting the two models are well registered, as this area would not be expected to have deformed to any great extent. On close inspection, the distance between the lines

above the headwall is approximately 5-8cm (Figure 19b). It is possible that this distance represents registration error, although minimal, or it may also be possible that the material above the headwall has risen slightly over time as the active layer slid downslope toward the edge of the headwall. It has also been suggested that subtle movements in permafrost terrain elevation may be attributed to seasonal elevational pulsing due to the volume difference between liquid and solid water as the active layer freezes and thaws. Although as these data sets were captured at a similar point in the thaw season, one could argue that the one month offset in the acquisition could be enough of a temporal offset to have small elevational differences due to phase change in water. This assertion should be taken into consideration when contemplating if this offset should be considered signal (true deformation) or error (registration).

At the left of Figure 19a, the slump toe is clearly indicated where the lines deviate around 20m. The red peak is interpreted as a deposition of material from the previous year which has since been further displaced down slope. The blue peak just upslope, around 30 meters, can be interpreted as a similar deposition of material from this study period, the thaw season of summer 2016. This material could have previously been the material now vacated from the headwall since the beginning of the thaw season. It is also possible that the chosen cross section does not pass through the interpreted area of highest deposition in both, or either year. Visual inspection of imagery from both years suggests that the area of highest flow rate is not spatially co-incident between years. It is then possible to interpret the gap in alignment at the toe region between the two data sets as the river bed. The river running across the slump toe, somewhat parallel to the headwall, is thought to be associated with the occurrence of the slump itself, as the presence of running water can contribute to thermal erosion of permafrost terrains, especially should the terrain be sloped. The flow rate in the stream can be seen in the imagery to be highly variable, having 'flashy' tendency, especially after precipitation events. This activity seems to be also eroding the south shore of the stream, beyond the existing slump. Material can be seen in the captured imagery detaching and falling into the stream within the first few days the installation was collecting data.

In Figure 20, the quality of the UAV derived data becomes further evident as the epoch data from this study appears smoothed toward the toe (left) and much noisier toward the headwall (right). In Figure 20a, the epoch cross sections follow a cubed root function shape toward the slump toe that deviates heavily from the UAV data, and among themselves. This area should be interpreted as artifact, as the DEM data extracted for these cross sections was that of the interpolated DEM outputs. This data was used as the modelling output DEMs were highly discontinuous, and did not model the slump much below the headwall. Closer attention should be focussed toward Figure 20b which is a closer look at the headwall area. Here we can see that the indicated headwall retreat agrees with the sequence in date for each dataset, suggesting that the modelled data was able to correctly capture the upslope retreat direction. Furthermore,

when the headwall positions between modelled datasets are inspected, it would seem that the approximate retreat rates shown agree with calculated volume loss. The calculations in Table 6 show that the volume lost was highest in the epoch between July 7 and July 17, and that between July 25 and August 1. This agrees with Figure 20b, where the greatest distance between headwalls fall on the same epochs, between orange and light green, and dark green and light blue.

Table 6 contains the estimates of volume lost from the slump headwall and estimated rate of loss during each epoch. As the length of each epoch was dictated by availability of appropriate data across the entire camera array, the volume lost in each is widely varied between approximately 2 and 36 cubic meters. However, when we look at the variability in the rate of volume loss, it can be seen that the deformation rate is not constant, as is the current understanding of thaw slumps in the literature. Some epochs saw very little change (60-90cm^3/day), and others experienced change rates comparable to the sum of the rest of the season (>3.5m^3/day). It has been suggested that external factors, namely precipitation events may have strong influence on the deformation rate in thaw slumps. Although the timing of high flow events was visually correlated with precipitation events in the captured imagery, empirical data from the nearby weather station at Fort McPherson will not be available until the fall of 2017, meaning support of the assertion will be delayed. Volume loss and rate of loss between the UAV reference data captured in the summer of 2015 and 2016 was also calculated. The volume loss over the year (active thaw season interpreted as June-September; 129 days) was estimated as just under 950m^3 which contributed to an estimated average retreat rate of 7.34m^3/day. This estimated daily rate of volume loss is higher than that of the proposed method (1.75m^3/day over 72 days). Contrarily, the estimated average headwall retreat rate of the epochs of data from this study was much higher than that calculated over the year of UAV data, at 16.9cm/day and 3.6cm/day respectively. These disparities could be due to the difference in time over which the rates were estimated, the difference in method by which they were calculated, differences in timing of slump headwall retreat and volume loss, or a combination of these and other factors. It's possible that the majority of RTS activity may be occurring over short time periods, or specific time periods which are being included in the estimate with periods of lower activity (early spring and late fall), leading to decreased rate estimates in longer epochs. The headwall retreat rates could be higher in this study's data because the time of this study focussed on the most active part of the thaw season. Similarly, the rate of volume loss could be lower for the epochs of this study as volume was only calculated in the headwall region specifically (as that was the only region able to be modeled), whereas the volume loss rate associated with the UAV data was calculated over the entire slump area. Further normalization of the data could provide further insight.

6.5 Comparison of change detection methods: DoD, C2M, M3C2

Quantification of the similarity in spatial distribution of the change signal in the epoch data may improve understanding of the proposed method, whereas the differences in the spatial distribution of signal would provide insight into the performance of the various differencing methods, and could help inform those interested in quantifying change accurately. Because the change detection analysis with the UAV derived data represents change over a year and over the full slump area rather than just the headwall, we cannot directly compare to the results produced by the proposed method. However, it can be employed in qualitative discussion of the performance of the various differencing methods.

When we compare the UAV point cloud results spatially between the various differencing methods, there is a pronounced difference in the resolution between the DoD (Figure 15a) and the other differencing methods. This is especially the case relative to the M3C2 annual change map (Figure 15d), which shows low resolution. The reduction in resolution of the M2C2 results are due to the algorithm's use of core points that intrinsically reduces the resolution as the data is subsampled. The data range of the M3C2 results is much wider than that of the other differencing methods (Table 3). When the whiskers on the boxplots in Figure 16 are considered, we see that M3C2 has more outlying data points than the other methods, none of which have outliers beyond the extent of their whiskers. These outliers could be those points on the map (Figure 15d) which do not appear spatially relevant. These misplaced, seemingly erroneous points are also of large magnitude (red and blue), and therefore could possibly be representing the outliers causing the data range inflation. These high magnitude change signal in spatially inappropriate places, which are interpreted as artifacts, occur in areas of topographic complexity (headwall) where the algorithm may be most likely to encounter confusion due to erroneous assignment of normal direction. If these possible outliers were removed, the range of M3C2 data would drop to approximately 7m, which is a similar magnitude as the other differencing methods.

In agreement with Barnhart & Crosby, 2013's comparison of C2M and M3C2, in this study, when considering the proposed method's results separate from those of the UAV data, in most cases M3C2 reported lower magnitude change than C2M (Table 7), and the other methods investigated. The M3C2 method is considered inherently more conservative than C2M as it can convert more displacement measurements to zero if they are deemed insignificant. In this study, M3C2 tended to have mean values more comparable to the other differencing methods when the magnitude of change was smaller. That is to say, that mean values between methods were most similar when time since reference was short, and they were most different when time since reference was long (Figure 22). However, M3C2 results in this study were not culled based on significance report, therefore this behaviour of M3C2 may not have been

realized, despite the appearance. Given the limitations of the map in Figure 15d, M3C2 is not recommended if change detection results are desired to be displaced spatially.

The production of maps to investigate the spatial behaviour of the data also allowed note of artifacts in the C2M Delaunay results (Figure 15b) which appear as triangular geometric shapes in areas of high magnitude change. They appear as unnatural geometric shapes in areas of high magnitude change. The artifacts are a known phenomenon caused by confusion in Delaunay triangulation where vertical surfaces or deviations from the general planar trend occur. These artifacts are most obvious around the headwall and at the slump toe, where deposition (red) appears unnatural geomorphically, and erroneous in terms of spatial occurrence. Like M3C2, the high magnitude values of these artifacts likely place them among the outlying data in the boxplot (Figure 16), and likely contribute to data range inflation. However, if we consider the data range and mean for the C2M Delaunay results in Table 3, we see that it has the narrowest data range relative to the other methods, and the smallest magnitude average change reported. This suggests that the C2M Delaunay results are underreporting the change detected, and that the data ranges are in fact not inflated. It is of course difficult to determine which method should be considered most accurate.

Figure 15c shows the UAV results for C2M cloud differencing using Poisson surface reconstruction for meshing. Like the C2M via Delaunay triangulation result (Figure 15b) the C2M Poisson results (Figure 15c) are of slightly lower resolution than that of the DoD results (Figure 15a), and of higher resolution than the M3C2 results. The C2M Poisson results however, lack the artifacts occurring in the C2M Delaunay results, making it a more appropriate meshing algorithm for this data set, if the user is most interested in representing data spatially. Table 3 shows that the C2M Poisson UAV data range has the smallest minimum value compared to the other differencing methods (-1.4m), and shows little negative data (interpreted as erosion) in Figure 16. Contrariwise, the magnitude of positive change (interpreted as deposition) is very like that of the DoD results (4.851m vs 4.892 respectively). This inconsistency makes it difficult to evaluate the performance of the differencing method compared to the others. Although the C2M Delaunay UAV results appear spatially reliable (Figure 15a), the additional meshing step required makes it still a more computationally taxing choice than M3C2 or DoD, for example.

The C2M - Poisson results (Figures 25c-32c) from the captured datasets have some other advantages and disadvantages of the other differencing methods in terms of the results of this study. They also lack the artifacts present in C2M – Delaunay and M3C2, and is smoothed relative to DoD, which may not be a fault depending on intention of use. If users are interested in data means, C2M- Poisson may

be a better choice, however if interested in data extremes (which inform geomorphic change studies), another method may be superior as the range of data in C2M-Poisson results are inconsistent.

One study found that there are variations in C2M's ability to report change depending on the time interval between epochs. C2M reported a higher magnitude of topographic change over short periods of time (12 h) and a lower magnitude of topographic change over long periods of time (four weeks) when compared to M3C2 (Barnhart & Crosby, 2013). The time interval in this study falls between these extremes, existing on the scale of days, making it possible for either result (over or under estimation) to be the case. C2M should however, underestimate the total change as is calculates distance based on closest points, rather than based on a defined search region which is not weighted by distance from the point being considered (Barnhart & Crosby, 2013).

The DoD spatial maps of the captured data show higher resolution than the other differencing methods, however have more discontinuous surfaces due to a lack of meshing and consideration of surrounding points, both of which would tend to smooth data. This may also be interpreted as advantageous or disadvantageous, depending on the type of information desired. If spatial relationships are of import, DoD's high resolution and lack of resampling would likely be the best differencing method. The empirical results of DoD (Table 7 and Figure 21a) are by no means poor relative to the other differencing methods investigated in this study, and are considered competitive. The DoD map result shows detail not found in the other method's map results, such as the seeming clear delineation of the stream bank at the slump toe. This is most evident in Figure 33a, in which only the data extremes are draped over the orthophoto. We can see that the bank delineation aligns well with its position in the orthophoto. Notice that the stream surface itself is visible, as one would expect, as the average water surface should have little change, and would not be included in the top or bottom 10% of the results. When the DoD data range in Figure 16 and Table 3 is considered, the magnitude of change is higher than in the other differencing methods. Supposing that the M3C2 data extremes are erroneous outliers and were culled, the DoD results would likely have the largest range and largest average change of all the methods tested. This agrees with our understanding of C2M and M3C2 which are known to have issues with underestimation of change detected.

In terms of application, M3C2 requires much less data grooming than DoD or C2M. It does not require creation of a mesh surface as with C2M, and does not require gridding as with DoD. This not only reduces operational time consumption, but also reduces the introduction of error caused by interpolation (meshing) or resampling (gridding). Additionally, cloud subsampling to produce core points further reduces computation time. Unlike DoD, M3C2 functions in 3D space which is necessary for analysis of natural environments, especially if data is collected from non-aerial platforms whose oblique angle of

capture defines vertical surfaces. Moreover, M3C2 results can be gridded and used as a substitute for DoD if a vertical normal angle is enforced. Although not discussed in this study, M3C2 can also report roughness (standard deviation of the points in the vicinity of *i*) and density estimates of each cloud, the statistical significance of each distance with a local confidence interval, providing a more robust interpretation of results. Although lacking these additional metrics, C2M can be as accurate as M3C2 (Lague *et al,* 2013). Given that both the empirical and spatial DoD results have fewer caveats in their interpretation than the other methods investigated, it's suggested that DoD may remain, in this case, the most robust change detection method reviewed. This is of course considering the lack of fine tuning to the M3C2 parameters in this study. The data ranges between differencing methods vary widely when compared over individual dates (Table 7), for which input data was equivalent, implying an overall conclusion that there is a lack of ability to report the accurate magnitude of the data extremes, or change detected.

As was the finding of Barnhart & Crosby, 2013, we are unable to report which technique best represents the actual topographic change occurring in this study's target thaw slump. The geomorphic interpretation of these data intrinsically varies depending on the differencing method chosen. The general spatial congruency in results across the different differencing methods, in both the UAV and proposed method results, including the occurrence of obvious spatial error, suggest that the proposed method is promising in terms of precision and possibly accuracy. Spatially and empirically, the results from the proposed methods are similar to those produced by the UAV derived data, suggesting that the method is also not misrepresenting deformation of target feature, and that the differencing methods are inconsistent regardless of the data source. All these reflections are considered evidence in favour of the functionality of the proposed method, despite the early stage in which its development currently sits and considering the potential influence equipment of higher quality and increased positional reference information for appropriate referencing could have.

6.6 Improvements to the proposed method and future work

The central complication of this study lies in logistics rather than the method itself. The remoteness of the chosen site meant that the data was only able to be collected after the study season was ended, rather than on a regular interval. This limitation did not allow for iterative adjustment, nor improvement to the installation or method. Should the site have been local, repeat visitation would be possible, allowing amelioration based on intermediate results.

The proposed method, in its current presentation, is limited to targets of a certain scale. For example, there was intention to place a second installation at another nearby thaw slump, CB, however

the size of that slump was deemed too large for the resolution possible given the cameras used (Figure 12). It would have not been possible to attain adequate image overlap over the whole thaw slump, given the number of cameras available. Should more cameras, or more powerful cameras (higher resolution) been used, this may not have been the case. Higher resolution cameras could be installed at greater distances from the target, improving overlap without a reduction in the detail required for successful SfM reconstruction. This too represents an inadequacy in the equipment used, rather than the proposed method itself. This limitation should be mitigated as the cost of high quality cameras reduce over time.

A major consideration, should the proposed capture method be reemployed, would be cameras with improved resolution, improved programmability/usability, increased recognition in SfM software, or any combination of these factors. The lack of internal calibration information for the chosen cameras in any of the SfM software investigated presented an immediate concern regarding proper modelling. In addition, given that the camera lacked a view finder and shutter, it was very difficult to use calibration programs to provide the internal parameter information lacking. Most SfM software have knowledge of the internal camera parameters of the most commonly used camera models.

Furthermore, this study employed only Agisoft Photoscan for use in SfM modelling. It's possible that the failure of inclusion of camera position information was a result of the chosen software. Future users of the method should consider investigation of other SfM software, including open source options.

Another important adjustment for future consideration would be to use the smallest capture interval available, or even record in video. In this way, issues with inconsistent interval alignment, lighting or atmospheric interference would be reduced or eliminated as the user could choose images over the scale of seconds or minutes, rather than portions of hours. It could be argued that when considering change detection on RTS, acquisition gaps of more than a few minutes could lead to misalignment in the geomorphic state of the feature, as their rate of change varies greatly over time, possibly over the scale of minutes. This adjustment would provide a less sensitive data set, ensuring a lower proportion of excluded data. However, the amount of data collected would greatly increase, as could possibly the amount of preprocessing time required. Contrarily, the improved alignment of images across the array would likely reduce the amount of post processing assigned to trial and error in modelling (masking, chunking, etc.).

Another improvement to the method would be to have more validation data. Additional UAV surveys over the study period for validation would provide redundancy and improve confidence in the method's performance. Additional UAV surveys however would increase field time, which reduces the attractiveness of the method in remote areas. It's possible that training locals to execute automated UAV flights without supervision may be a possibility not far into the future. The D1 slump investigated in this study offers a good opportunity for continued work with the proposed methods as it has close access by

road, a general location that is proximal to other RTS and is therefore frequented, and a baseline of three years of data against which to build a long-term study.

The data sets used for modelling in this study were much smaller than used on average in SfM (11 images compared to often hundreds), and therefore computational time consumed in modelling was short. This was similarly the case in terms of analysis done within Cloud Compare, as most work in that software, including cloud differencing, was quite quick. The most time-consuming portion of the exercise, such as interpolations, could be mitigated with the introduction of batch processes. The proposed method would greatly benefit from computation automation, as well as the acquisition automation which had been the focus.

Future iterations of the proposed method should consider the limitations discussed and improvements suggested, however deciding the installation geometry in complex and dangerous environments remains the most challenging aspect of the proposed method and remains in need of human expertise and interpretation. The installation requirements of any site vary depending on the morphology and surrounding topography, which dictates the availability of installation positions. Study site selection will remain a main factor, regardless of technological advancement, as is the case with any change detection studies in dynamic or dangerous natural environments. The proposed method is therefore not recommended for large targets such as glaciers or mega slumps, as they require aerial acquisition to capture their large extent and higher obliquity than could be supplied by ground based installations of any kind. The proposed method is also limited to targets that adhere to the requirements of SfM, as is the case with any method employing SfM. Highly reflective surfaces or those with little optical heterogeneity, such as water or snow, are not recommended until SfM algorithms have evolved to address the complexities of such targets.

The proposed method would also be well suited for targets of smaller scale than considered in this study. A stationary array of cameras could be used to study the seasonal change of a target at the scale of a tree or shrub, for example. The complexities involved in proper geometric design would be vastly reduced should the size of the array be larger than that of the target of interest.

Overall, the proposed method would provide a robust alternative for ground based change detection studies in difficult environments, as the necessity to revisit or survey such a target is greatly reduced, while at the same time increasing the volume of data collected. This point lends the proposed method to further development as the cumulative potential benefits outweigh the current limitations.

6.7 Novelty of method

Although the results of this study were not adequately robust as to allow statistical analysis of results, the method presents innovation in terms of increased temporal resolution and automation of topographic data collection when compared to existing methods. The main limitation of the method proposed is the cost of high resolution cameras. Despite the current cost of SLR cameras, they remain less costly than ranging technologies, especially if employed at a high temporal frequency, and in remote areas. Should the method by redeployed with higher quality cameras, the cost of the subsequent data produced would still be less than with current technology.

The anticipated drop in cost for SLR cameras will further drive down the cost of the proposed method, potentially making it feasible for employment in other fields of science as well. It's possible that this method could be a useful technique to any field of science, even external to geosciences, in which high temporal resolution change detection is desired. The technique would be advantageous in study of phenology, where qualitative growth patterns and quantitative biomass calculations could be compared to solar input, for example. In civil and geoengineering, the technique could allow real time monitoring of infrastructure or geological stability, and potentially contribute to early warning systems for hazard monitoring. A system could be designed in which a large installation monitors for deformation with the support of an alarm system triggered by deformation beyond an established threshold.

The future capacity of the proposed method in terms of geomorphic study of retrogressive thaw slumps in permafrost environments is yet to be determined, but presents promise in terms of data gaps in current understanding of the factors responsible for their activity. Should the data quality produced by the proposed method improve, there is potential to assess retreat rate quantitatively, as a function of time and/or weather events, for example, which could provide support for existing hypothesis concerning the relation between RTS retreat and local precipitation events. Furthermore, by increasing the temporal resolution of high resolution data of RTS, as is offered with the proposed method, one may expect to have the capacity to investigate the sediment and ground ice characteristics of permafrost, the differences in growth characteristics of individual disturbances, and contrast in thaw slumps among regions (Kokelj *et al*., 2015). Such insight could help advance the understanding of RTS and how we may expect their behavior to change depending on the surficial materials present or prevailing climate trends in that feature's immediate environment.

7 Conclusions

The presence of a trend in the mean elevation change data between differencing methods, but not in data range, suggests that the data capture method proposed can articulate the overall deformation at the study site with some precision, however while lacking accuracy. If such precision is possible with the

high level of modeling challenges this data set faced, one might expect that use of higher quality cameras, increased capture interval, optimized SfM geometry (increased data redundancy), or any combination of these improvements, may produce an approachable, semi-automated field method, with competitive results. It could be argued that the trend in mean elevation change supports the viability of the proposed capture method, and that the lack of congruency in data range between differencing methods suggests need for further investigation, development and adjustment in terms of analyses and differencing algorithms employed.

Increased use of positional information for rigorous accuracy assessment would result in an increasingly quantitative analysis, as opposed to the qualitative results available to this study. Increased quantitative metric would also allow a clearer trajectory in future iterations and subsequently, a more rapid evolution of the method.

REFERENCES

Agisoft, L. L. C. (2013). Agisoft PhotoScan user manual. Professional edition, version 0.9. 0.

Balser, A. W., Jones, J. B., & Gens, R. (2014). Timing of retrogressive thaw slump initiation in the Noatak Basin, northwest Alaska, USA. *Journal of Geophysical Research: Earth Surface*, *119*(5), 1106-1120.

Bamber, J., Krabill, W., Raper, V. and Dowdeswell, J., 2005. Interpretation of elevation changes on Svalbard glaciers and ice caps from airborne lidar data. Annals of Glaciology, 42: 202–208.

Barker, R., Dixon, L., & Hooke, J. (1997). Use of terrestrial photogrammetry for monitoring and measuring bank erosion. *Earth Surface Processes and Landforms*, *22*(13), 1217-1227.

Barnhart, T. B., Crosby, B. T., Derryberry, D. R., & Rowland, J. C. (2013, December). Using High-temporal-resolution, Repeat Terrestrial LiDAR to Compare Topographic Change Detection Methods and to Elucidate the Hydrometeorologic Controls on the Retreat Rate and Form of the Selawik Retrogressive Thaw Slump, Northwest Alaska. In *AGU Fall Meeting Abstracts* (Vol. 1, p. 0966).

Barnhart, T. B., & Crosby, B. T. (2013). Comparing two methods of surface change detection on an evolving thermokarst using high-temporal-frequency terrestrial laser scanning, Selawik River, Alaska. *Remote Sensing*, *5*(6), 2813-2837.

Bauer, T., Strauss, P., & Murer, E. (2014). A photogrammetric method for calculating soil bulk density §. *Journal of Plant Nutrition and Soil Science*, *177*(4), 496-499.

Bauer, T., James, M. R., McShane, G., Quinton, J. N., & Strauss, P. (2015, April). Intra-rainfall soil surface change detection using close-range photogrammetry. In *EGU General Assembly Conference Abstracts* (Vol. 17, p. 1587).

Bolitho, M., Kazhdan, M., Burns, R., & Hoppe, H. (2009). Parallel poisson surface reconstruction. *Advances in Visual Computing*, 678-689.

Brooker, A., Fraser, R.H., Olthof, I., Kokelj, S.V., Lacelle, D., 2014. Mapping the activity and evolution of retrogressive thaw slumps by Tasseled Cap trend analysis of a Landsat satellite image stack. Permafr. Periglac. Process. 25, 243–256.

Burn, C. R., & Lewkowicz, A. G. (1990). CANADIAN LANDFORM EXAMPLES - 17 RETROGRESSIVE THAW SLUMPS. *The Canadian Geographer/Le Géographe canadien*, *34*(3), 273-276.

Burn, C.R., Kokelj, S.V., 2009. The permafrost and environment of the Mackenzie Delta area. Permafr. Periglac. Process. 20, 83–105.

Cerminaro, D. J. (2014). Implementation of photogrammetry to improve proactive assessment of retaining

walls along transportation corridors.

Chandler, J. H. and Brunsden, D., 1995. Steady state behaviour of the Black Ven mudslide: the application of archival analytical photogrammetry to studies of landform change. Earth Surface Processes and Landforms, 20(3): 255–275.

Chandler, J. (1999). TECHNICAL COMMUNICATIONS-Effective Application of Automated Digital Photogrammetry for Geomorphological Research. *Earth Surface Processes and Landforms*, *24*(1), 51-64.

Chandler, J. H., Shiono, K., Rameshwaren, P. and Lane, S. N., 2001. Measuring flume surfaces for hydraulics research using a Kodak DCS460. Photogrammetric Record, 17(97): 39–61.

Chandler, J., Ashmore, P., Paola, C., Gooch, M., & Varkaris, F. (2002). Monitoring river-channel change using terrestrial oblique digital imagery and automated digital photogrammetry. *Annals of the Association of American Geographers*, *92*(4), 631-644.

Chandler, J. H., Buffin-Belanger, T., Rice, S., Reid, I. and Graham, D. J., 2003. The accuracy of a river bed moulding/casting system and the effectiveness of a low-cost digital camera for recording river bed fabric. Photogrammetric Record, 18(103): 209–223.

Chandler, J. H., Fryer, J. G., & Jack, A. (2005). Metric capabilities of low - cost digital cameras for close range surface measurement. *The Photogrammetric Record*, *20*(109), 12-26.

Chernos, M. (2014). The relative importance of calving and surface ablation at a lacustrine terminating glacier: a detailed assessment of ice loss at Bridge Glacier, British Columbia.

Chin, K. S., Lento, J., Culp, J. M., Lacelle, D., & Kokelj, S. V. (2016). Permafrost thaw and intense thermokarst activity decreases abundance of stream benthic macroinvertebrates. *Global change biology*.

Copland, L., Pope, S., Bishop, M. P., Shroder, J. F., Clendon, P., Bush, A., ... & Owen, L. A. (2009). Glacier velocities across the central Karakoram. *Annals of Glaciology*, *50*(52), 41-49.

Grom, J. D. (2008). Retrogressive thaw slump process and morphology, Eureka Sound Lowlands, Ellesmere Island, Nunavut, Canada (Doctoral dissertation, McGill University).

EDF R&D. Cloudcompare (version 2.4) [gpl software]. Technical report, Telecom ParisTech Paris, 2012.

Eiken, T., & Sund, M. (2012). Photogrammetric methods applied to Svalbard glaciers: accuracies and challenges. *Polar Research*, *31*.

Environment Canada, 2015. National Climate Data and Information Archive, Fort McPherson, NWT. http://climate.weather.gc.ca.

Feng, T., Liu, X., Scaioni, M., Lin, X., & Li, R. (2012, May). Real-time landslide monitoring using close-range stereo image sequences analysis. In *Systems and Informatics (ICSAI), 2012 International*

Conference on (pp. 249-253). IEEE.

Fonstad, M. A., Dietrich, J. T., Courville, B. C., Jensen, J. L., & Carbonneau, P. E. (2013). Topographic structure from motion: a new development in photogrammetric measurement. *Earth Surface Processes and Landforms*, *38*(4), 421-430.

Furukawa, Y., Curless, B., Seitz, S. M., & Szeliski, R. (2010, June). Towards internet-scale multi-view stereo. In *Computer Vision and Pattern Recognition (CVPR), 2010 IEEE Conference on* (pp. 1434-1441). IEEE.

Glenn NF, Streutker DR, Chadwick DJ, Thackray GD, Dorsch SJ. 2006. Analysis of LiDAR- derived topo- graphic information for characterizing and differentiating landslide morphology and activity. Geomorphology 73(1–2): 131–148.

Hancock, G. and Willgoose, G., 2001. The production of digital elevation models for experimental model landscapes. Earth Surface Processes and Landforms, 26(5): 475–490.

Haneberg, W. C. (2008). Using close range terrestrial digital photogrammetry for 3-D rock slope modeling and discontinuity mapping in the United States. *Bulletin of Engineering Geology and the Environment*, *67*(4), 457-469.

Hottier, P., 1976. Accuracy of close-range analytical restitutions: practical experiments and prediction. Photogrammetric Engineering & Remote Sensing, 42(3): 345–375.

Hsiao, K. H., Liu, J. K., Yu, M. F., & Tseng, Y. H. (2004, July). Change detection of landslide terrains using ground-based lidar data. In *XXth ISPRS Congress, Istanbul, Turkey, Commission VII, WG* (Vol. 7, No. 5, p. 5).

James, T. D., Murray, T., Barrand, N. E., & Barr, S. L. (2006). Extracting photogrammetric ground control from lidar DEMs for change detection. *The Photogrammetric Record*, *21*(116), 312-328.

James, L. A., Hodgson, M. E., Ghoshal, S., & Latiolais, M. M. (2012). Geomorphic change detection using historic maps and DEM differencing: The temporal dimension of geospatial analysis. *Geomorphology*, *137*(1), 181-198.

James, M. R., & Robson, S. (2014). Sequential digital elevation models of active lava flows from ground-based stereo time-lapse imagery. *ISPRS Journal of Photogrammetry and Remote Sensing*, *97*, 160-170.

Janeras, M., Navarro, M., Arnó, G., Ruiz, A., Kornus, W., Talaya, J., ... & López, F. (2004, September). LIDAR APPLICATIONS TO ROCK FALL HAZARD ASSESMENT IN VALL DE NÚRIA. In *Proceedings, 4th ICA Mountain Cartography Workshop, Vall de Núria, Catalonia, Spain* (pp. 1-14).

Jiang, R., Jáuregui, D. V., & White, K. R. (2008). Close-range photogrammetry applications in bridge measurement: literature review. *Measurement*, *41*(8), 823-834.

Jones, B. M., Stoker, J. M., Gibbs, A. E., Grosse, G., Romanovsky, V. E., Douglas, T. A., ... &

Richmond, B. M. (2013). Quantifying landscape change in an arctic coastal lowland using repeat airborne LiDAR. *Environmental Research Letters*, *8*(4), 045025.

Kääb, A. (2008). Remote sensing of permafrost - related problems and hazards. *Permafrost and Periglacial Processes*, *19*(2), 107-136.

Kääb, A., Girod, L. M. R., & Berthling, I. T. (2014). Surface kinematics of periglacial sorted circles using structure-from-motion technology. *The Cryosphere*, *8*, 1041-1056.

Kokelj, S.V., Jorgenson, T., 2013. Advances in thermokarst research. Permafr. Periglac. 24, 108–119.

Kokelj, S. V., Lantz, T. C., Kanigan, J., Smith, S. L., & Coutts, R. (2009). Origin and polycyclic behaviour of tundra thaw slumps, Mackenzie Delta region, Northwest Territories, Canada. *Permafrost and Periglacial Processes*, *20*(2), 173-184.

Kokelj, S. V., Tunnicliffe, J., Lacelle, D., Lantz, T. C., Chin, K. S., & Fraser, R. (2015). Increased precipitation drives mega slump development and destabilization of ice-rich permafrost terrain, northwestern Canada. *Global and Planetary Change*, *129*, 56-68.

Krieger, K., Crosby, B. T., Phillips, C., Godsey, S., & Jerolmack, D. J. (2009, December). Slump Scaling: Common Geometries Observed from Retrogressive Thaw Slumps in Three Different Environments in Arctic Alaska. In *AGU Fall Meeting Abstracts* (Vol. 1, p. 0044).

Krosley, L., Oerter, E., Ortiz, T., & Ortiz, T. (2006, January). Digital ground-based photogrammetry for measuring discontinuity orientations in steep rock exposures. In *Golden Rocks 2006, The 41st US Symposium on Rock Mechanics (USRMS)*. American Rock Mechanics Association.

Lacelle, D., Bjornson, J., Lauriol, B., Clark, I.D., Troutet, Y., 2004. Segregated-intrusive ice of subglacial meltwater origin in retrogressive thaw flow headwalls, Richardson Mountains, NWT, Canada. Quat. Sci. Rev. 23, 681–696.

Lacelle, D., Bjornson, J., Lauriol, B., 2010. Climatic and geomorphic factors affecting con- temporary (1950–2004) activity of retrogressive thaw slumps on the Aklavik Plateau, Richardson Mountains, NWT, Canada. Permafr. Periglac. Process. 21, 1–15.

Lacelle, D., Brooker, A., Fraser, R.H., Kokelj, S.V., 2015. Distribution and growth of thaw slumps in the Richardson Mountains – Peel Plateau region, northwestern Canada. Geomorphology 235, 40–51.

Lague, D., Brodu, N., & Leroux, J. (2013). Accurate 3D comparison of complex topography with terrestrial laser scanner: Application to the Rangitikei canyon (NZ). *ISPRS Journal of Photogrammetry and Remote Sensing*, *82*, 10-26.

Lane, S. N., James, T. D. and Crowell, M. D., 2000. Application of digital photogrammetry to complex topography for geomorphological research. Photogrammetric Record, 16(95): 793–821.

Lantuit, H., Pollard, W.H., 2005. Temporal stereophotogrammetric analysis of retrogressive thaw slumps

on Herschel Island, Yukon Territory. Nat. Hazards Earth Syst. Sci. 5, 413–423.

Lantuit, H., & Pollard, W. H. (2008). Fifty years of coastal erosion and retrogressive thaw slump activity on Herschel Island, southern Beaufort Sea, Yukon Territory, Canada. *Geomorphology*, *95*(1), 84-102.

Lantz, T. C., & Kokelj, S. V. (2008). Increasing rates of retrogressive thaw slump activity in the Mackenzie Delta region, NWT, Canada. *Geophysical Research Letters*, *35*(6).

Lantz, T., Kokelj, S.V., Gergel, S.E., Henry, G.H., 2009. Relative impacts of disturbance and temperature: persistent changes in microenvironment and vegetation in retrogressive thaw slumps. Glob. Chang. Biol. 15, 1664–1675.

Lawless, M. and Robert, A., 2001. Three-dimensional flow structure around small-scale bedforms in a simulated gravel-bed environment. Earth Surface Processes and Landforms, 26(5): 507–522.

Leon, J. X., Roelfsema, C. M., Saunders, M. I., & Phinn, S. R. (2015). Measuring coral reef terrain roughness using 'Structure-from-Motion' close-range photogrammetry. *Geomorphology*, *242*, 21-28.

Levy, J. S., Fountain, A. G., Dickson, J. L., Head, J. W., Okal, M., Marchant, D. R., & Watters, J. (2013). Accelerated thermokarst formation in the McMurdo Dry Valleys, Antarctica. *Scientific reports*, *3*.

Lewkowicz, A. G. (1987). Headwall retreat of ground-ice slumps, Banks Island, Northwest Territories. *Canadian Journal of Earth Sciences*, *24*(6), 1077-1085.

Lindenbergh, R., & Pietrzyk, P. (2015). Change detection and deformation analysis using static and mobile laser scanning. *Applied Geomatics*, *7*(2), 65-74.

Lu, D., Mausel, P., Brondizio, E., & Moran, E. (2004). Change detection techniques. *International journal of remote sensing*, *25*(12), 2365-2401.

Lucieer, A., Turner, D., King, D. H., & Robinson, S. A. (2014). Using an Unmanned Aerial Vehicle (UAV) to capture micro-topography of Antarctic moss beds. *International Journal of Applied Earth Observation and Geoinformation*, *27*, 53-62.

Mackay, J. R. (1966). Segregated epigenetic ice and slumps in permafrost. *Mackenzie Delta area, NWT Geographical Bulletin*, *8*(1), 59-80.

Mackay JR. 1967. Permafrost depths, lower Mackenzie valley, Northwest Territories. 1967. Arctic 20: 21–26.

Maiti, A., & Chakravarty, D. (2016). Performance analysis of different surface reconstruction algorithms for 3D reconstruction of outdoor objects from their digital images. *SpringerPlus*, *5*(1), 932.

Malone, L., Lacelle, D., Kokelj, S.V., Clark, I.D., 2013. Impacts of hillslope thaw slumps on the geochemistry of permafrost catchments (Stony Creek watershed, NWT, Canada). Chem. Geol. 356, 38–49.

Micheletti, N., Chandler, J. H., & Lane, S. N. (2015). Investigating the geomorphological potential of

freely available and accessible structure - from - motion photogrammetry using a smartphone. *Earth Surface Processes and Landforms*, *40*(4), 473-486.

Mora, P., Baldi, P., Casula, G., Fabris, M., Ghirotti, M., Mazzini, E., & Pesci, A. (2003). Global Positioning Systems and digital photogrammetry for the monitoring of mass movements: application to the Ca'di Malta landslide (northern Apennines, Italy). *Engineering Geology*, *68*(1), 103-121.

Niethammer, U., James, M. R., Rothmund, S., Travelletti, J., & Joswig, M. (2012). UAV-based remote sensing of the Super-Sauze landslide: Evaluation and results. *Engineering Geology*, *128*, 2-11.

Nolan, M., & DesLauriers, K. (2016). Which are the highest peaks in the US Arctic? Fodar settles the debate. *The Cryosphere*, *10*(3), 1245-1257.

Obu, J., Lantuit, H., Grosse, G., Günther, F., Sachs, T., Helm, V., & Fritz, M. (2016). Coastal erosion and mass wasting along the Canadian Beaufort Sea based on annual airborne LiDAR elevation data. *Geomorphology*.

Olefeldt, D., Goswami, S., Grosse, G., Hayes, D., Hugelius, G., Kuhry, P., ... & Turetsky, M. R. (2016). Circumpolar distribution and carbon storage of thermokarst landscapes. *Nature communications*, *7*.

O'Neill, H. B., Burn, C. R., & Kokelj, S. V. (2015). Field measurements of permafrost conditions beside the Dempster Highway embankment, Peel Plateau, NWT. In *Proceedings from Conference: GEOQuébec*.

O'Neill, H. B., Burn, C. R., Kokelj, S. V., & Lantz, T. C. (2015). 'Warm'Tundra: Atmospheric and Near - Surface Ground Temperature Inversions Across an Alpine Treeline in Continuous Permafrost, Western Arctic, Canada. *Permafrost and Periglacial Processes*, *26*(2), 103-118.

Pitkanen T, Kajutti K. 2004. Close-range photogrammetry as a tool in glacier change detection. ISPRS International Archives of Photogrammetry, Remote Sensing and Spatial Information Sciences. XXX(B7): 769–773.

Rieke - Zapp, D. H., & Nearing, M. A. (2005). Digital close range photogrammetry for measurement of soil erosion. *The Photogrammetric Record*, *20*(109), 69-87.

Rivera, A., Corripio, J., Bravo, C., & Cisternas, S. (2012). Glaciar Jorge Montt (Chilean Patagonia) dynamics derived from photos obtained by fixed cameras and satellite image feature tracking. *Annals of Glaciology*, *53*(60), 147-155.

Romanovsky, V.E., Smith, S.L., Christiansen, H.H., 2010. Permafrost thermal state in the polar Northern Hemisphere during the International Polar Year 2007-2009: a synthesis. Permafr. Periglac. 21, 106–116.

Rovero, F., Zimmermann, F., Berzi, D., & Meek, P. (2013). " Which camera trap type and how many do I need?" A review of camera features and study designs for a range of wildlife research

applications. *Hystrix, the Italian Journal of Mammalogy*, *24*(2), 148-156.

Sauber, J., Molnia, B., Carabajal, C., Luthcke, S., & Muskett, R. (2005). Ice elevations and surface change on the Malaspina Glacier, Alaska. *Geophysical Research Letters*, *32*(23).

Segal, R. A., Lantz, T. C., & Kokelj, S. V. (2016). Acceleration of thaw slump activity in glaciated landscapes of the Western Canadian Arctic. *Environmental Research Letters*, *11*(3), 034025.

Séjourné, A., Costard, F., Fedorov, A., Gargani, J., Skorve, J., Massé, M., & Mège, D. (2015). Evolution of the banks of thermokarst lakes in Central Yakutia (Central Siberia) due to retrogressive thaw slump activity controlled by insolation. *Geomorphology*, *241*, 31-40.

Serreze, M. C., Barrett, A. P., Stroeve, J. C., Kindig, D. N., & Holland, M. M. (2009). The emergence of surface-based Arctic amplification. *The Cryosphere*, *3*(1), 11-19.

Shewchuk, J. R. (2002). Delaunay refinement algorithms for triangular mesh generation. *Computational geometry*, *22*(1-3), 21-74.

Short, N., Brisco, B., Couture, N., Pollard, W., Murnaghan, K., & Budkewitsch, P. (2011). A comparison of TerraSAR-X, RADARSAT-2 and ALOS-PALSAR interferometry for monitoring permafrost environments, case study from Herschel Island, Canada. *Remote Sensing of Environment*, *115*(12), 3491-3506.

Snavely N, Seitz SM, Szeliski R. 2006. Photo tourism: exploring photo collections in 3D. ACM Transactions on Graphics 25(3): 835–846.

Snavely N, Seitz SM, Szeliski R. 2008. Modeling the world from Internet photo collections. International Journal of Computer Vision 80 (12): 189–210.

Stojic, M., Chandler, J. H., Ashmore, P. and Luce, J., 1998. The assessment of sediment transport rates by automated digital photogrammetry. Photogrammetric Engineering & Remote Sensing, 64(5): 387–395.

Stumpf, A., Malet, J. P., Allemand, P., Pierrot-Deseilligny, M., & Skupinski, G. (2015). Ground-based multi-view photogrammetry for the monitoring of landslide deformation and erosion. *Geomorphology*, *231*, 130-145.

Sund, M., Eiken, T., & Rolstad Denby, C. (2011). Velocity structure, front position changes and calving of the tidewater glacier Kronebreen, Svalbard. *The Cryosphere Discussions*, *5*(1), 41-73.

Swanson, D. K. and K. Hill. 2010. Monitoring of retrogressive thaw slumps in the Arctic Network, 2010 baseline data: Three-dimensional modeling with small-format aerial photographs. Natural Resource Data Series NPS/ARCN/NRDS—2010/123. National Park Service, Fort Collins, Colorado.

Swanson, D.K., 2012. Monitoring of Retrogressive Thaw Slumps in the Arctic Net- work, 2011: Three-Dimensional Modeling of Landform Change. Natural Resource Report NPS/ARCN/NRDS—2012/247. National Park Service, Fort Collins, Colorado, p. 60.

Taboga, A. (2011). *Development of integrated high-resolution geophysical, photogrammetric and GPS surveying applied to landslides in the South Wales coalfield*.

Thoma, D. P., Gupta, S. C., Bauer, M. E. and Kirchoff, C. E., 2005. Airborne laser scanning for riverbank erosion assessment. Remote Sensing of Environment, 95(4): 493–501.

Turner, D., Lucieer, A., & de Jong, S. M. (2015). Time series analysis of landslide dynamics using an unmanned aerial vehicle (UAV). *Remote Sensing*, *7*(2), 1736-1757.

Van Wychen, W., Copland, L., Gray, L., Burgess, D., Danielson, B., & Sharp, M. (2012). Spatial and temporal variation of ice motion and ice flux from Devon Ice Cap, Nunavut, Canada. *Journal of Glaciology*, *58*(210), 657-664.

Walstra, J., Chandler, J. H., Dixon, N. and Dijkstra, T. A., 2004. Time for change—quantifying landslide evolution using historical aerial photographs and modern photogrammetric methods. International Archives of the Photogrammetry, Remote Sensing and Spatial Information Sciences, 35(4): 475–480.

Wang, B. (2011). Retrogression rate of thaw slumps in permafrost–an update from the latest monitoring data.

Wangensteen B, Eiken T, Odegard RS, Sollid JL. 2007. Measuring coastal cliff retreat in the Kongsfjorden area, Svalbard, using terrestrial photogrammetry. Polar Research 26(1): 14–21.
Wdowinski, S., Kim, S. W., Amelung, F., Dixon, T. H., Miralles-Wilhelm, F., & Sonenshein, R. (2008). Space-based detection of wetlands' surface water level changes from L-band SAR interferometry. *Remote Sensing of Environment*, *112*(3), 681-696.

Westoby, M. J., Brasington, J., Glasser, N. F., Hambrey, M. J., & Reynolds, J. M. (2012). 'Structure-from-Motion'photogrammetry: A low-cost, effective tool for geoscience applications. *Geomorphology*, *179*, 300-314.

APPENDIX A

Maps: Spatial Visualization of Results

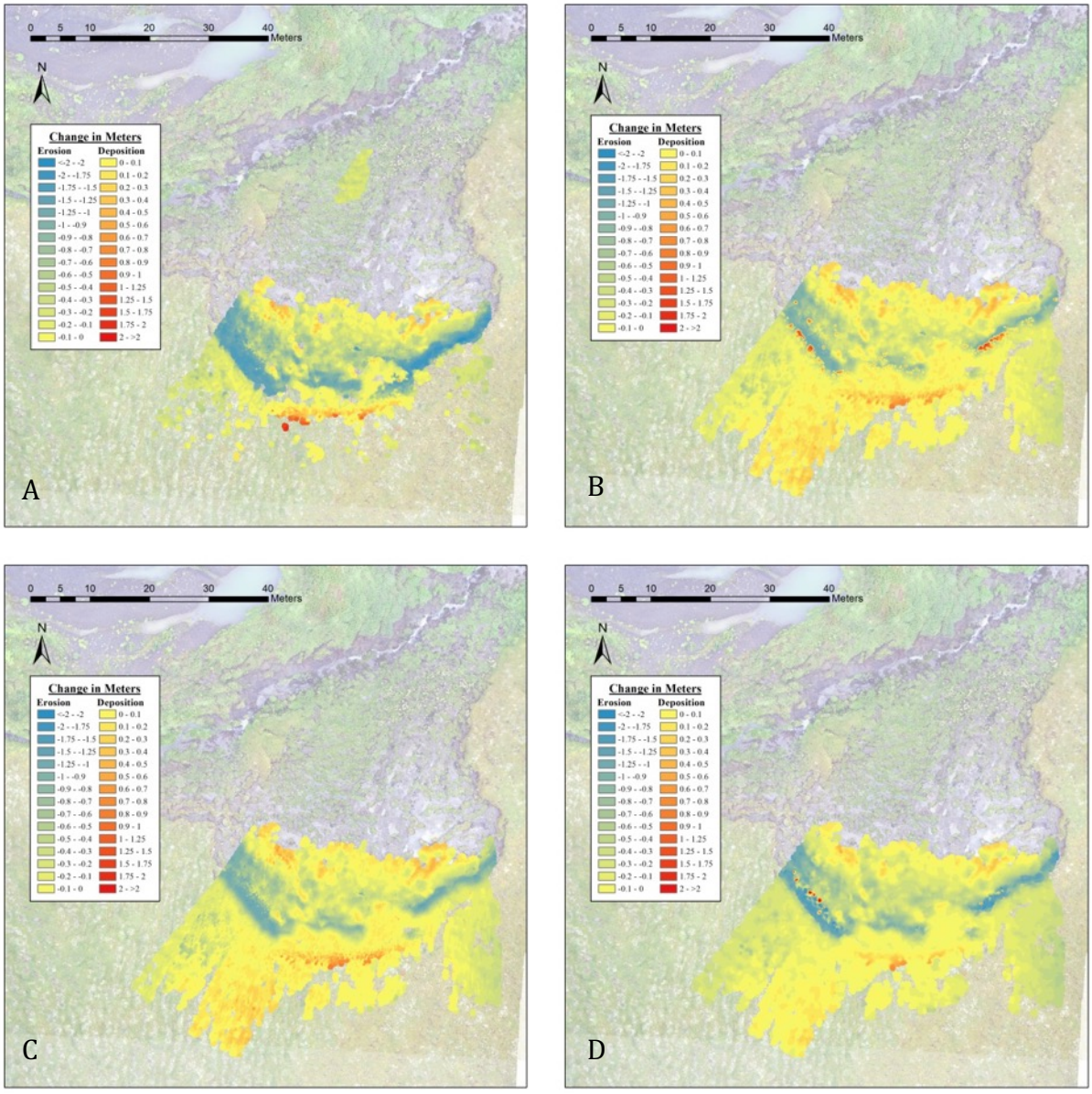

Figure 25. Elevation change results of SfM models at D1 (relative to August 3, 2016 UAV reference model) derived from camera array on June 27, 2017. A) DEMs of Difference (DoDs); B) Cloud to Mesh (C2M) distances (via Delaunay triangulation mesh; C) Cloud to Mesh (C2M) distances (via Poisson mesh); D) Multiscale Model to Model Cloud Comparison (M3C2) distances.

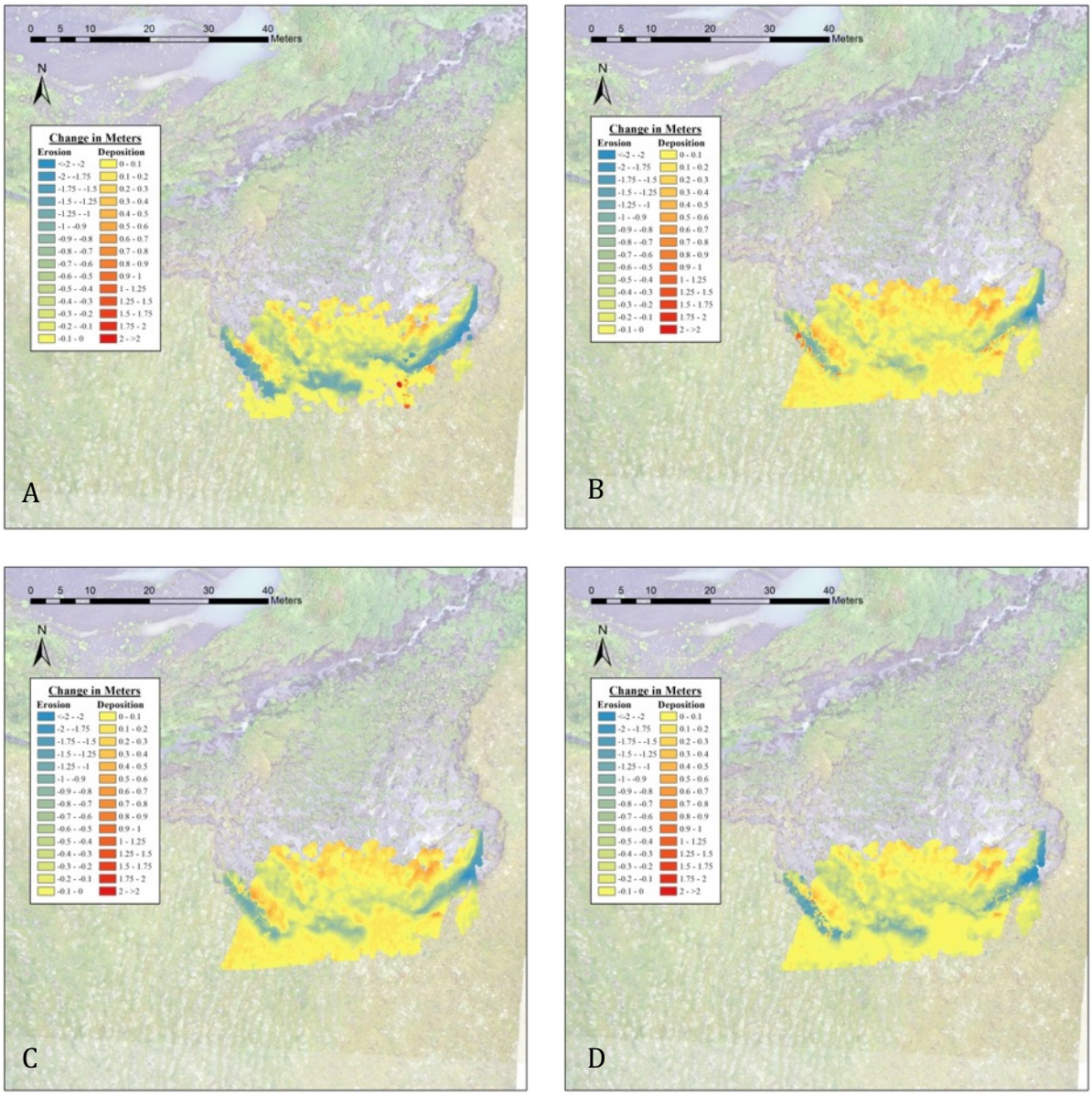

Figure 26. Elevation change results of SfM models at D1 (relative to August 3, 2016 UAV reference model) derived from camera array on July 7, 2017. A) DEMs of Difference (DoDs); B) Cloud to Mesh (C2M) distances (via Delaunay triangulation mesh; C) Cloud to Mesh (C2M) distances (via Poisson mesh); D) Multiscale Model to Model Cloud Comparison (M3C2) distances.

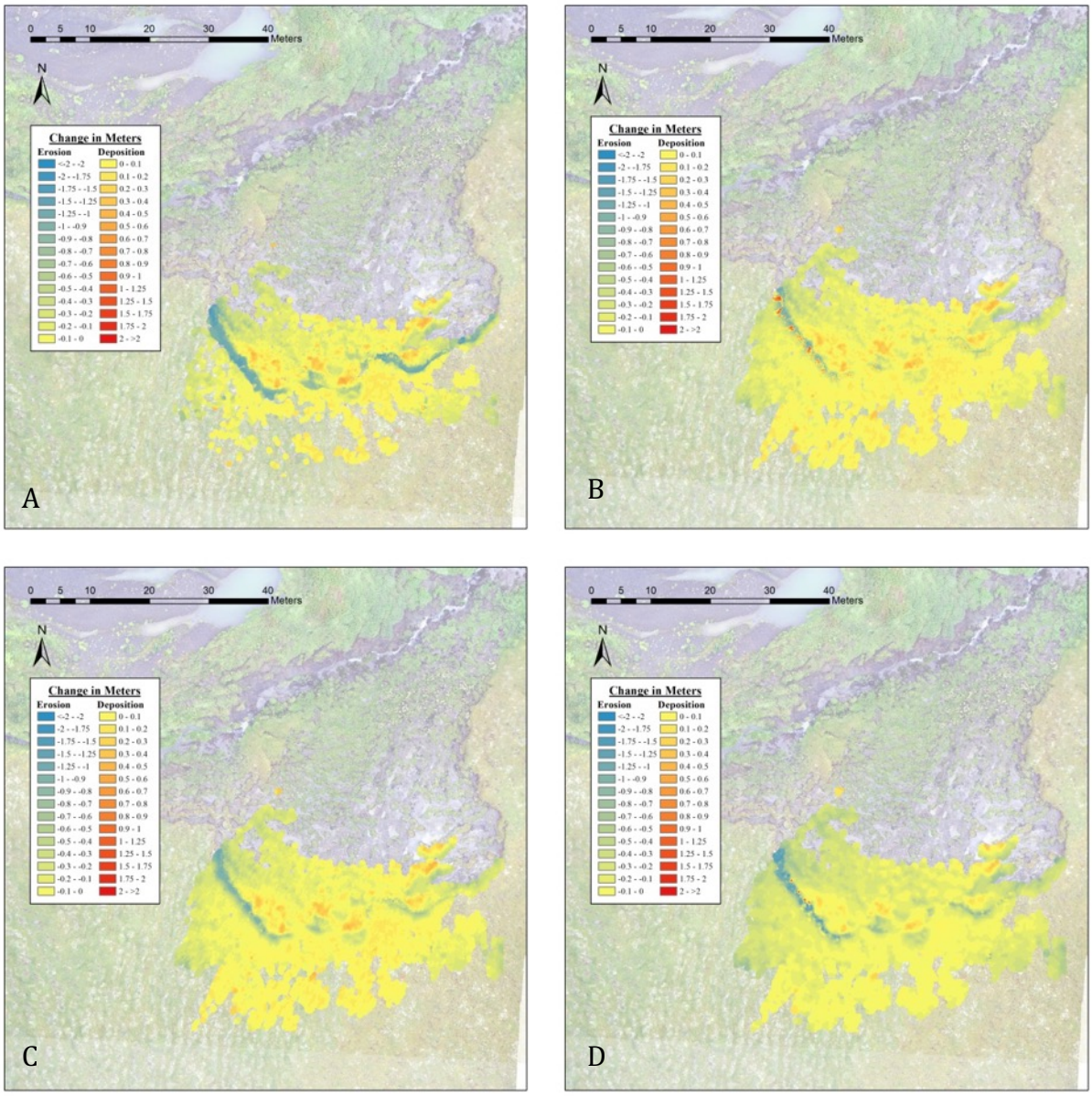

Figure 27. Elevation change results of SfM models at D1 (relative to August 3, 2016 UAV reference model) derived from camera array on July 17, 2017. A) DEMs of Difference (DoDs); B) Cloud to Mesh (C2M) distances (via Delaunay triangulation mesh; C) Cloud to Mesh (C2M) distances (via Poisson mesh); D) Multiscale Model to Model Cloud Comparison (M3C2) distances.

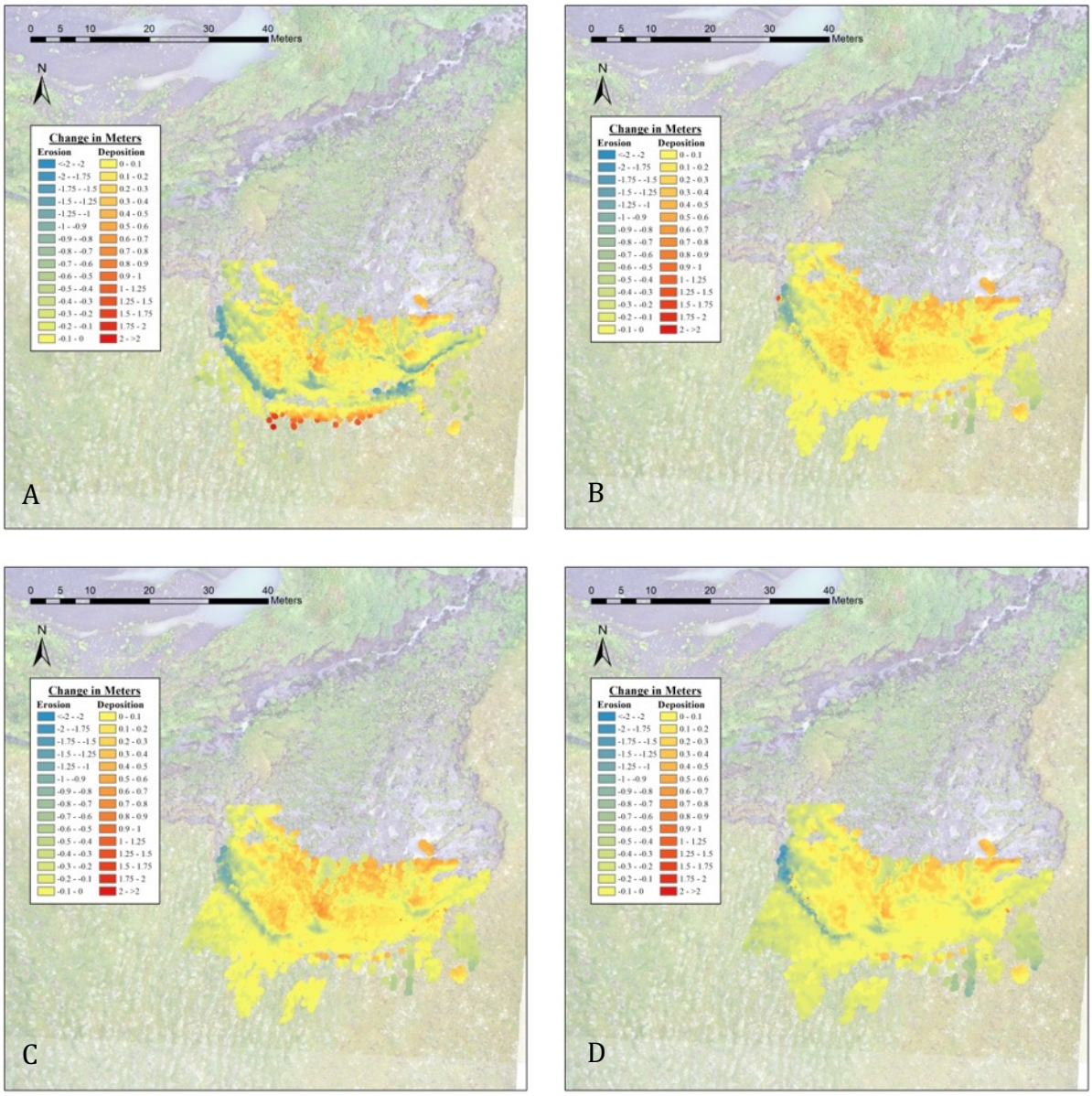

Figure 28. Elevation change results of SfM models at D1 (relative to August 3, 2016 UAV reference model) derived from camera array on July 25, 2017. A) DEMs of Difference (DoDs); B) Cloud to Mesh (C2M) distances (via Delaunay triangulation mesh; C) Cloud to Mesh (C2M) distances (via Poisson mesh); D) Multiscale Model to Model Cloud Comparison (M3C2) distances.

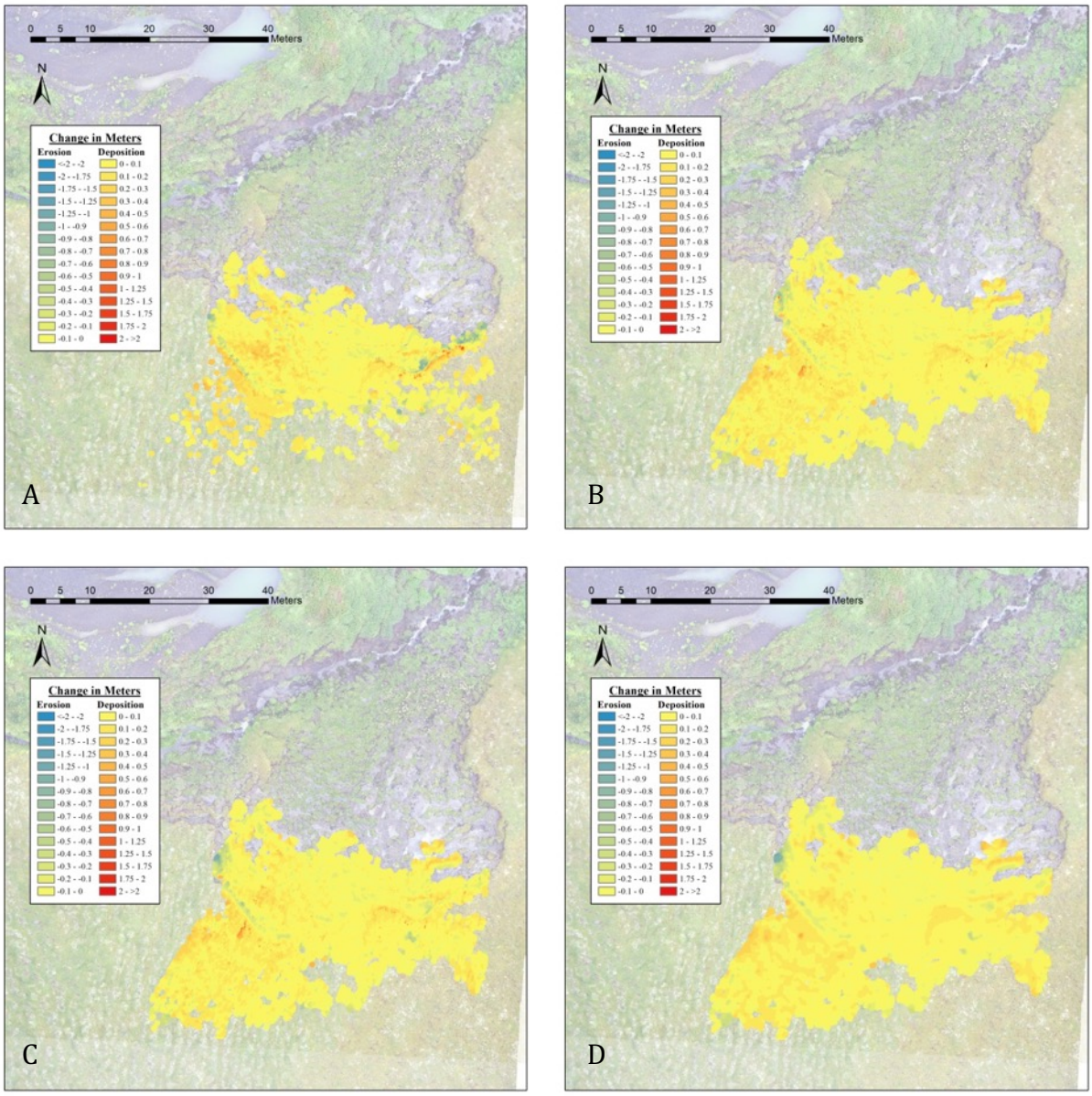

Figure 29. Elevation change results of SfM models at D1 (relative to August 3, 2016 UAV reference model) derived from camera array on August 1, 2017. A) DEMs of Difference (DoDs); B) Cloud to Mesh (C2M) distances (via Delaunay triangulation mesh; C) Cloud to Mesh (C2M) distances (via Poisson mesh); D) Multiscale Model to Model Cloud Comparison (M3C2) distances.

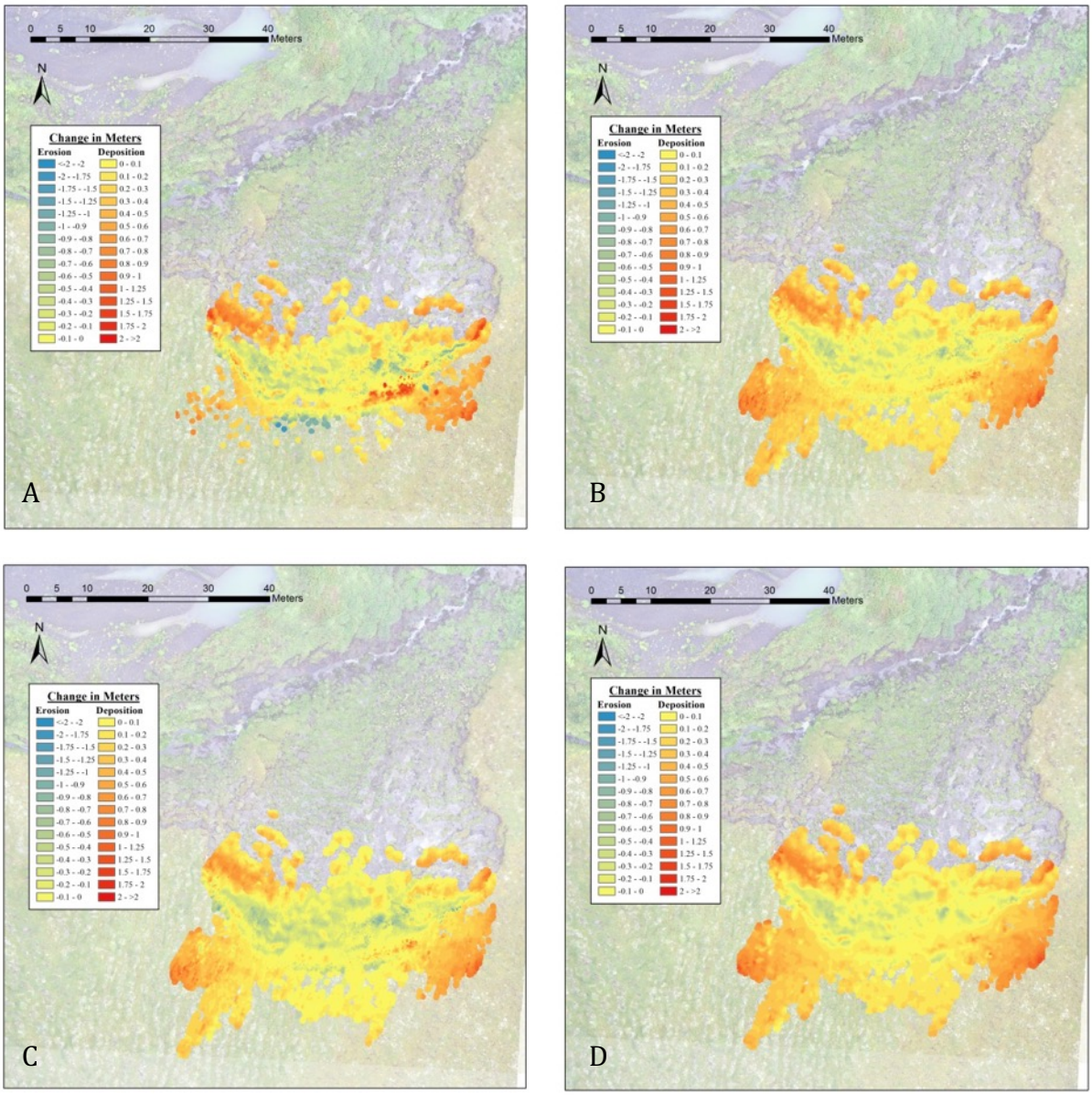

Figure 30. Elevation change results of SfM models at D1 (relative to August 3, 2016 UAV reference model) derived from camera array on August 14, 2017. A) DEMs of Difference (DoDs); B) Cloud to Mesh (C2M) distances (via Delaunay triangulation mesh; C) Cloud to Mesh (C2M) distances (via Poisson mesh); D) Multiscale Model to Model Cloud Comparison (M3C2) distances.

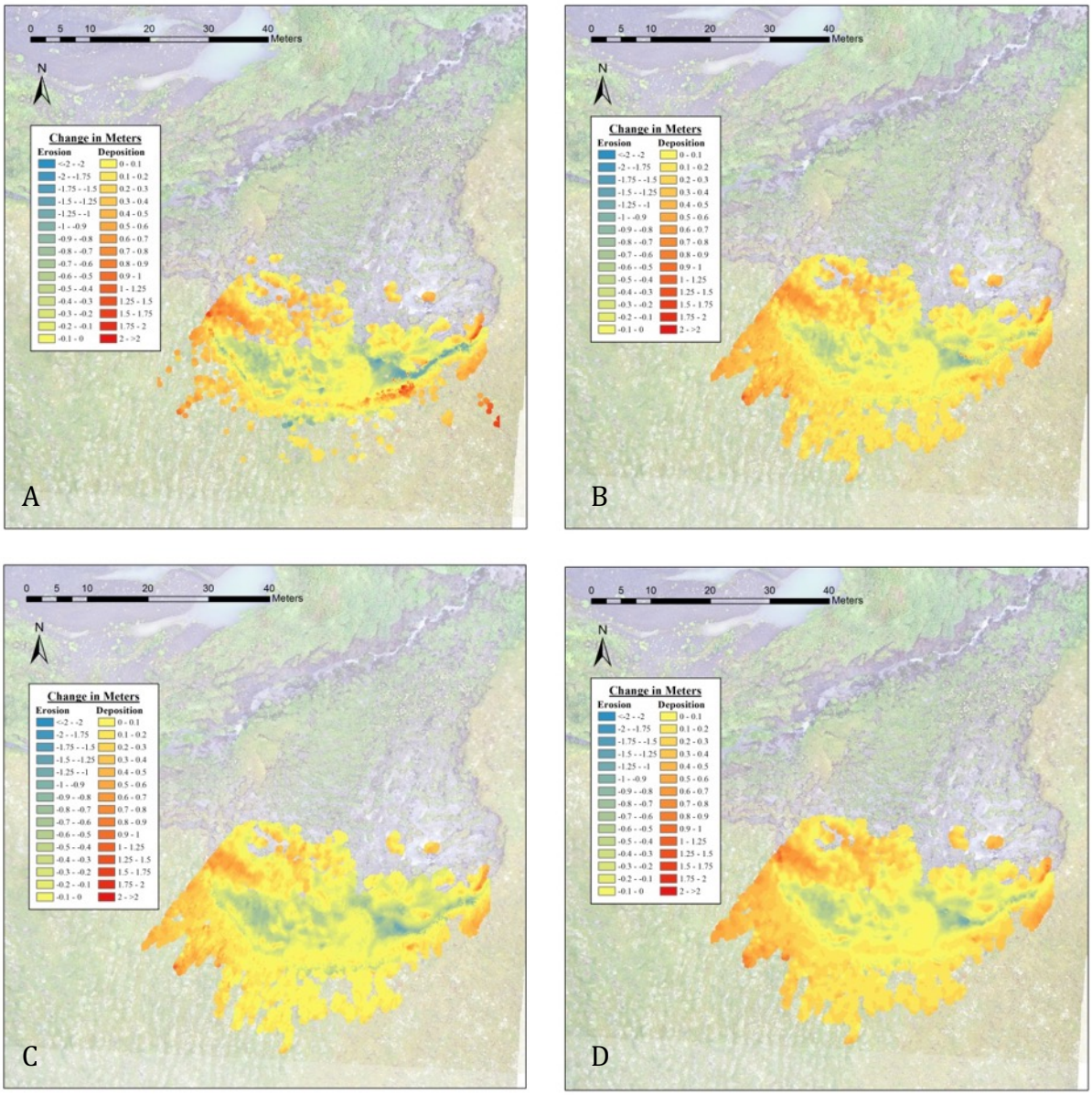

Figure 31. Elevation change results of SfM models at D1 (relative to August 3, 2016 UAV reference model) derived from camera array on August 20, 2017. A) DEMs of Difference (DoDs); B) Cloud to Mesh (C2M) distances (via Delaunay triangulation mesh; C) Cloud to Mesh (C2M) distances (via Poisson mesh); D) Multiscale Model to Model Cloud Comparison (M3C2) distances.

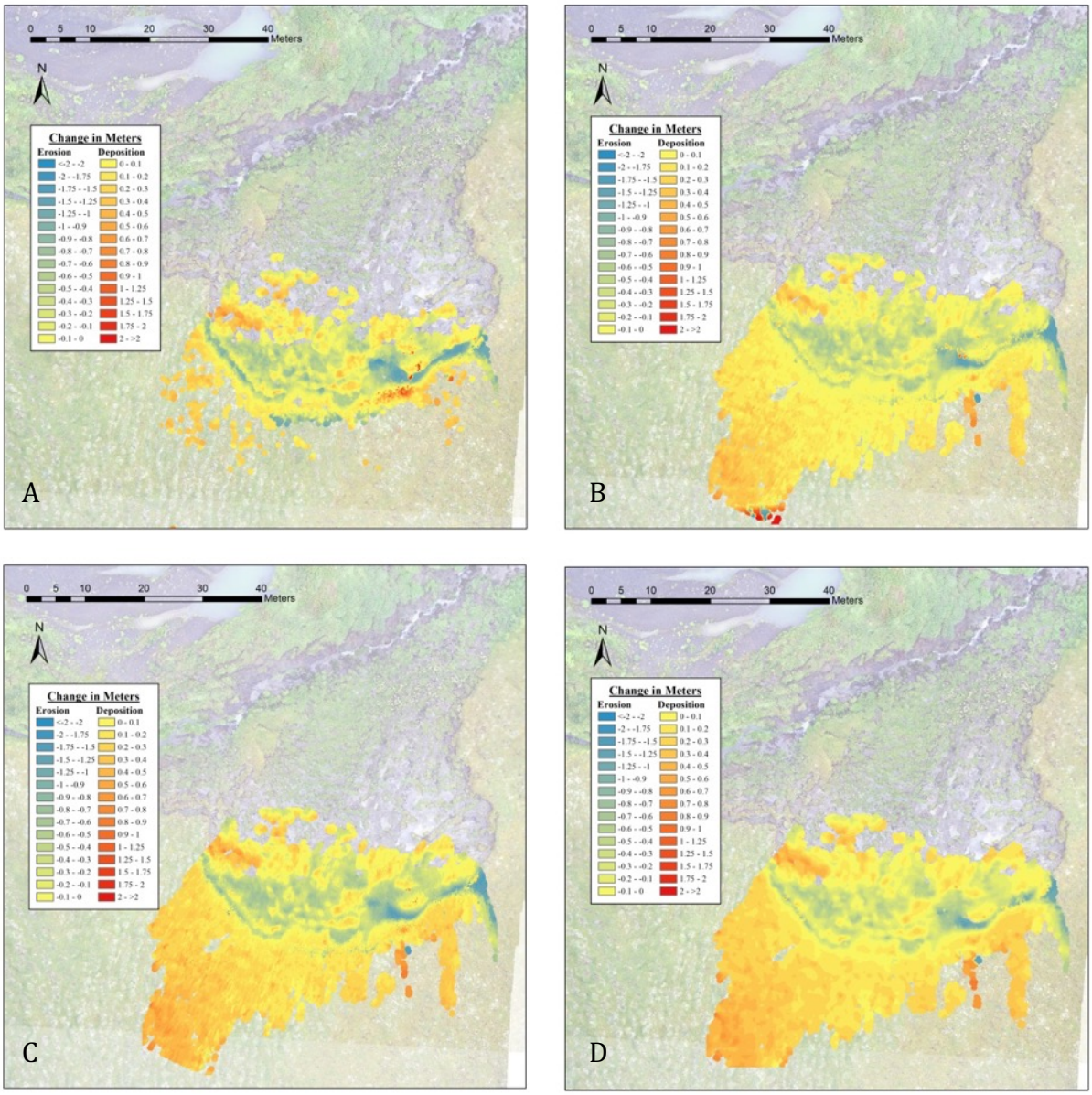

Figure 32. Elevation change results of SfM models at D1 (relative to August 3, 2016 UAV reference model) derived from camera array on September 2, 2017. A) DEMs of Difference (DoDs); B) Cloud to Mesh (C2M) distances (via Delaunay triangulation mesh; C) Cloud to Mesh (C2M) distances (via Poisson mesh); D) Multiscale Model to Model Cloud Comparison (M3C2) distances.

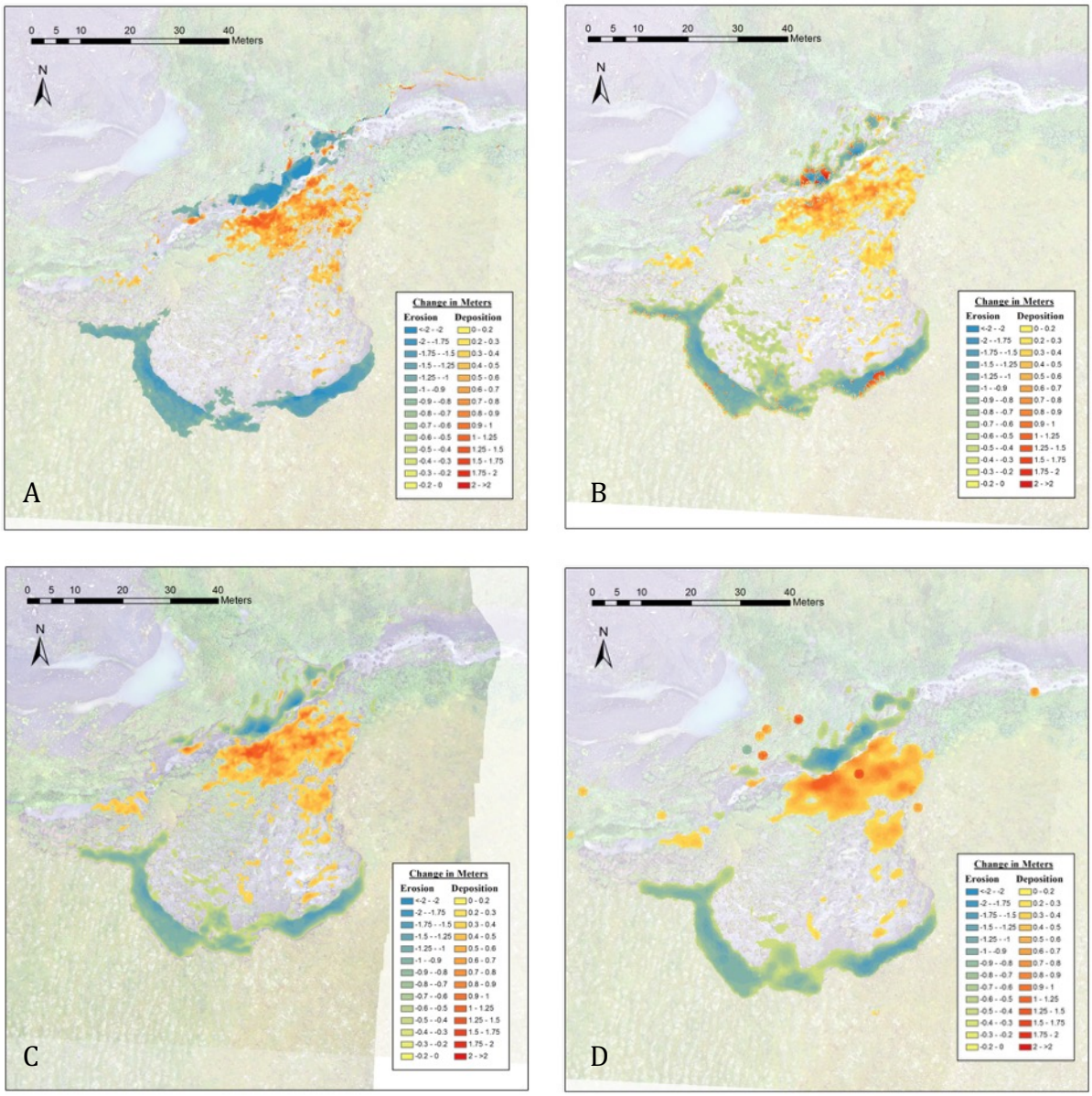

Figure 33. Elevation change results of SfM models derived from UAV imagery in July 27, 2015 and August 3, 2016. Data has been reduced to the extreme values falling under and over the 10% and 90% quantiles, respectively. A) DoD; B) C2M distances (via Delaunay triangulation mesh); C) C2M distances (via Poisson mesh); D) M3C2 distances. Courtesy of Robert Fraser, CCRS.

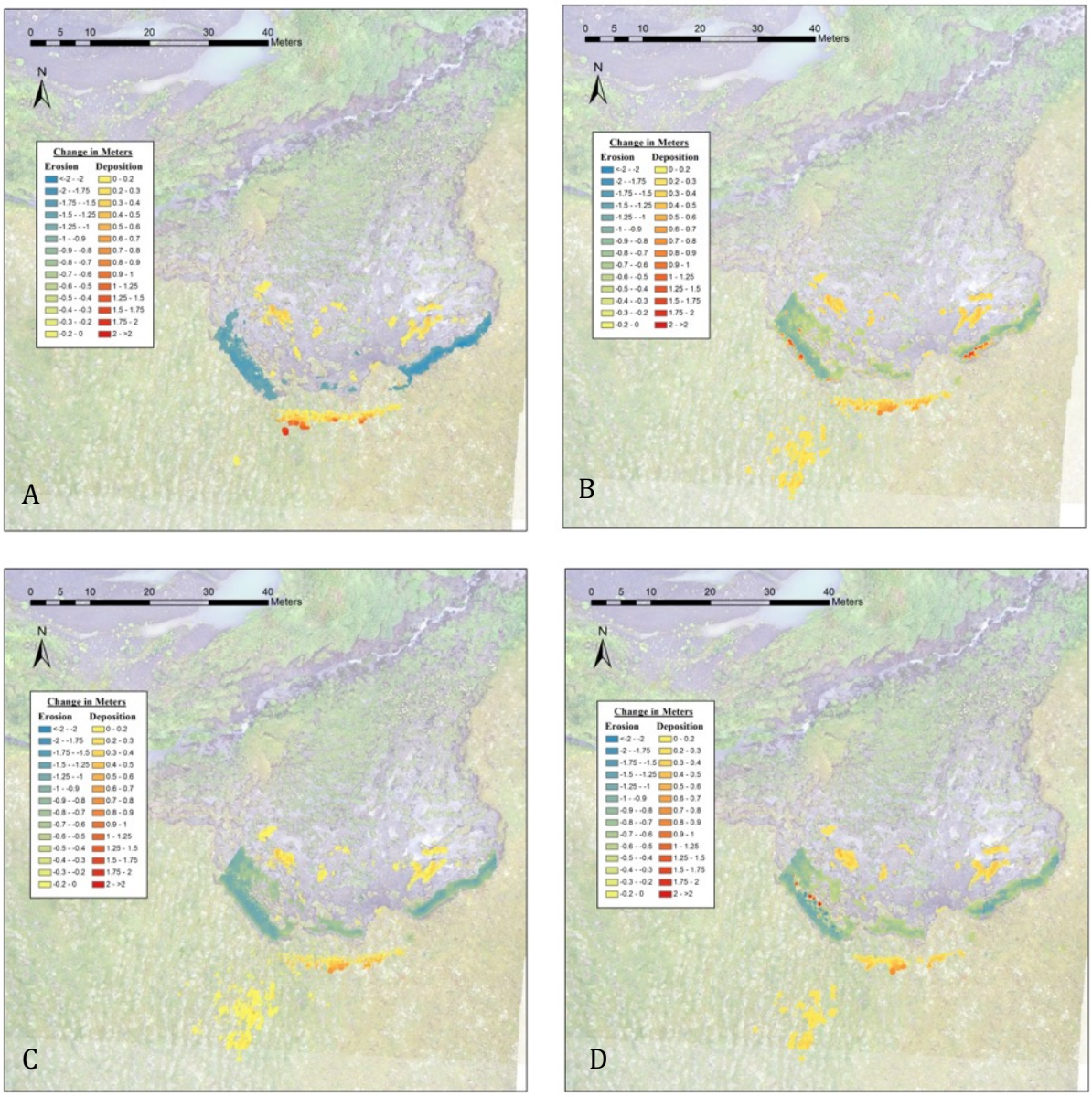

Figure 34. Elevation change results of SfM models at D1 (relative to August 3, 2016 UAV reference model) derived from camera array on June 27, 2017. Data has been reduced to the extreme values falling under and over the 10% and 90% quantiles, respectively. A) DEMs of Difference (DoDs); B) Cloud to Mesh (C2M) distances (via Delaunay triangulation mesh; C) Cloud to Mesh (C2M) distances (via Poisson mesh); D) Multiscale Model to Model Cloud Comparison (M3C2) distances.

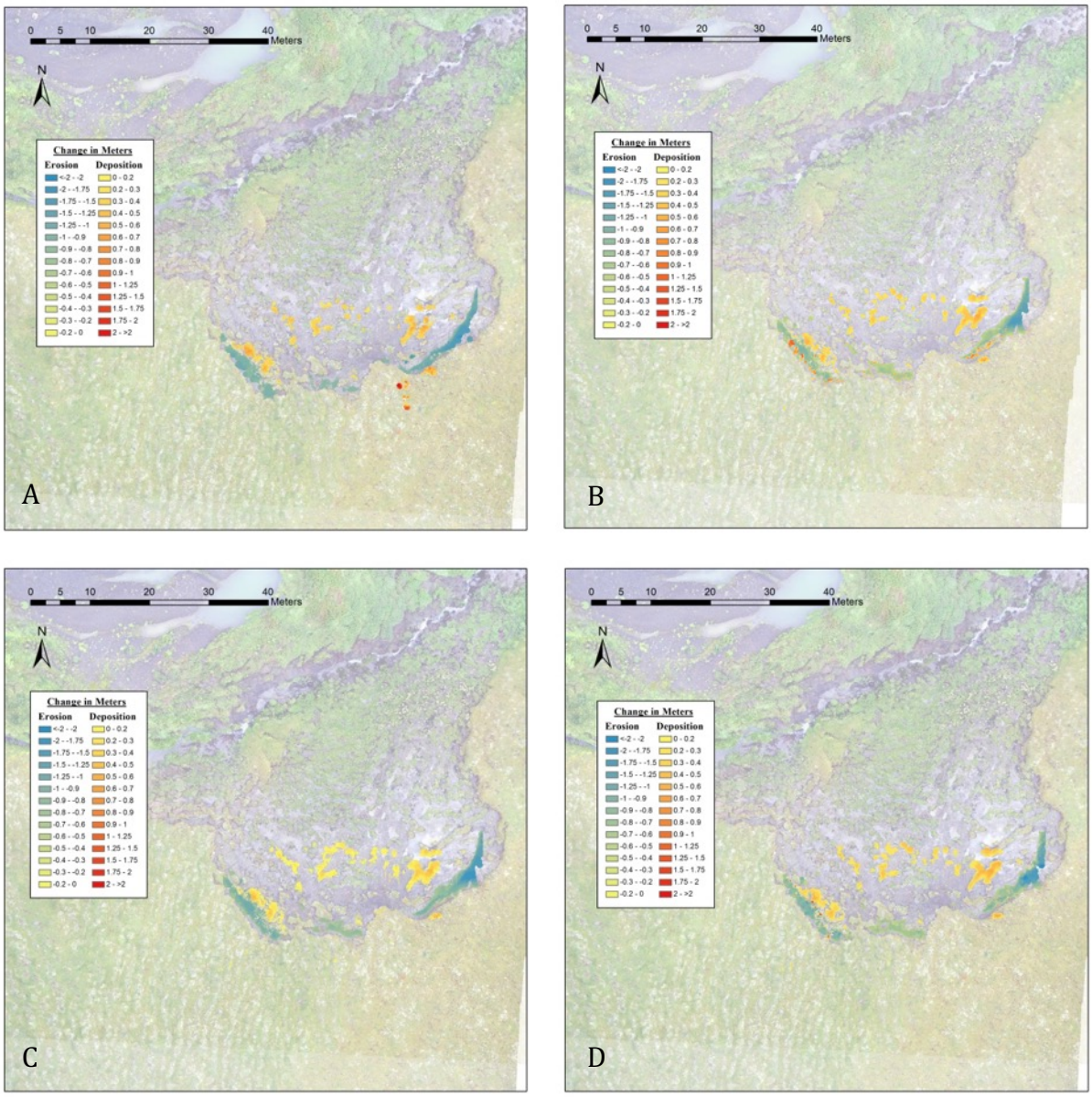

Figure 35. Elevation change results of SfM models at D1 (relative to August 3, 2016 UAV reference model) derived from camera array on July 7, 2017. Data has been reduced to the extreme values falling under and over the 10% and 90% quantiles, respectively. A) DEMs of Difference (DoDs); B) Cloud to Mesh (C2M) distances (via Delaunay triangulation mesh; C) Cloud to Mesh (C2M) distances (via Poisson mesh); D) Multiscale Model to Model Cloud Comparison (M3C2) distances.

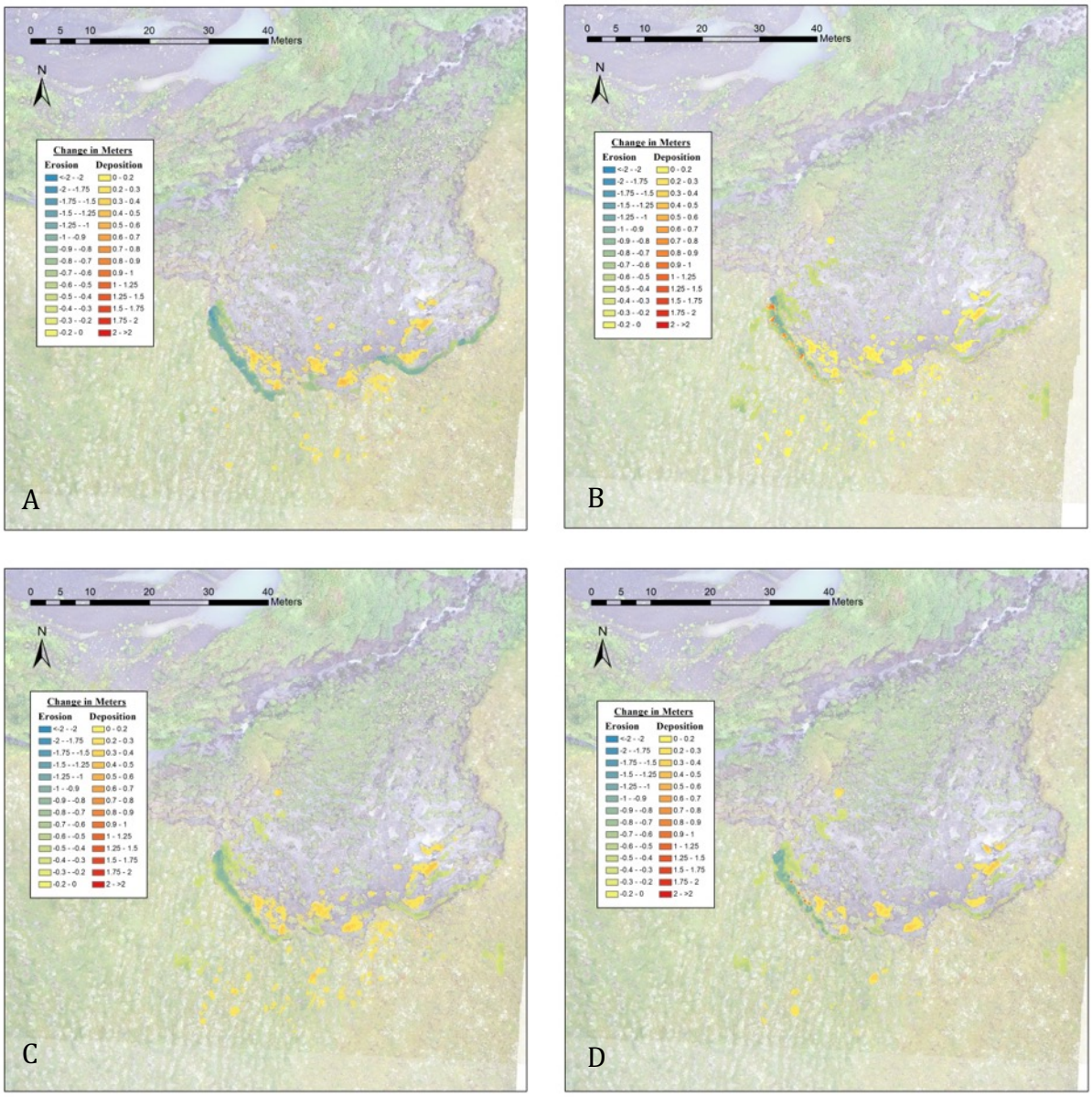

Figure 36. Elevation change results of SfM models at D1 (relative to August 3, 2016 UAV reference model) derived from camera array on July 17, 2017. Data has been reduced to the extreme values falling under and over the 10% and 90% quantiles, respectively. A) DEMs of Difference (DoDs); B) Cloud to Mesh (C2M) distances (via Delaunay triangulation mesh; C) Cloud to Mesh (C2M) distances (via Poisson mesh); D) Multiscale Model to Model Cloud Comparison (M3C2) distances.

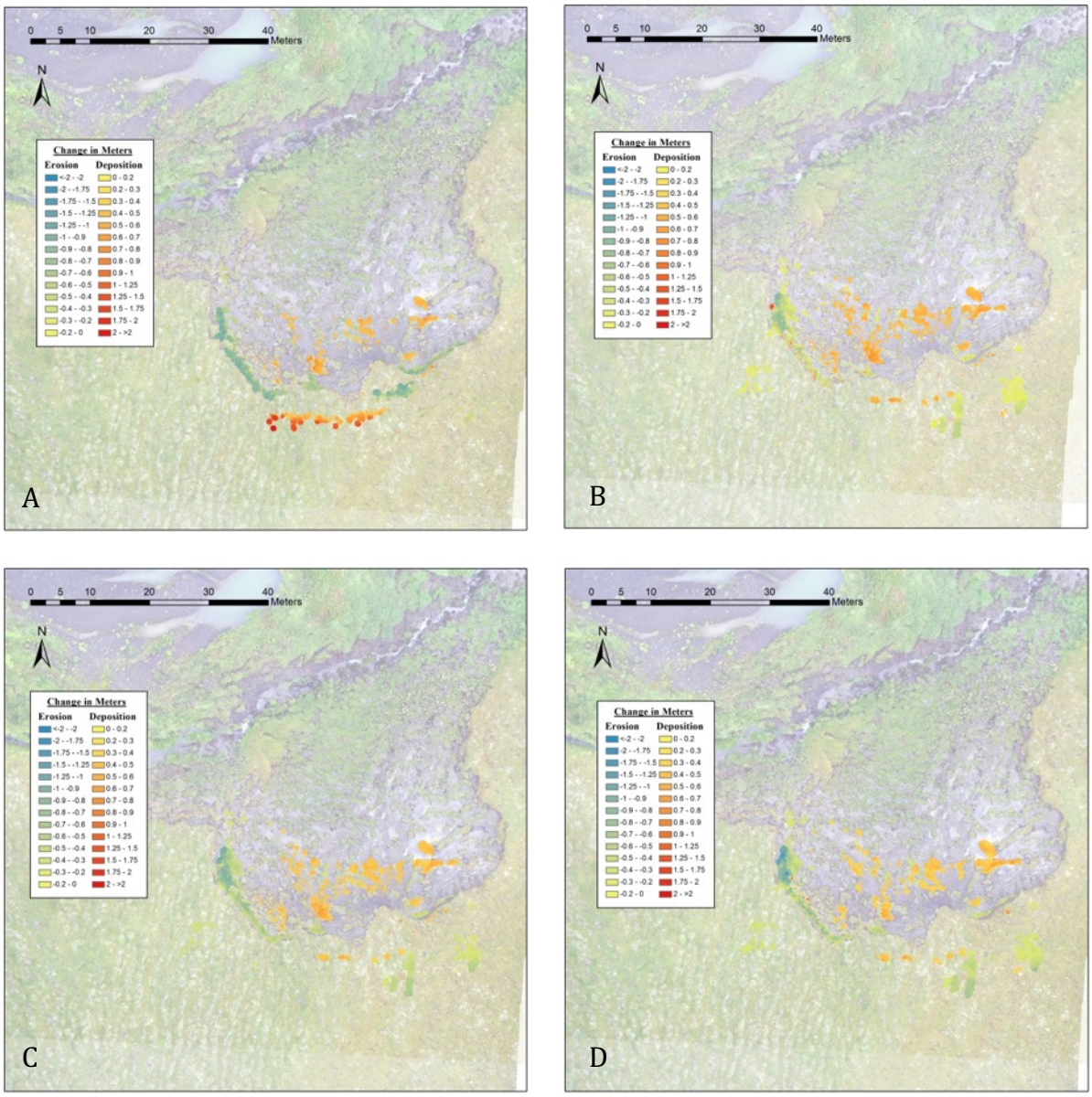

Figure 37. Elevation change results of SfM models at D1 (relative to August 3, 2016 UAV reference model) derived from camera array on July 25, 2017. Data has been reduced to the extreme values falling under and over the 10% and 90% quantiles, respectively. A) DEMs of Difference (DoDs); B) Cloud to Mesh (C2M) distances (via Delaunay triangulation mesh; C) Cloud to Mesh (C2M) distances (via Poisson mesh); D) Multiscale Model to Model Cloud Comparison (M3C2) distances.

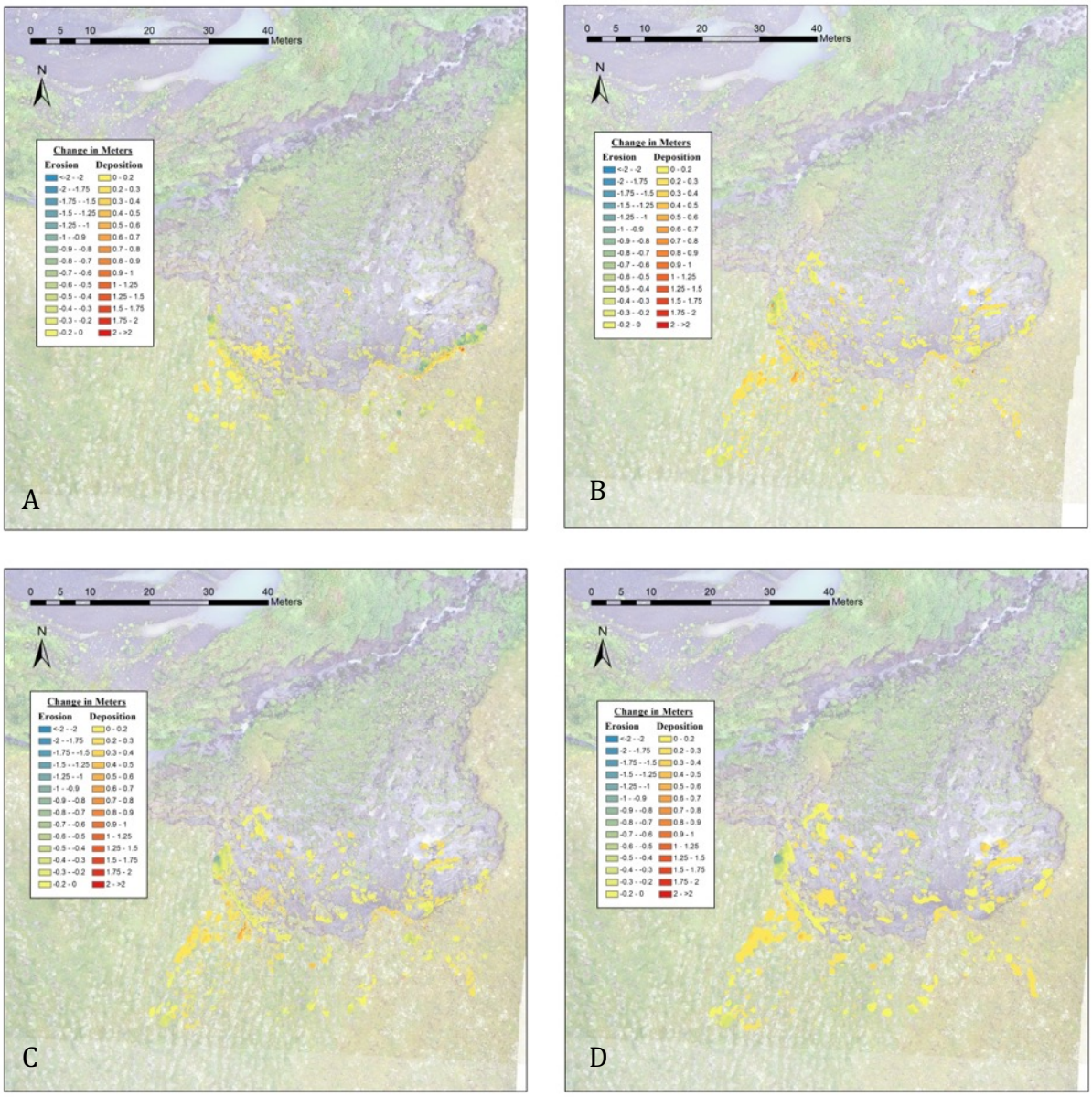

Figure 38. Elevation change results of SfM models at D1 (relative to August 3, 2016 UAV reference model) derived from camera array on August 1, 2017. Data has been reduced to the extreme values falling under and over the 10% and 90% quantiles, respectively. A) DEMs of Difference (DoDs); B) Cloud to Mesh (C2M) distances (via Delaunay triangulation mesh; C) Cloud to Mesh (C2M) distances (via Poisson mesh); D) Multiscale Model to Model Cloud Comparison (M3C2) distances.

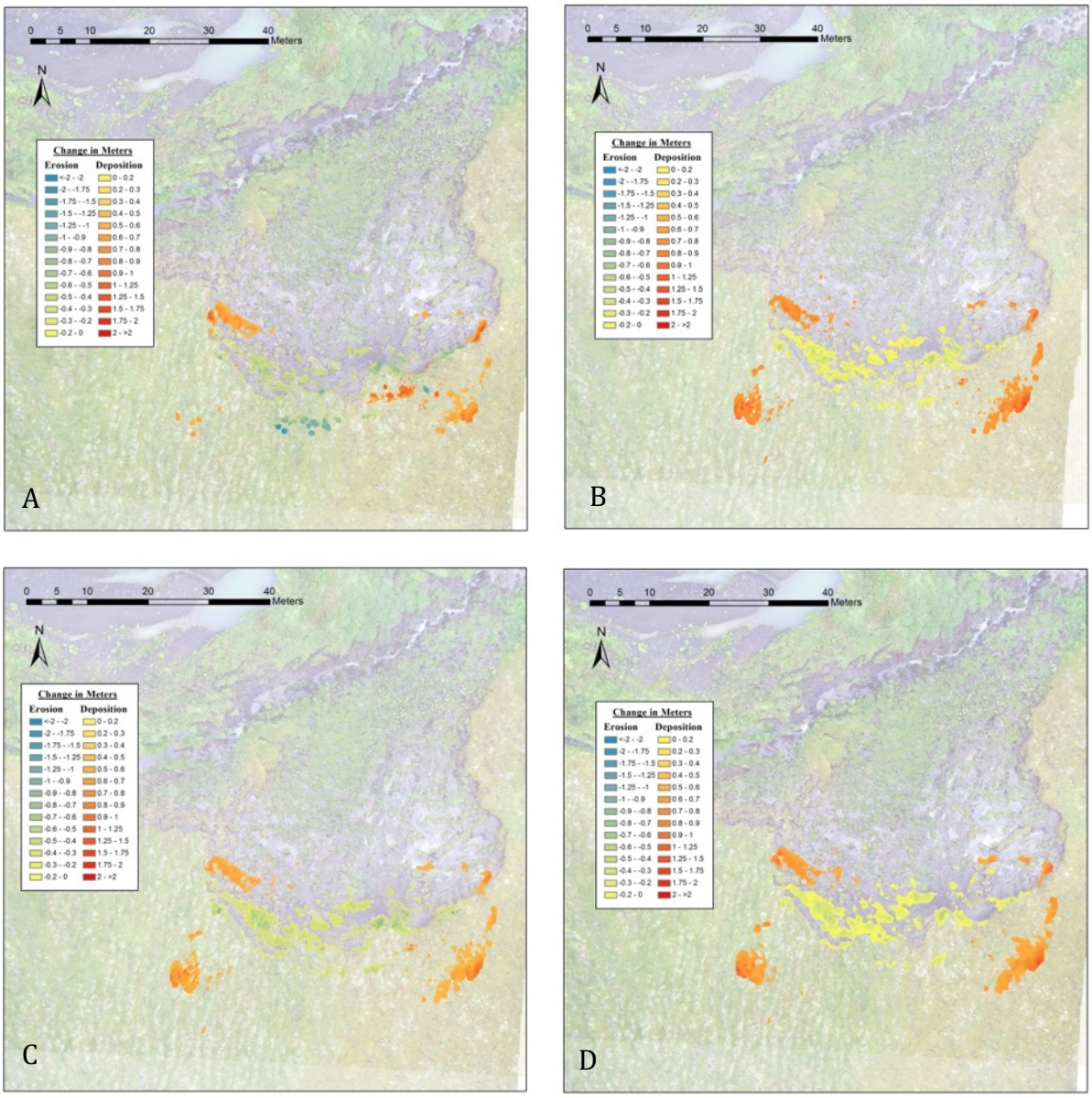

Figure 39. Elevation change results of SfM models at D1 (relative to August 3, 2016 UAV reference model) derived from camera array on August 14, 2017. Data has been reduced to the extreme values falling under and over the 10% and 90% quantiles, respectively. A) DEMs of Difference (DoDs); B) Cloud to Mesh (C2M) distances (via Delaunay triangulation mesh; C) Cloud to Mesh (C2M) distances (via Poisson mesh); D) Multiscale Model to Model Cloud Comparison (M3C2) distances.

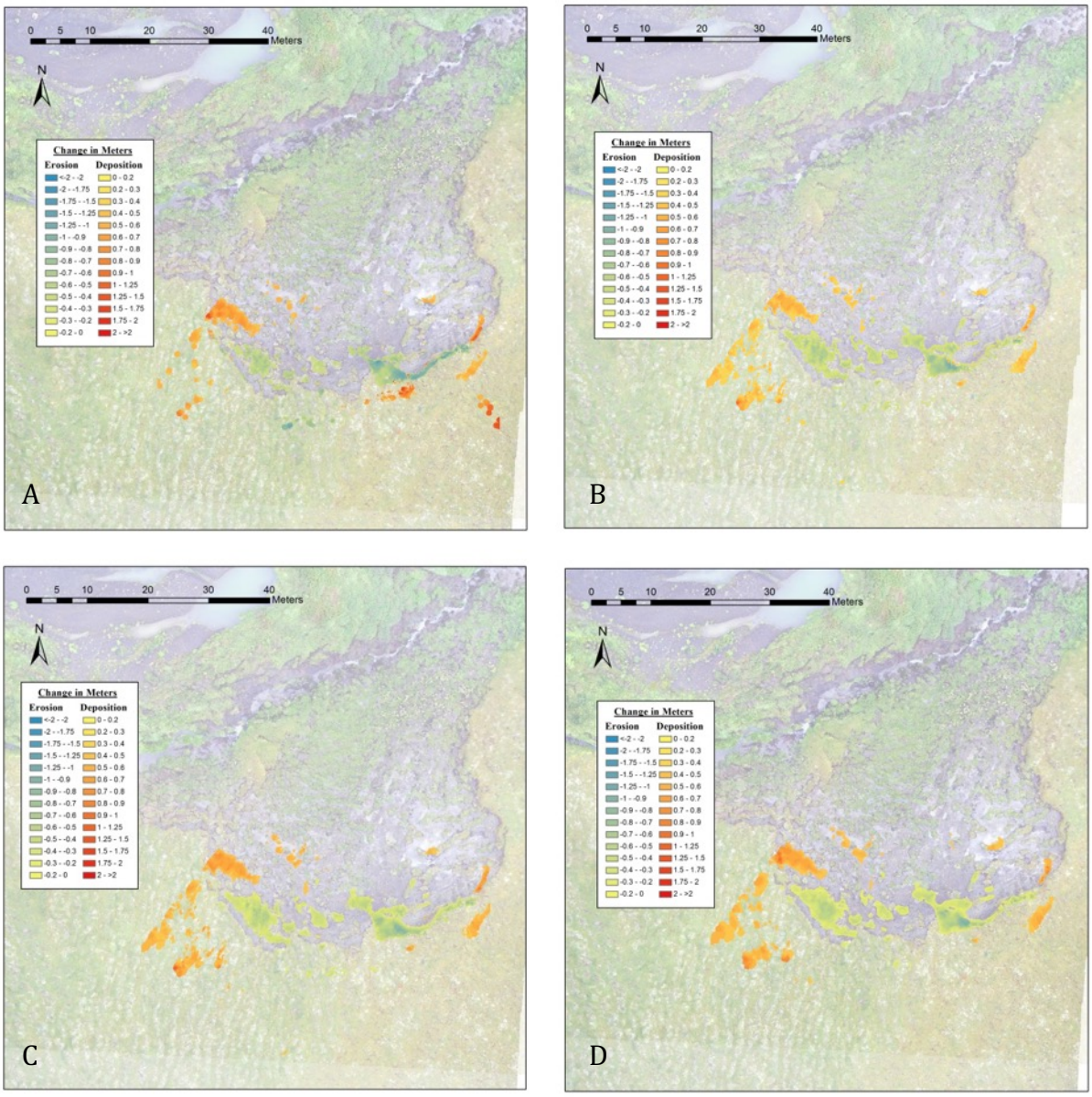

Figure 40. Elevation change results of SfM models at D1 (relative to August 3, 2016 UAV reference model) derived from camera array on August 20, 2017. Data has been reduced to the extreme values falling under and over the 10% and 90% quantiles, respectively. A) DEMs of Difference (DoDs); B) Cloud to Mesh (C2M) distances (via Delaunay triangulation mesh; C) Cloud to Mesh (C2M) distances (via Poisson mesh); D) Multiscale Model to Model Cloud Comparison (M3C2) distances.

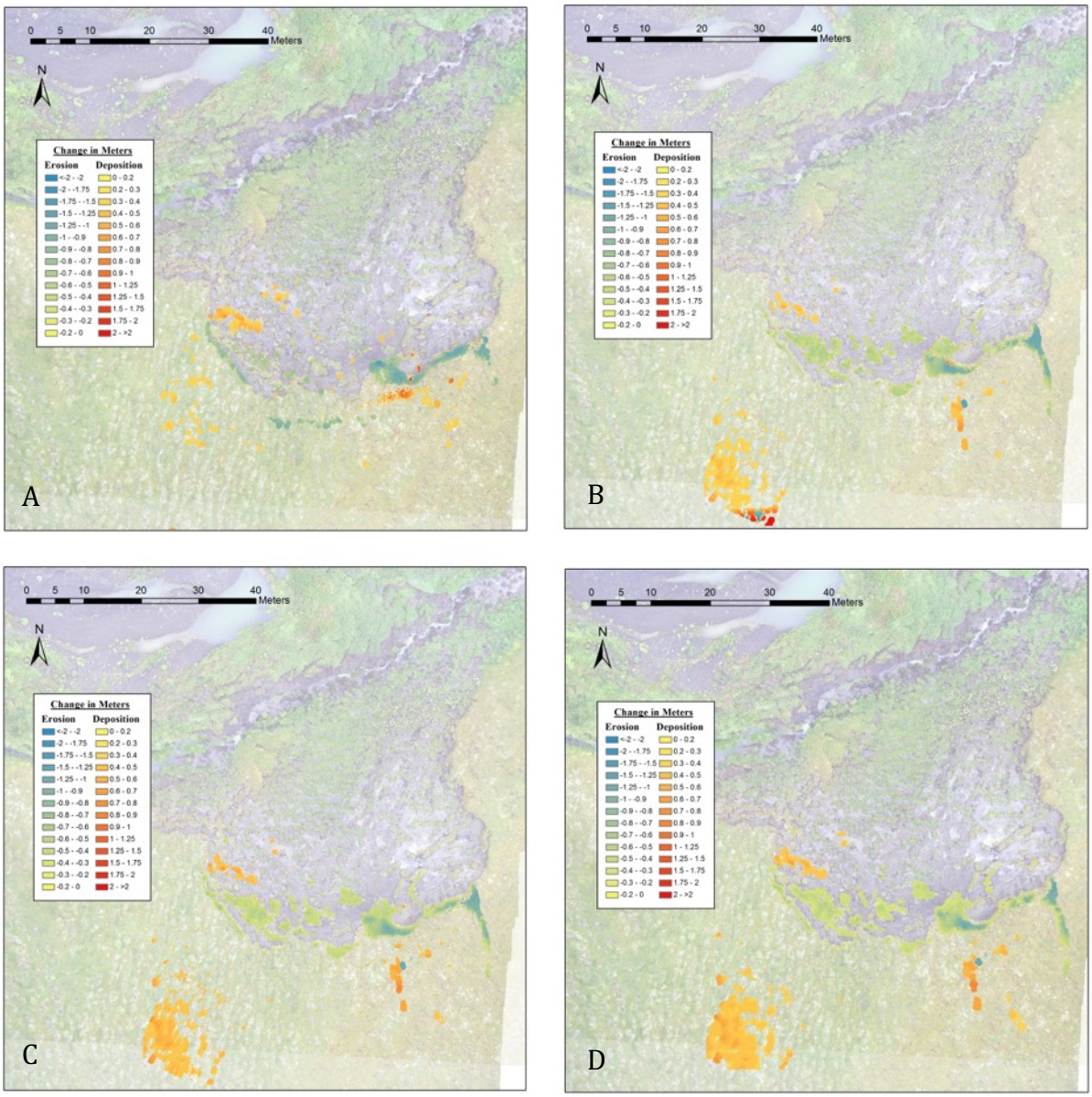

Figure 41. Elevation change results of SfM models at D1 (relative to August 3, 2016 UAV reference model) derived from camera array on September 2, 2017. Data has been reduced to the extreme values falling under and over the 10% and 90% quantiles, respectively. A) DEMs of Difference (DoDs); B) Cloud to Mesh (C2M) distances (via Delaunay triangulation mesh; C) Cloud to Mesh (C2M) distances (via Poisson mesh); D) Multiscale Model to Model Cloud Comparison (M3C2) distances.

Figure 42. Ground control target (1-foot diameter) displaying an example of high image compression in acquired trail cameras.